

# Leading and beyond leading-order spectral form factor in chaotic quantum many-body systems across all Dyson symmetry classes

Vijay Kumar,<sup>1</sup> Tomaž Prosen,<sup>2,3</sup> and Dibyendu Roy<sup>1</sup>

<sup>1</sup>*Raman Research Institute, Bangalore 560080, India*

<sup>2</sup>*Physics Department, Faculty of Mathematics and Physics,  
University of Ljubljana, Jadranska 19, SI-1000 Ljubljana, Slovenia*

<sup>3</sup>*Institute of Mathematics, Physics and Mechanics, Jadranska 19, SI-1000 Ljubljana, Slovenia*

We show the emergence of random matrix theory (RMT) spectral correlations in the chaotic phase of generic periodically kicked interacting quantum many-body systems by analytically calculating spectral form factor (SFF),  $K(t)$ , up to two leading orders in time,  $t$ . We explicitly consider the presence or absence of time reversal ( $\mathcal{T}$ ) symmetry to investigate all three Dyson's symmetry classes. Our derivation only assumes random phase approximation to enable ensemble average. For  $\mathcal{T}$ -invariant systems with  $\mathcal{T}^2 = 1$ , we show that beyond the Thouless time  $t^*$ , the SFF takes the form  $K(t) \simeq 2t - 2t^2/\mathcal{N}$  up to second order in time, where  $\mathcal{N}$  is the Hilbert space dimension. This is identical to the result from circular orthogonal ensemble of RMT. In the absence of  $\mathcal{T}$ -symmetry, we show that  $K(t) \simeq t$  beyond  $t^*$ , and there is no universal term in the second order, unlike the  $\mathcal{T}^2 = 1$  case, in agreement with the result of circular unitary ensemble. For  $\mathcal{T}$ -invariant systems with  $\mathcal{T}^2 = -1$ , we show that  $K(t) \simeq 2t + 2t^2/\mathcal{N}$  up to two orders in time beyond  $t^*$ , in agreement with the result of circular symplectic ensemble. In all three cases, the system-size,  $L$ , scaling of  $t^*$  is determined by eigenvalues of a doubly stochastic matrix  $\mathcal{M}$ . For strongly interacting fermionic chains,  $\mathcal{M}$  is  $SU(2)$  invariant in all three cases, leading to  $t^* \propto L^2$  in the presence of  $U(1)$  symmetry. In the absence of  $U(1)$  symmetry, we find  $t^* \propto L^0$ , due to gapped non-degenerate second-largest eigenvalue of  $\mathcal{M}$  or  $t^* \propto \ln(L)$  due to gapped second-largest eigenvalue with degeneracy  $\propto L^\zeta$ . Our calculation of SFF is plausible in higher space dimensions as well, where similar system-size scalings of  $t^*$  can be obtained.

## I. INTRODUCTION

The quantum origin of chaos is still very actively studied even after fifty years of intensive research. An epoch in the field started with observing universal statistical properties of the spectra of quantum systems whose classical analogs are chaotic. These spectral properties are excellently described by random matrix theory (RMT) [1–5], which was introduced in nuclear physics by Eugene Wigner to predict the distribution of energy level spacings of heavy nuclei [6–10]. The success of RMT in capturing the universal spectral properties has been so remarkable that the presence of RMT behavior in a physical system is investigated to diagnose quantum chaos. Further advancing our understanding of quantum chaos requires an explanation for the emergence of RMT behavior in physical systems.

A widely recognized and meaningful approach in this context involves analytically identifying statistical measures for random matrices and quantum systems with chaotic classical analogs. The results for the two cases are expected to match, but the steps leading to such a match would explain why such quantum systems behave identically to random matrices. The spectral form factor (SFF), a measure of correlation between energy levels, is extensively studied to diagnose quantum chaos. For time reversal ( $\mathcal{T}$ ) invariant systems with  $\mathcal{T}^2 = 1$  representing Gaussian orthogonal ensembles, the SFF takes

the following form in RMT [6]:

$$K_{\text{GOE}}(t) = 2t - t \ln \left( 1 + \frac{2t}{t_{\text{H}}} \right) = 2t - \frac{2t^2}{t_{\text{H}}} + \frac{2t^3}{t_{\text{H}}^2} - \dots, \quad (1)$$

where  $t$  is the time and  $t_{\text{H}}$  is the Heisenberg time, which is related to the Hilbert space dimension  $\mathcal{N}$ . Berry [11], calculated the SFF up to leading order in time using the semiclassical periodic orbit theory, which was later extended up to second order in time by Sieber and Richter [12, 13]. Finally, the complete derivation, up to all orders in time, was performed by Müller *et al.* [14, 15]. Additionally, a rigorous explanation has been possible only for quantum graphs [16, 17]. These studies provided valuable information on the reasons for the effectiveness of RMT. However, the RMT spectral statistics has also been observed to emerge in quantum many-body systems without classical analogs and is used to diagnose chaos in such systems as well. Therefore, a proper explanation of the emergence of RMT statistics in quantum many-body systems without classical analogs requires approaches that extend beyond the semiclassical periodic orbit theory.

In recent years, the SFF has been calculated in different studies to understand quantum chaos in interacting many-body systems and its connection to RMT [18–38]. Some of these studies showed the emergence of RMT SFF in quantum circuits with random unitary gates within the limits of large local Hilbert space dimensions [18, 21, 25, 27, 31]. While quantum circuits are powerful theoretical tools, the requirement of a large local Hilbert space dimension leaves the question unanswered

for physical systems with finite local Hilbert space dimensions like interacting fermions or qubits. Other studies involve effective field theory description [33], but a general mechanism explaining the emergence of RMT behavior for generic many-body quantum systems is still under question. Kos *et al.*[19] made a significant advancement in this direction by deriving the SFF up to two leading orders in time. They considered a one-dimensional (1D) system of qubits with long-range interactions and a periodically kicked magnetic field in a transverse direction. Following the random phase approximation (RPA), they could express the leading-order contribution of SFF in terms of a partition function of a classical 1D Ising model (on a ring of circumference  $t$ ), which can be calculated via a  $2 \times 2$  transfer matrix. It was plausible as the transverse field does not lead to any coupling among qubits in the driving Hamiltonian. This calculation was further generalized for the generic driving Hamiltonian in [26] to derive the SFF only in leading order in time. The higher-order terms of SFF for generic many-body quantum systems remain yet to be found. Furthermore, the models studied in [19, 26, 30, 37] have  $\mathcal{T}$  invariance. From a technical point of view, it is not clear how the formalism can be extended to systems in the absence of  $\mathcal{T}$ -symmetry or half-integer spin systems with  $\mathcal{T}$  invariance where  $\mathcal{T}$  satisfies  $\mathcal{T}^2 = -1$ . In particular, while the number of diagrams that contribute in the first and second order in  $t$  for  $\mathcal{T}$ -invariant systems with  $\mathcal{T}^2 = 1$  and in the absence of  $\mathcal{T}$ -symmetry is finite, the number of such diagrams is exponentially large in  $t$  for  $\mathcal{T}$ -invariant systems with  $\mathcal{T}^2 = -1$ . Thus, one must find an alternative scheme to evaluate the SFF for  $\mathcal{T}$ -invariant systems with  $\mathcal{T}^2 = -1$ . We have achieved this goal in this work, which is one of the main highlights of this paper.

This work calculates the SFF up to two leading orders in  $t$  for generic periodically kicked interacting many-body quantum systems with or without  $\mathcal{T}$ -symmetry, which allows us to investigate all three Dyson's circular ensembles [9, 10]. A recent study computed the exact SFF of non-interacting fermions with Dyson statistics [39]. Our approach involves the RPA to perform ensemble average, which has been checked to work very well for such systems in the presence of random onsite potentials and long-range interactions [26, 30, 37]. We show the emergence of universal RMT SFF for Dyson's symmetry classes, namely, circular orthogonal ensemble (COE) for  $\mathcal{T}^2 = 1$ , circular unitary ensemble (CUE) in the absence of  $\mathcal{T}$ -symmetry, and circular symplectic ensemble (CSE) for  $\mathcal{T}^2 = -1$ . The RMT predictions for the SFF of these ensembles are

$$K_{\text{COE}}(t) = 2t - t \ln \left( 1 + \frac{2t}{\mathcal{N}} \right), \quad (2)$$

$$K_{\text{CUE}}(t) = t, \quad (3)$$

$$K_{\text{CSE}}(t) = 2t - t \ln \left| 1 - \frac{2t}{\mathcal{N}} \right|, \quad (4)$$

for  $0 < t < \mathcal{N}$  [9, 10, 39, 40]. The SFF  $K_{\text{CSE}}(t)$  differs from the CSE SFF in Refs. [9, 40] by a factor of

$1/4$  because CSE SFF in these references is defined with an extra factor of  $1/4$ . However, we exclude this factor in our derivation for a unified description. Our explicit derivation of SFF is crucial because it explains how (e.g., the mechanism, nonuniversal behavior) and when (timescales) many-body quantum systems acquire a universal RMT form. For  $\mathcal{T}$ -invariant systems with  $\mathcal{T}^2 = 1$ , the leading order in  $t$  contribution to the SFF can be interpreted as a return probability  $P_t(\underline{n})$  to an initial state  $|\underline{n}\rangle$  after  $t$  time steps. The diagrams contributing to the second order in  $t$  of the SFF resemble the Sieber-Richter pairs of semiclassical periodic orbit theory [12, 13]. Most importantly, our results for the SFF not only give the universal SFF at longer time but also the nonuniversal part of SFF at short time, which goes beyond the RMT predictions. We particularly notice that the nonuniversal part of SFF at shorter times mainly comes from leading order in the  $t$  contributions of the SFF. We also determine the system-size scaling of the Thouless timescales  $t^*$  beyond which the SFF takes the universal RMT form in chains of spinless or spinful interacting fermions in the presence or absence of a  $U(1)$  symmetry. We observe  $P_t(\underline{n}) \sim 1$  when  $t \ll t^*$  and  $P_t(\underline{n}) \sim 1/\mathcal{N}$  when  $t \geq t^*$ . While 1D long-range models require more control to probe our predictions, checking them in higher dimensions experimentally would be easier. Our calculation of SFF is also applicable to higher space dimensions. We specifically notice the validity of the RPA for a shorter range of interactions with increasing coordination numbers that are easily feasible in higher dimensions. This work is highly significant as it explains the emergence of RMT behavior in generic many-body quantum systems.

The rest of the paper is organized as follows. In Sec. II, we present the basic models, the RPA used to perform ensemble average, and the key technical developments as four theorems in computing  $K(t)$ . We summarize the main findings in Sec. III. In Secs. IV-IX, we prove all the main technical steps. In Sec. X, we derive the leading-order SFF and the system-size scaling of  $t^*$  for each case of  $\mathcal{T}$ -symmetry. In Sec. XI, we explain the second order in time terms of the RMT SFF. In Sec. XII, we extend our  $K(t)$  calculation to higher spatial dimensions with an example showing identical system-size scaling of  $t^*$  as in lower dimension. Finally, we present our conclusion in Sec. XIII. Further technical details are presented in five appendices.

## II. MODELS AND OBSERVABLES OF INTEREST

The main goal of this paper is to provide an explanation for the emergence of RMT behavior in generic strongly interacting quantum systems. Thus, we study a general class of periodically kicked systems, described by the Hamiltonian

$$\hat{H}(t) = \hat{H}_0 + \tau_p \hat{H}_1 \sum_{n \in \mathbb{Z}} \delta(t - n\tau_p), \quad (5)$$

where  $\mathbb{Z}$  is the set of integers,  $\delta(t)$  is the Dirac delta function,  $\hat{H}_0$  and  $\hat{H}_1$  are two non-commuting Hermitian operators, and  $\tau_p$  is the period of kicking. We set  $\tau_p = 1$  for the rest of the discussion. We take  $\hat{H}_0$  to be  $\mathcal{T}$ -invariant, and  $\hat{H}_1$  with or without  $\mathcal{T}$ -symmetry. In Tab. I, we summarize the constraints imposed by these symmetries on relevant quantities related to  $\hat{H}_0$  and  $\hat{H}_1$ . To study the emergence of RMT behavior in such systems we study the SFF, which is defined as the Fourier transform of a connected two-point correlation function of spectral density [19, 40]. For periodically driven systems, the spectral density is defined as

$$\rho(\phi) = \frac{2\pi}{\mathcal{N}} \sum_{n=1}^{\mathcal{N}} \delta(\phi - \phi_n), \quad (6)$$

where  $\phi_n$  for  $n = 1, \dots, \mathcal{N}$  are eigenphases of the Floquet operator,  $\hat{U}$ . The connected two-point correlation function of  $\rho(\phi)$  is defined as

$$C(\theta) = \frac{1}{2\pi} \int_0^{2\pi} d\phi \rho(\phi + \theta/2) \rho(\phi - \theta/2) - 1. \quad (7)$$

We obtain the SFF by taking its Fourier transform:

$$K(t) = \frac{\mathcal{N}^2}{2\pi} \int_0^{2\pi} d\theta C(\theta) e^{-i\theta t} = [\text{tr} \hat{U}^t][\text{tr} \hat{U}^{-t}] - \mathcal{N}^2 \delta_{t,0}. \quad (8)$$

Since  $K(t)$  is not self averaging, we perform additional ensemble averaging denoted by  $\langle \dots \rangle$  and explained later in this section. Thus, the SFF takes the final form:

$$K(t) = \langle [\text{tr} \hat{U}^t][\text{tr} \hat{U}^{-t}] \rangle - \mathcal{N}^2 \delta_{t,0}. \quad (9)$$

For the Hamiltonian in Eq. (5), the operator  $\hat{U}$  can be expressed in terms of operators  $\hat{H}_0$  and  $\hat{H}_1$  as

$$\hat{U} = \mathbb{T} e^{-i \int_0^1 dt \hat{H}(t)} = \hat{V} \hat{W}, \quad (10)$$

where  $\mathbb{T}$  represents time ordering,  $\hat{V} = e^{-i\hat{H}_1}$ , and  $\hat{W} = e^{-i\hat{H}_0}$ . We choose the eigenstates of  $\hat{H}_0$ , denoted by  $|\underline{n}\rangle$ , as the basis states to compute the SFF. Thus, the operators  $\hat{H}_0$  and  $\hat{W}$  act as

$$\hat{H}_0 |\underline{n}\rangle = E_{\underline{n}} |\underline{n}\rangle, \quad (11)$$

$$\hat{W} |\underline{n}\rangle = e^{-i\theta_{\underline{n}}} |\underline{n}\rangle, \quad (12)$$

where the eigenvalues of  $\hat{H}_0$  and the eigenphases of  $\hat{W}$  are related by  $\theta_{\underline{n}} = E_{\underline{n}} \bmod 2\pi$ . Inserting identities  $\sum_{\underline{n}_\tau} |\underline{n}_\tau\rangle \langle \underline{n}_\tau| = \mathbb{1}_{\mathcal{N}}$  in  $\text{tr} \hat{U}^t$  and  $\sum_{\underline{n}'_\tau} |\underline{n}'_\tau\rangle \langle \underline{n}'_\tau| = \mathbb{1}_{\mathcal{N}}$  in  $\text{tr} \hat{U}^{-t}$  for  $\tau = 1, \dots, t$ , we obtain

$$K(t) = \sum_{\underline{n}_1, \dots, \underline{n}_t} \sum_{\underline{n}'_1, \dots, \underline{n}'_t} \langle e^{-i \sum_{\tau=1}^t (\theta_{\underline{n}_\tau} - \theta_{\underline{n}'_\tau})} \rangle \times \prod_{\tau=1}^t V_{\underline{n}_\tau, \underline{n}_{\tau+1}} V_{\underline{n}'_\tau, \underline{n}'_{\tau+1}}^*, \quad (13)$$

where the trace in Eq. (9) forces periodic boundary condition (PBC) in time,  $t+1 \equiv 1$ , and  $V$  denotes the matrix representation of  $\hat{V}$  in the computational basis with elements  $V_{\underline{n}, \underline{n}'} = \langle \underline{n} | \hat{V} | \underline{n}' \rangle$ . We assume that the phases  $\theta_{\underline{n}}$  are independent and uniformly distributed over the interval  $[0, 2\pi)$  apart from the case when  $\mathcal{T}^2 = -1$ , where the Kramers' degeneracy leads to doubly degenerate phases, but still, uniformly distributed. The assumption of independent and uniformly distributed phases has been tested numerically to success in the presence of random onsite potentials and long-range interactions in  $\hat{H}_0$  for 1D lattices [19, 26, 30, 37]. We shall later discuss that it works better in higher spatial dimensions, even for relatively shorter-range interactions. Therefore, we get by averaging over the phases:

$$\langle e^{-i \sum_{\tau=1}^t (\theta_{\underline{n}_\tau} - \theta_{\underline{n}'_\tau})} \rangle = \sum_{\pi} \prod_{\tau=1}^t \delta_{\theta_{\underline{n}'_\tau}, \pi(\theta_{\underline{n}_\tau})}, \quad (14)$$

where  $\pi$  is a permutation over  $t$  phases  $\{\theta_{\underline{n}_1}, \dots, \theta_{\underline{n}_t}\}$ . In general, one or more phases appear multiple times, thus, the collection of phases,  $\{\theta_{\underline{n}_1}, \dots, \theta_{\underline{n}_t}\}$ , forms a multiset. If there are  $l$  distinct phases of multiplicity  $p_1, \dots, p_l$ , satisfying  $\sum_{i=1}^l p_i = t$ , the permutations  $\pi$  belong to the group  $S_t / (S_{p_1} \times \dots \times S_{p_l})$ , where  $S_x$  is the symmetric group of degree  $x$  for  $x = t, p_1, \dots, p_l$ . For  $\mathcal{T}$ -invariant systems with  $\mathcal{T}^2 = 1$  and systems without  $\mathcal{T}$ -symmetry, all the phases are non-degenerate, which implies that the permutation of phases is equivalent to the permutation of states  $\underline{n}_\tau$ . Thus,

$$\pi(\theta_{\underline{n}_\tau}) = \theta_{\underline{n}_{\pi(\tau)}}. \quad (15)$$

For  $\mathcal{T}$ -invariant systems with  $\mathcal{T}^2 = -1$ , the phases are doubly degenerate, e.g.,  $\theta_{\underline{n}} = \theta_{\mathcal{T}\underline{n}}$ . Thus,

$$\pi(\theta_{\underline{n}_\tau}) = \theta_{\underline{n}_{\pi(\tau)}}, \theta_{\mathcal{T}\underline{n}_{\pi(\tau)}}, \quad (16)$$

where the subscript  $\mathcal{T}\underline{n}_{\pi(\tau)}$  represents the time-reversed state  $|\mathcal{T}\underline{n}_{\pi(\tau)}\rangle$  of a state  $|\underline{n}_{\pi(\tau)}\rangle$ . Substituting Eqs. (14,15) in Eq. (13) gives the SFF,  $K_1(t)$  and  $K_0(t)$ , respectively, for COE and CUE as

$$K_1(t) = \sum_{\underline{n}_1, \dots, \underline{n}_t} \sum_{\pi} \prod_{\tau=1}^t V_{\underline{n}_\tau, \underline{n}_{\tau+1}} V_{\underline{n}_{\pi(\tau)}, \underline{n}_{\pi(\tau+1)}}^*, \quad (17)$$

$$K_0(t) = \sum_{\underline{n}_1, \dots, \underline{n}_t} \sum_{\pi} \prod_{\tau=1}^t V_{\underline{n}_\tau, \underline{n}_{\tau+1}} V_{\underline{n}_{\pi(\tau)}, \underline{n}_{\pi(\tau+1)}}^*. \quad (18)$$

We stress that while the Eqs. (17,18) seem to have identical expressions on the right-hand side, the  $V$  matrix is symmetric in Eq. (17) and non-symmetric in Eq. (18). Substituting Eqs. (14,16) in Eq. (13) gives the SFF,  $K_{-1}(t)$  for CSE:

$$K_{-1}(t) = \sum_{\underline{n}_1, \dots, \underline{n}_t} \sum_{\pi} \sum_{\bar{\sigma}} \prod_{\tau=1}^t V_{\underline{n}_\tau, \underline{n}_{\tau+1}} V_{\underline{n}_{\pi(\tau)}, \underline{n}_{\pi(\tau+1)}}^*, \quad (19)$$

	Basis states under time reversal	Phases $\theta_{\underline{n}}$	$\hat{H}_1$ matrix	$\hat{V}(\equiv e^{-i\hat{H}_1})$ matrix
$\mathcal{T}^2 = \mathbf{1}$	$ \mathcal{T}\underline{n}\rangle =  \underline{n}\rangle$	non-degenerate	real symmetric	symmetric unitary
Absence of $\mathcal{T}$ -symmetry	$ \mathcal{T}\underline{n}\rangle =  \underline{n}\rangle$	non-degenerate	complex Hermitian	non-symmetric unitary
$\mathcal{T}^2 = -\mathbf{1}$	$\langle \underline{n}   \mathcal{T} \underline{n} \rangle = 0$	doubly degenerate, $\theta_{\mathcal{T}\underline{n}} = \theta_{\underline{n}}$	complex Hermitian with $\langle \mathcal{T}\underline{n}   \hat{H}_1   \mathcal{T}\underline{n}' \rangle = \langle \underline{n}   \hat{H}_1   \underline{n}' \rangle^*$ , $\langle \underline{n}   \hat{H}_1   \mathcal{T}\underline{n}' \rangle = -\langle \mathcal{T}\underline{n}   \hat{H}_1   \underline{n}' \rangle^*$ , $\langle \mathcal{T}\underline{n}   \hat{H}_1   \underline{n}' \rangle = -\langle \underline{n}   \hat{H}_1   \mathcal{T}\underline{n}' \rangle^*$	non-symmetric unitary with $\langle \mathcal{T}\underline{n}   \hat{V}   \mathcal{T}\underline{n}' \rangle = \langle \underline{n}'   \hat{V}   \underline{n} \rangle$ , $\langle \underline{n}   \hat{V}   \mathcal{T}\underline{n}' \rangle = -\langle \underline{n}'   \hat{V}   \mathcal{T}\underline{n} \rangle$ , $\langle \mathcal{T}\underline{n}   \hat{V}   \underline{n}' \rangle = -\langle \mathcal{T}\underline{n}'   \hat{V}   \underline{n} \rangle$

TABLE I: Constraints imposed on relevant quantities related to  $\hat{H}_0$  and  $\hat{H}_1$  by the presence or absence of time reversal ( $\mathcal{T}$ ) symmetry.

where  $\vec{\sigma} = (\sigma_1, \dots, \sigma_t)$  and  $\sigma_\tau = 0, 1$  for  $\tau = 1, \dots, t$  such that  $\underline{n}_{\pi(\tau)}^{(0)} = \underline{n}_{\pi(\tau)}$  and  $\underline{n}_{\pi(\tau)}^{(1)} = \mathcal{T}\underline{n}_{\pi(\tau)}$ . Since the subgroups of permutations  $\pi$  depend on the multiplicity of different phases in the multiset  $\{\theta_{\underline{n}_1}, \dots, \theta_{\underline{n}_t}\}$ , the summations  $\sum_{\underline{n}_1, \dots, \underline{n}_t}$  and  $\sum_{\pi}$  in Eqs. (17), (18), and (19) can not be performed independently. To make further progress, it is necessary to decouple the two summations. We introduce the following procedure to achieve this.

**Step 1:** We first take  $\pi \in S_t$ , irrespective of multiplicity of phases in the multiset  $\{\theta_{\underline{n}_1}, \dots, \theta_{\underline{n}_t}\}$ . For a multiset containing  $l$  distinct phases of multiplicity  $p_1, \dots, p_l$ , this leads to each distinct permutation being considered  $\prod_{i=1}^l p_i!$  times. Therefore, all the extra appearances of each distinct permutation must be removed. The following step explains how this can be achieved.

**Step 2:** We start by fixing the minimal case of repetition, where a phase appears twice in the multiset,  $\theta_{\underline{n}_{\tau_1}} = \theta_{\underline{n}_{\tau_2}}$ . Each distinct permutation of such a multiset appears twice. We remove the contributions of such extra appearances by explicitly calculating and then subtracting their contributions as below:

$$K_1(t) = \sum_{\pi \in S_t} \mathcal{X}_\pi - \sum_{\pi \in S_t/S_2} \mathcal{X}_\pi^{\{\underline{n}, \underline{n}\}} + \dots, \quad (20)$$

$$K_0(t) = \sum_{\pi \in S_t} \mathcal{Y}_\pi - \sum_{\pi \in S_t/S_2} \mathcal{Y}_\pi^{\{\underline{n}, \underline{n}\}} + \dots, \quad (21)$$

$$K_{-1}(t) = \sum_{\pi \in S_t} \sum_{\vec{\sigma}} \mathcal{Z}_{\pi, \vec{\sigma}} - \sum_{\pi \in S_t/S_2} \sum_{\vec{\sigma}} \mathcal{Z}_{\pi, \vec{\sigma}}^{\{\underline{n}, \underline{n}\}} - \sum_{\pi \in S_t/S_2} \sum_{\vec{\sigma}} \mathcal{Z}_{\pi, \vec{\sigma}}^{\{\underline{n}, \mathcal{T}\underline{n}\}} + \dots, \quad (22)$$

where

$$\mathcal{X}_\pi = \sum_{\{\underline{n}\}} \prod_{\tau=1}^t V_{\underline{n}_\tau, \underline{n}_{\tau+1}} V_{\underline{n}_{\pi(\tau)}, \underline{n}_{\pi(\tau+1)}}^*, \quad (23)$$

$$\mathcal{X}_\pi^{\{\underline{n}, \underline{n}\}} = \sum_{\{\underline{n}\}} \sum_{\tau_1 < \tau_2} \delta_{\underline{n}_{\tau_1}, \underline{n}_{\tau_2}} \prod_{\tau=1}^t V_{\underline{n}_\tau, \underline{n}_{\tau+1}} V_{\underline{n}_{\pi(\tau)}, \underline{n}_{\pi(\tau+1)}}^*, \quad (24)$$

$$\mathcal{Y}_\pi = \sum_{\{\underline{n}\}} \prod_{\tau=1}^t V_{\underline{n}_\tau, \underline{n}_{\tau+1}} V_{\underline{n}_{\pi(\tau)}, \underline{n}_{\pi(\tau+1)}}^*, \quad (25)$$

$$\mathcal{Y}_\pi^{\{\underline{n}, \underline{n}\}} = \sum_{\{\underline{n}\}} \sum_{\tau_1 < \tau_2} \delta_{\underline{n}_{\tau_1}, \underline{n}_{\tau_2}} \prod_{\tau=1}^t V_{\underline{n}_\tau, \underline{n}_{\tau+1}} V_{\underline{n}_{\pi(\tau)}, \underline{n}_{\pi(\tau+1)}}^*, \quad (26)$$

$$\mathcal{Z}_{\pi, \vec{\sigma}} = \sum_{\{\underline{n}\}} \prod_{\tau=1}^t V_{\underline{n}_\tau, \underline{n}_{\tau+1}} V_{\underline{n}_{\pi(\tau)}, \underline{n}_{\pi(\tau+1)}}^{(\sigma_\tau)}, \quad (27)$$

$$\mathcal{Z}_{\pi, \vec{\sigma}}^{\{\underline{n}, \underline{n}\}} = \sum_{\{\underline{n}\}} \sum_{\tau_1 < \tau_2} \delta_{\underline{n}_{\tau_1}, \underline{n}_{\tau_2}} \prod_{\tau=1}^t V_{\underline{n}_\tau, \underline{n}_{\tau+1}} V_{\underline{n}_{\pi(\tau)}, \underline{n}_{\pi(\tau+1)}}^{(\sigma_\tau)}, \quad (28)$$

$$\mathcal{Z}_{\pi, \vec{\sigma}}^{\{\underline{n}, \mathcal{T}\underline{n}\}} = \sum_{\{\underline{n}\}} \sum_{\tau_1 < \tau_2} \delta_{\underline{n}_{\tau_1}, \mathcal{T}\underline{n}_{\tau_2}} \prod_{\tau=1}^t V_{\underline{n}_\tau, \underline{n}_{\tau+1}} V_{\underline{n}_{\pi(\tau)}, \underline{n}_{\pi(\tau+1)}}^{(\sigma_\tau)}, \quad (29)$$

where  $\sum_{\{\underline{n}\}} = \sum_{\underline{n}_1, \dots, \underline{n}_t}$ . The symbols  $\mathcal{X}_\pi$  and  $\mathcal{Y}_\pi$  denote, respectively, the total contribution to SFFs  $K_1(t)$  and  $K_0(t)$  of a permutation  $\pi \in S_t$  of all the multisets of states  $\{\underline{n}_1, \dots, \underline{n}_t\}$ . The symbols  $\mathcal{X}_\pi^{\{\underline{n}, \underline{n}\}}$  and  $\mathcal{Y}_\pi^{\{\underline{n}, \underline{n}\}}$  represent, respectively, the correction for a permutation  $\pi \in S_t/S_2$  of all the multisets  $\{\underline{n}_1, \dots, \underline{n}_t\}$ , where at least one state appears two times. These terms fix the double counting of permutation  $\pi$  of such multisets in  $\mathcal{X}_\pi$  and  $\mathcal{Y}_\pi$ . However, the overcounting resulting from a higher number of repetitions is still present and requires further correction terms. In this paper, we restrict ourselves to double repetitions only. Similarly, the symbol  $\mathcal{Z}_{\pi, \vec{\sigma}}$  denotes a contribution to the SFF,  $K_{-1}(t)$ , of a permutation  $\pi \in S_t$  and configuration  $\vec{\sigma}$  of all the multisets of states  $\{\underline{n}_1, \dots, \underline{n}_t\}$ . In this case, when a phase repeats two times in  $\{\theta_{\underline{n}_1}, \dots, \theta_{\underline{n}_t}\}$ , due to the Kramers' degeneracy, either a state appears two times in  $\{\underline{n}_1, \dots, \underline{n}_t\}$  or a state and its time-reversed state appear in  $\{\underline{n}_1, \dots, \underline{n}_t\}$ . Thus, there are two correction terms, denoted by  $\mathcal{Z}_{\pi, \vec{\sigma}}^{\{\underline{n}, \underline{n}\}}$  and  $\mathcal{Z}_{\pi, \vec{\sigma}}^{\{\underline{n}, \mathcal{T}\underline{n}\}}$ .

Calculating the SFF for each case of  $\mathcal{T}$ -symmetry requires a procedure to calculate  $\mathcal{X}_\pi$ ,  $\mathcal{X}_\pi^{\{\underline{n}, \underline{n}\}}$ ,  $\mathcal{Y}_\pi$ ,  $\mathcal{Y}_\pi^{\{\underline{n}, \underline{n}\}}$ ,  $\mathcal{Z}_{\pi, \vec{\sigma}}$ ,  $\mathcal{Z}_{\pi, \vec{\sigma}}^{\{\underline{n}, \underline{n}\}}$ , and  $\mathcal{Z}_{\pi, \vec{\sigma}}^{\{\underline{n}, \mathcal{T}\underline{n}\}}$  for different permutations  $\pi$  and configurations  $\vec{\sigma}$ . Based on a diagrammatic representation of  $\pi$  and  $\vec{\sigma}$  (e.g., Fig. 1), we present rules to calculate the contribution of each permutation in Sec. IV-VI.

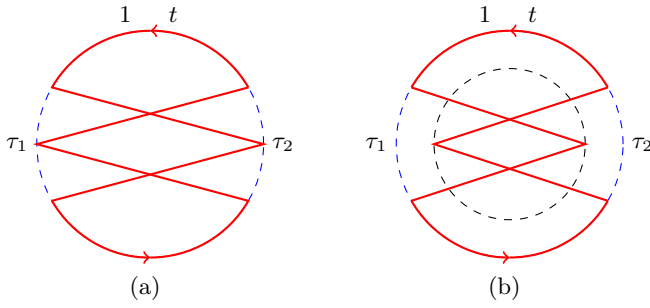


FIG. 1: (a) A diagrammatic representation of a transposition for systems with  $\mathcal{T}^2 = 1$  and without  $\mathcal{T}$ -symmetry, where states  $\underline{n}_{\tau_1}$  and  $\underline{n}_{\tau_2}$  are interchanged. The dashed blue circle represents initial configuration of states,  $\{\underline{n}_1, \dots, \underline{n}_{\tau_1}, \dots, \underline{n}_{\tau_2}, \dots, \underline{n}_t\}$ . The subscripts  $(1, \dots, t)$  are in increasing order along the counterclockwise direction on the blue circle. The red curve represents the configuration of states after transposition  $\{\underline{n}_1, \dots, \underline{n}_{\tau_2}, \dots, \underline{n}_{\tau_1}, \dots, \underline{n}_t\}$ . (b) A diagrammatic representation of a transposition for  $\mathcal{T}^2 = -1$  case, where states  $\underline{n}_{\tau_1}$  and  $\underline{n}_{\tau_2}$  are interchanged and  $\sigma_{\tau_1} = \sigma_{\tau_2} = 1, \sigma_\tau = 0$  for  $\tau = 1, \dots, t$  excluding  $\tau_1, \tau_2$ . The inner black dashed circle represent time reversed version of the states on the outer circle.

We further find that, unlike the  $\mathcal{T}^2 = 1$  and in the absence of  $\mathcal{T}$ -symmetry cases, the matrix  $V$  has a richer structure for  $\mathcal{T}^2 = -1$  as given in Tab. I. More specifically, the property  $\langle \mathcal{T} \underline{n} | \hat{V} | \mathcal{T} \underline{n}' \rangle = \langle \underline{n}' | \hat{V} | \underline{n} \rangle$  immediately leads to the following theorem for such systems:

**Theorem 1:** For a permutation  $\pi$  and a configuration  $\vec{\sigma} = (\sigma_1, \dots, \sigma_t)$ , there exists another configuration  $\vec{\sigma}' = (1 - \sigma_t, \dots, 1 - \sigma_1)$ , such that

$$\mathcal{Z}_{\pi, \vec{\sigma}} = \mathcal{Z}_{\mathcal{R}\pi, \vec{\sigma}'}, \quad (30)$$

where  $\mathcal{R}$  is a reflection/anticyclic permutation, which reverses the order of all states in  $\{\underline{n}_1, \dots, \underline{n}_t\}$ . Therefore, collectively, permutation  $\mathcal{R}\pi$  changes the order of states to  $\{\underline{n}_{\pi(t)}, \dots, \underline{n}_{\pi(1)}\}$ .

**Proof:** From Eq. (27), we write

$$\begin{aligned} \mathcal{Z}_{\pi, \vec{\sigma}} &= \sum_{\underline{n}_1, \dots, \underline{n}_t} \prod_{\tau=1}^t V_{\underline{n}_\tau, \underline{n}_{\tau+1}} V_{\underline{n}_{(\sigma_\tau)}, \underline{n}_{\pi(\tau+1)}}^* \\ &= \sum_{\underline{n}_1, \dots, \underline{n}_t} \prod_{\tau=1}^t V_{\underline{n}_\tau, \underline{n}_{\tau+1}} V_{\mathcal{T} \underline{n}_{\pi(\tau+1)}, \mathcal{T} \underline{n}_{\pi(\tau)}}^* \\ &= \sum_{\underline{n}_1, \dots, \underline{n}_t} \prod_{\tau=1}^t V_{\underline{n}_\tau, \underline{n}_{\tau+1}} V_{\underline{n}_{\pi(\tau+1)}^{(1-\sigma_{\tau+1})}, \underline{n}_{\pi(\tau)}^{(1-\sigma_\tau)}}^* \\ &= \mathcal{Z}_{\mathcal{R}\pi, \vec{\sigma}'}. \end{aligned} \quad (31)$$

Following the rules in Sec. IV-VI, the leading-order SFF determining the linear ramp can be easily derived

for the  $\mathcal{T}^2 = 1$  and without  $\mathcal{T}$ -symmetry cases by studying the  $t$  cyclic and  $t$  anticyclic variants of identity permutation,  $I$ ,

$$K_1^{(1)}(t) = \sum_{l=0}^{t-1} (\mathcal{X}_{\mathcal{C}^l I} + \mathcal{X}_{\mathcal{R}\mathcal{C}^l I}), \quad (32)$$

$$K_0^{(1)}(t) = \sum_{l=0}^{t-1} (\mathcal{Y}_{\mathcal{C}^l I} + \mathcal{Y}_{\mathcal{R}\mathcal{C}^l I}), \quad (33)$$

where the superscript (1) represents that the above expressions only contain the leading-order SFF, and  $\mathcal{C}^l$  denotes cyclic permutation, whose action is defined as  $\underline{n}_{\mathcal{C}^l(\tau)} = \underline{n}_{\tau+l}$  for  $\tau = 1, \dots, t$ . We explicitly evaluate  $K_1^{(1)}(t)$  and  $K_0^{(1)}(t)$  in Sec. X. However, for the  $\mathcal{T}^2 = -1$  case, each permutation  $\pi$  has further  $2^t$  variants due to configurations  $\vec{\sigma}$  in Eq. (22). Therefore, a brute-force calculation based on the rules in Sec. VI is practically impossible. Instead, a new approach is required. Our new approach starts with a general analysis of arbitrary diagrams in Sec. VII, which we formulate into the following theorem.

**Theorem 2:** Contributions  $\mathcal{X}_\pi, \mathcal{X}_\pi^{\{\underline{n}, \underline{n}\}}, \mathcal{Y}_\pi, \mathcal{Y}_\pi^{\{\underline{n}, \underline{n}\}}, \mathcal{Z}_{\pi, \vec{\sigma}}, \mathcal{Z}_{\pi, \vec{\sigma}}^{\{\underline{n}, \underline{n}\}}$ , and  $\mathcal{Z}_{\pi, \vec{\sigma}}^{\{\underline{n}, \mathcal{T} \underline{n}\}}$  can be expressed as a sum of three kinds of terms, namely, Type I, Type II, and Type III. Type I term is  $1/\mathcal{N}^\mu$ , where  $\mu$  is a non-negative integer. This term is universal since it is independent of Hamiltonian parameters. Type II and Type III terms are nonuniversal because they depend on Hamiltonian parameters. Furthermore, Type III terms decay exponentially with time, while Type II terms remain finite at long times.

**Theorem 2** implies that only Type I and Type II terms are significant in determining SFF at long time. More specifically, when the contribution of all the permutations is added, Type I terms must add up to give a universal RMT form of SFF, whereas Type II terms must cancel each other out. Type III terms only contribute to the nonuniversal part of SFF and vanish beyond  $t^*$ . **Theorem 2** also suggests that Type III terms are insignificant when the goal is to understand the emergence of RMT behavior. Thus, eliminating some Type III terms, we define reduced diagrams (see, for example, Fig. 2) in Sec. VIII. The reduced

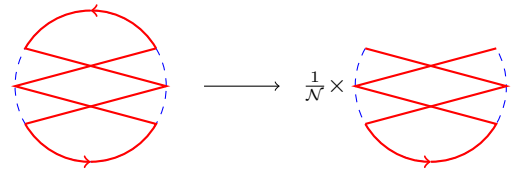


FIG. 2: A reduced diagram obtained by inserting a factor  $1/\mathcal{N}$  for a red arc in a diagram representing a transposition.

diagrams provide further analytical control. Performing

a general analysis of reduced diagrams, we discovered a meaningful pattern, which we formulated into the following theorems. For systems with  $\mathcal{T}^2 = 1$  and in the absence of  $\mathcal{T}$ -symmetry, we have the following theorem:

**Theorem 3:** For each reduced diagram, there exists a diagram with minimal repetition of states that has an identical reduced diagram.

**Theorem 3** implies that for a given permutation  $\pi$ , there exists a permutation  $\pi'$  such that Type I and Type II contribution of  $\mathcal{X}_\pi$  and  $\mathcal{X}_{\pi'}^{\{n,n\}}$  (or  $\mathcal{Y}_\pi$  and  $\mathcal{Y}_{\pi'}^{\{n,n\}}$ ) are identical as in Fig. 3.

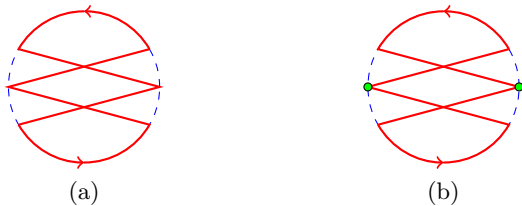


FIG. 3: Reduced diagrams of (a) and (b) are identical. The green circles in diagram (b) indicate that the states at those time steps are identical.

For  $\mathcal{T}$ -invariant systems with  $\mathcal{T}^2 = -1$ , we have the following theorem:

**Theorem 4:** For each reduced diagram, there exists either a diagram with minimal repetition of states or a diagram with two states at different time steps related by time reversal. These diagrams also have an identical reduced diagram.

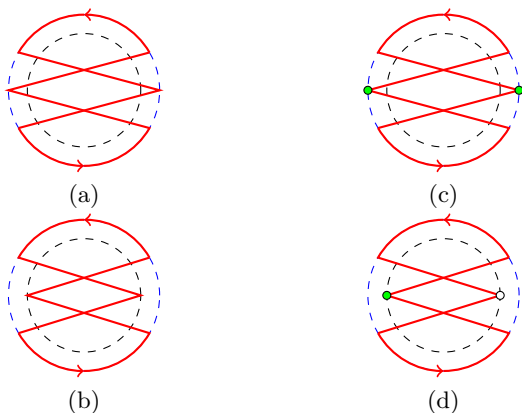


FIG. 4: Reduced diagrams of (a) and (c) are identical. Reduced diagrams of (b) and (d) are identical. The green circles in (c) indicate that the states at those time steps are identical. The green and white circle in (d) indicate that the states at those time steps are related by time reversal.

**Theorem 4** implies that for a given permutation  $\pi$  and configuration  $\vec{\sigma}$ , there exists another permutation  $\pi'$  such that Type I and Type II contribution of either  $\mathcal{Z}_{\pi,\vec{\sigma}}$

and  $\mathcal{Z}_{\pi',\vec{\sigma}}^{\{n,n\}}$  or  $\mathcal{Z}_{\pi,\vec{\sigma}}$  and  $\mathcal{Z}_{\pi',\vec{\sigma}}^{\{n,\mathcal{T}n\}}$  are identical as in Fig. 4. Following **Theorem 3** and **Theorem 4**, we identify diagrams whose reduced diagrams are not cancelled. Such diagrams give universal RMT form of SFF. We identify such diagrams determining SFF up to second order in  $t$  as shown in Sec. X-XI.

The SFF of physical chaotic systems takes the RMT SFF form only beyond  $t^*$ . To find the system-size scaling of  $t^*$ , we study strongly interacting fermionic chains with or without  $\mathcal{T}$ -symmetry in Sec. X. To study systems with  $\mathcal{T}^2 = 1$  and in the absence of  $\mathcal{T}$ -symmetry, we consider a chain of spinless fermions described by

$$\hat{H}_0^0 = \sum_{x=1}^L \epsilon_x \hat{n}_x + \sum_{x<y} \frac{U_0}{|x-y|^\alpha} \hat{n}_x \hat{n}_y, \quad (34)$$

$$\hat{H}_1^0 = \sum_{x<y} -J_{xy} \hat{c}_x^\dagger \hat{c}_y + \Delta_{xy} c_x^\dagger c_y^\dagger + h.c., \quad (35)$$

where the superscript 0 represents spinless fermions,  $\hat{n}_x \equiv \hat{c}_x^\dagger \hat{c}_x$ ,  $\hat{c}_x$  and  $\hat{c}_x^\dagger$  are, respectively, fermion occupation number, annihilation, and creation operators at site  $x$ . We take onsite energies  $\epsilon_1, \dots, \epsilon_L$  as Gaussian random numbers with zero mean and finite standard deviation of  $\Delta\epsilon$ . The hopping amplitude, denoted by  $J_{xy}$ , takes real or imaginary values according to the presence or absence of  $\mathcal{T}$ -symmetry. The pairing amplitude  $\Delta_{xy}$  takes only real values.

For  $\mathcal{T}$ -invariant systems with  $\mathcal{T}^2 = -1$ , we take a chain of interacting spin-1/2 fermions given as

$$\hat{H}_0^{1/2} = \sum_{x=1}^L \epsilon_x (\hat{n}_{x\uparrow} + \hat{n}_{x\downarrow}) + \sum_{x<y} \sum_{\sigma\sigma'} \frac{U_{xy}^{\sigma\sigma'}}{|x-y|^\alpha} \hat{n}_{x\sigma} \hat{n}_{y\sigma'} + \sum_{x=1}^L U_x \hat{n}_{x\uparrow} \hat{n}_{x\downarrow}, \quad (36)$$

$$\hat{H}_1^{1/2} = \sum_{x=1}^L \sum_{\sigma\sigma'} J_{\sigma\sigma'} \hat{c}_{x\sigma}^\dagger \hat{c}_{x+1\sigma'} + \Delta_{\sigma\sigma'} \hat{c}_{x\sigma}^\dagger \hat{c}_{x+1\sigma'}^\dagger + h.c., \quad (37)$$

where the superscript 1/2 stands for spin-1/2 fermions,  $\sigma = \uparrow, \downarrow$  represent the spin state along the  $z$ -axis,  $\hat{n}_{x\uparrow} \equiv \hat{c}_{x\uparrow}^\dagger \hat{c}_{x\uparrow}$  and  $\hat{n}_{x\downarrow} \equiv \hat{c}_{x\downarrow}^\dagger \hat{c}_{x\downarrow}$  are fermion occupation number operators at site  $x$  for spin states  $|\uparrow\rangle$  and  $|\downarrow\rangle$ , respectively. The operators  $\hat{c}_{x\sigma}$  and  $\hat{c}_{x\sigma}^\dagger$  are annihilation and creation operators of fermions at site  $x$  with spin  $\sigma$ . The long-range interaction parameters  $U_{ij}^{\sigma\sigma'}$  are all chosen as Gaussian random numbers with mean  $U_0$  and standard deviation  $\Delta U_0$  to ensure phases are only doubly degenerate due to the Kramers' degeneracy. The particle-particle repulsion  $U_x$  at a site  $x$  is also chosen as Gaussian random numbers with mean  $\bar{U}$  and standard deviation  $\Delta \bar{U}$ . Additionally, the annihilation operators of spin-1/2 fermions transform under  $\mathcal{T}$  as

$$\mathcal{T} \hat{c}_{x\uparrow} \mathcal{T}^{-1} = -\hat{c}_{x\downarrow}, \quad \mathcal{T} \hat{c}_{x\downarrow} \mathcal{T}^{-1} = \hat{c}_{x\uparrow}. \quad (38)$$

Thus,  $\hat{H}_0^{1/2}$  and  $\hat{H}_1^{1/2}$  are invariant under  $\mathcal{T}$  when  $U_{ij}^{\uparrow\uparrow} = U_{ij}^{\downarrow\downarrow}$ ,  $U_{ij}^{\uparrow\downarrow} = U_{ij}^{\downarrow\uparrow}$ ,  $J_{\downarrow\downarrow} = J_{\uparrow\uparrow}^*$ ,  $J_{\uparrow\downarrow} = -J_{\downarrow\uparrow}^*$ ,  $\Delta_{\downarrow\downarrow} = \Delta_{\uparrow\uparrow}^*$ , and  $\Delta_{\uparrow\downarrow} = -\Delta_{\downarrow\uparrow}^*$ . We also take PBC on real space for all the models by imposing  $\hat{c}_{x+L} \equiv \hat{c}_x$ ,  $\hat{c}_{x+L\sigma} \equiv \hat{c}_{x\sigma}$ , and replacing  $|x-y|$  by  $\min(|x-y|, L-|x-y|)$  in long-range interactions.

### III. OUTLINE OF THE RESULTS

We have identified the diagrams determining the universal RMT form of SFF up to two leading orders in time for all three Dyson's circular ensembles [9, 10]. Different system-size scaling of  $t^*$  have been found in recent years for various systems of COE and CUE classes with or without a  $U(1)$  symmetry [19, 21, 25, 26, 30, 37, 41]. There is hardly any result on interacting many-body quantum chaos of CSE class. We here provide a unified description of system-size scaling of  $t^*$  for all three Dyson's statistics in the presence or absence of a  $U(1)$  symmetry, which we summarize in Tab. II.

#### A. Leading-order SFF: Linear Ramp

The leading-order SFF is determined by the identity permutation and its variants. For  $\mathcal{T}$ -invariant systems with  $\mathcal{T}^2 = 1$ , there are  $t$  cyclic and  $t$  anticyclic permutations as variants of identity permutation. All these variants have identical contributions due to the symmetric nature of the matrix  $V$  as summarized in Tab. I, and PBC in time. Therefore, we find the leading-order SFF for the COE class by applying the rules in Sec. IV as

$$\begin{aligned} K_1^{(1)}(t) &= 2t \operatorname{tr} \mathcal{M}^t \\ &= 2t (1 + \lambda_1^t + \dots + \lambda_{\mathcal{N}-1}^t). \end{aligned} \quad (39)$$

Here,  $\mathcal{M}$  is a doubly stochastic (Markov) matrix given by  $\mathcal{M} = V \bullet V^*$ , where “ $\bullet$ ” represents the Hadamard product defined as  $(A \bullet B)_{i,j} = A_{i,j} B_{i,j}$ . The largest eigenvalue ( $\lambda_0$ ) of  $\mathcal{M}$  is one whereas other eigenvalues  $\lambda_1, \dots, \lambda_{\mathcal{N}-1}$  have magnitude less than one. The leading order in  $t$  contributions to the SFF can be physically interpreted using the Markov matrix as a return probability  $P_t(\underline{n}) = \langle \underline{n} | \mathcal{M}^t | \underline{n} \rangle$  to an initial state  $|\underline{n}\rangle$  after  $t$  time steps. Thus, we can write  $K_1^{(1)}(t) = 2t \sum_{\underline{n}} P_t(\underline{n})$ .

For systems in the absence of  $\mathcal{T}$ -symmetry, the contribution of cyclic variants differs from the anticyclic variants due to the non-symmetric nature of the matrix  $V$ . We thus get the leading-order SFF for the CUE class by applying the rules in Sec. V as

$$\begin{aligned} K_0^{(1)}(t) &= t (\operatorname{tr} \mathcal{M}^t + \operatorname{tr} \tilde{\mathcal{M}}^t) \\ &= t (1 + \lambda_1^t + \dots + \lambda_{\mathcal{N}-1}^t + \chi_0^t + \dots + \chi_{\mathcal{N}-1}^t), \end{aligned} \quad (40)$$

where  $\tilde{\mathcal{M}}$  is a complex Hermitian matrix defined by  $\tilde{\mathcal{M}} = V \bullet V^\dagger$ . The eigenvalues of  $\tilde{\mathcal{M}}$ ,  $\chi_0, \dots, \chi_{\mathcal{N}-1}$ , have magnitude less than one.

For  $\mathcal{T}$ -invariant systems with  $\mathcal{T}^2 = -1$ , each of the cyclic and anticyclic variant have further  $2^t$  variants corresponding to different configurations  $\vec{\sigma} = (\sigma_1, \dots, \sigma_t)$ . Analyzing their reduced diagrams, we find that only diagrams with  $\vec{\sigma} = (0, \dots, 0)$  or  $\vec{\sigma} = (1, \dots, 1)$  have non-vanishing contribution at long times leading to the SFF for the CSE class at leading order in  $t$  as

$$\begin{aligned} K_{-1}^{(1)}(t) &= 2t (\operatorname{tr} \mathcal{M}^t + \operatorname{tr} \tilde{\mathcal{M}}^t) \\ &= 2t (1 + \lambda_1^t + \dots + \lambda_{\mathcal{N}-1}^t + \chi_0^t + \dots + \chi_{\mathcal{N}-1}^t). \end{aligned} \quad (41)$$

The Thouless time  $t^*$  is determined by the second-largest eigenvalue  $\lambda_1$  of a doubly stochastic matrix  $\mathcal{M}$  for all three classes. Beyond  $t^*$ , we have  $K_1^{(1)} \simeq 2t$ ,  $K_0^{(1)} \simeq t$ , and  $K_{-1}^{(1)}(t) \simeq 2t$ , which are identical to the RMT predictions for these classes up to first order in  $t$ , Eqs. (2-4). We find that  $t^*$  is related to eigenvalue  $\lambda_1$  and its degeneracy  $d_1$  through

$$t^* \simeq \frac{\ln(d_1) + 1}{|\ln \lambda_1|}. \quad (42)$$

We determine the system-size of scaling of  $t^*$  in the presence or absence of a  $U(1)$  symmetry by studying the Hamiltonians Eqs. (34,35) for systems with  $\mathcal{T}^2 = 1$  and in the absence of  $\mathcal{T}$ -symmetry. To study the former case, we choose the hopping and pairing parameters as

$$J_{xy} = \begin{cases} J, & \text{if } |x-y| = 1, \\ 0, & \text{otherwise} \end{cases} \quad (43)$$

$$\Delta_{xy} = \begin{cases} \Delta, & \text{if } |x-y| = 1, \\ 0, & \text{otherwise} \end{cases} \quad (44)$$

where  $J$  and  $\Delta$  are real valued parameters. We break  $\mathcal{T}$ -symmetry by adding an imaginary next-nearest-neighbor hopping. So we consider the following parameters to investigate  $t^*$  for systems in the absence of  $\mathcal{T}$ -symmetry.

$$J_{xy} = \begin{cases} J, & \text{if } |x-y| = 1, \\ ig, & \text{if } |x-y| = 2, \\ 0, & \text{otherwise} \end{cases} \quad (45)$$

$$\Delta_{xy} = \begin{cases} \Delta, & \text{if } |x-y| = 1, \\ \Delta', & \text{if } |x-y| = 2, \\ 0, & \text{otherwise} \end{cases} \quad (46)$$

where  $J, g, \Delta$  and  $\Delta'$  are real valued parameters. We explore a chain of strongly interacting spin-1/2 fermions in Eqs. (36,37) to determine  $t^*$  for  $\mathcal{T}$ -invariant systems with  $\mathcal{T}^2 = -1$ . We obtain different system-size scaling of  $t^*$  for various choices of parameters in all three classes as summarized in Tab. II. While the second-largest eigenvalue  $\lambda_1$  of  $\mathcal{M}$  determines when the universal RMT SFF

	Parameters ( $\beta$ )	Symmetry	$\lambda_1$ in thermodynamic limit	Degeneracy, $d_1$	Thouless time, $t^*$
$\mathcal{T}^2 = 1$	$J \neq 0, \Delta = 0$	$[\tilde{H}(t), \tilde{N}] = 0$	$1 - c_\beta/L^2$	$\mathcal{O}(L^0)$	$\mathcal{O}(L^2)$
	$J \neq \Delta \neq 0$	$[\tilde{H}(t), \tilde{N}] \neq 0$	$\mathcal{O}(L^0)$	$\mathcal{O}(L^0)$	$\mathcal{O}(L^0)$
	$ J  =  \Delta  \neq 0$	$[\tilde{H}(t), \tilde{N}] \neq 0$	$\mathcal{O}(L^0)$	$\mathcal{O}(L^2)$	$\mathcal{O}(\ln L)$
	$J = 0, \Delta \neq 0$	$[\tilde{H}(t), \tilde{N}_s] = 0$	$1 - c_\beta/L^2$	$\mathcal{O}(L^0)$	$\mathcal{O}(L^2)$
Absence of $\mathcal{T}$ -symmetry	$J, g \neq 0; \Delta, \Delta' = 0$	$[\tilde{H}(t), \tilde{N}] = 0$	$1 - c_\beta/L^2$	$\mathcal{O}(L^0)$	$\mathcal{O}(L^2)$
	$J, g \neq 0; \Delta, \Delta' \neq 0$	$[\tilde{H}(t), \tilde{N}] \neq 0$	$\mathcal{O}(L^0)$	$\mathcal{O}(L^0)$	$\mathcal{O}(L^0)$
	$ J  =  \Delta ,  g  =  \Delta' $	$[\tilde{H}(t), \tilde{N}] \neq 0$	$\mathcal{O}(L^0)$	$\mathcal{O}(L)$	$\mathcal{O}(\ln L)$
$\mathcal{T}^2 = -1$	$J_{\sigma\sigma'} \neq 0; \Delta_{\sigma\sigma'} = 0$	$[\tilde{H}(t), \tilde{N}_t] = 0$	$1 - c_\beta/L^2$	$\mathcal{O}(L^0)$	$\mathcal{O}(L^2)$
	$J_{\sigma\sigma'} \neq 0, \Delta_{\sigma\sigma'} \neq 0$	$[\tilde{H}(t), \tilde{N}_t] \neq 0$	$\mathcal{O}(L^0)$	$\mathcal{O}(L^0)$	$\mathcal{O}(L^0)$
	$ J_{\sigma\sigma'}  =  \Delta_{\sigma\sigma'} $	$[\tilde{H}(t), \tilde{N}_t] \neq 0$	$\mathcal{O}(L^0)$	$\mathcal{O}(L)$	$\mathcal{O}(\ln L)$

TABLE II: System-size scaling of Thouless time ( $t^*$ ) for periodically kicked strongly interacting fermionic chains of length  $L$  with or without time reversal ( $\mathcal{T}$ ) symmetry. The operators  $\tilde{N} = \sum_{x=1}^L \hat{n}_x$  and  $\tilde{N}_t = \sum_{x=1}^L \sum_{\sigma} \hat{n}_{x\sigma}$  denote the total fermion number for spinless and spinful model, respectively, and  $\tilde{N}_s = \sum_{x=1}^L (-1)^x \hat{n}_x$  is the staggered fermion number for even  $L$ . The presence or absence of a  $U(1)$  symmetry can be found by their commutation with the chain's Hamiltonian  $\tilde{H}(t)$ .

form would emerge for all three classes, the other eigenvalues of  $\mathcal{M}$  and  $\tilde{\mathcal{M}}$  fix the nonuniversal behavior of the SFF at short timescales for any physical systems. We have shown a nice comparison between the SFF obtained within the RPA and that from direct numerics in Fig. 28 both at short and long times for a  $\mathcal{T}$ -invariant model with  $\mathcal{T}^2 = 1$ .

### B. Second-order correction

The second-order term in the RMT SFF is inversely proportional to the Hilbert space dimension  $\mathcal{N}$  for  $\mathcal{T}^2 = \pm 1$  and such term is absent in the absence of  $\mathcal{T}$ -symmetry. From the Type I term for different permutations, we find that the following permutations and their variants contribute to the second-order correction in the SFF. These are (1) single transpositions ( $T$ ) defined as the interchange of any two states in  $\{\underline{n}_1, \dots, \underline{n}_t\}$ , (2) sub-sequence reversal ( $S$ ) defined as reversal of the order of states between two-time steps, (3) identity permutation with a state repeated twice ( $R$ ) and (4) sub-sequence reversal with a state repeated twice ( $SR$ ). The last permutation reverses the order of states between the two appearances of the repeated state.

Analyzing reduced diagrams for these permutations, we find that the reduced diagrams of  $T$  and  $R$  are exactly identical for all three Dyson classes. This implies that the Type I and Type II contributions of these permutations exactly cancel each other. Similarly, the reduced diagrams of  $S$  are canceled by the reduced diagrams of  $SR$ . However, there are two extra  $SR$  diagrams with long red arcs. Computing all the variants of these diagrams, we obtain the second-order RMT correction to the SFF for all three Dyson classes:

$$K_1^{(2)}(t) = -\frac{2t^2}{\mathcal{N}} + \mathcal{O}(\lambda_1^t), \quad (47)$$

$$K_0^{(2)}(t) = \mathcal{O}(\lambda_1^t, \chi_0^t), \quad (48)$$

$$K_{-1}^{(2)}(t) = \frac{2t^2}{\mathcal{N}} + \mathcal{O}(\lambda_1^t, \chi_0^t). \quad (49)$$

In an alternative diagrammatic representation, the extra  $SR$  diagrams resemble the Sieber-Richter pairs of near-miss and self-crossing orbits [12, 13]. Nevertheless, there are specific differences in these diagrams as we are studying quantum systems here on a discrete Hilbert space compared to semiclassical periodic orbit theory on continuous phase space. We further notice that the nonuniversal terms at second order in  $t$  of our calculated SFF do not contribute significantly to the short-time nonuniversal behavior of SFF when we compare the SFF computed within the RPA and that from direct numerics, Fig. 28.

### IV. RULES TO CALCULATE $\mathcal{X}_\pi$ AND $\mathcal{X}_\pi^{\{\underline{n}, \underline{n}\}}$

We now enumerate some rules, which can be applied to find  $\mathcal{X}_\pi$  and  $\mathcal{X}_\pi^{\{\underline{n}, \underline{n}\}}$  for  $\mathcal{T}$ -invariant systems with  $\mathcal{T}^2 = 1$ . The rules are:

(i) First draw a diagram representing a permutation  $\pi$  (e.g., a sub-sequence reversal shown in Fig. 5).

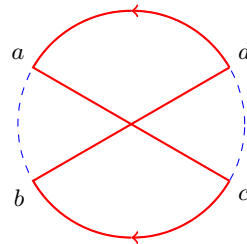
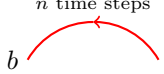
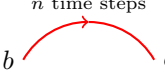


FIG. 5: A diagram representing a sub-sequence reversal which reverses the order of states from  $\tau_1$  to  $\tau_2$ . States at time steps  $\tau_1$  and  $\tau_2$  are denoted by the labels  $b$  and  $c$ ,  $b \equiv \underline{n}_{\tau_1}, c \equiv \underline{n}_{\tau_2}$ . The other labels  $a$  and  $d$  denote states at the corresponding time steps,  $a \equiv \underline{n}_{\tau_1-1}, d \equiv \underline{n}_{\tau_2+1}$ .

(ii) Denote a state repeated twice by green circles, “ $\bullet$ ”, at the corresponding time steps (e.g., Fig. 3b).

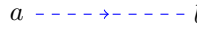





(iii) For a red arc of length  $n$  time steps, insert a factor as

  $\equiv$    $\equiv (\mathcal{M}^n)_{a,b}$ . The matrix  $\mathcal{M}$  is symmetric due to the symmetric unitary property of the matrix  $V$ . Thus, performing eigendecomposition of  $\mathcal{M}$ , we obtain

$$(\mathcal{M}^n)_{a,b} = \sum_{i=0}^{\mathcal{N}-1} \lambda_i^n \mathcal{M}_{a,b}^{(i)}, \quad (50)$$

where  $\lambda_i$  are eigenvalues of  $\mathcal{M}$ , such that  $\lambda_0 = 1 \geq |\lambda_1| \geq \dots \geq |\lambda_{\mathcal{N}-1}|$ , [26], and  $\mathcal{M}^{(i)} = |\lambda_i\rangle\langle\lambda_i|$ . The state  $|\lambda_i\rangle$  is an eigenvector of  $\mathcal{M}$  corresponding to eigenvalue  $\lambda_i$ .

(iv)   $\equiv$    $\equiv V_{a,b}$ .

(v)   $\equiv$    $\equiv V_{a,b}^*$ .

(vi) Take a sum over all the matrix indices repeated twice or more.

We derive the above rules in App. A. Applying the above rules, we evaluate the contribution  $\mathcal{X}_S$  of a sub-sequence reversal described in Fig. 5 as

$$\begin{aligned} \mathcal{X}_S &= \left( \sum_{i=1}^{\mathcal{N}-1} \lambda_i^{\nu_1} \mathcal{M}_{d,a}^{(i)} \right) \left( \sum_{j=0}^{\mathcal{N}-1} \lambda_j^{\nu_2} \mathcal{M}_{b,c}^{(j)} \right) \\ &\quad \times V_{a,b} V_{c,d} V_{a,c}^* V_{b,d}^*, \\ &= \sum_{i,j=0}^{\mathcal{N}-1} \lambda_i^{\nu_1} \lambda_j^{\nu_2} Q_S^{ij}, \end{aligned} \quad (51)$$

where  $Q_S^{ij} = \mathcal{M}_{d,a}^{(i)} \mathcal{M}_{b,c}^{(j)} V_{a,b} V_{c,d} V_{a,c}^* V_{b,d}^*$ , and  $\nu_1 = t - \tau_2 + \tau_1 - 2$  and  $\nu_2 = \tau_2 - \tau_1$  are the lengths of upper and lower red arcs of Fig. 5 measured in units of the kicking period  $\tau_p$ .

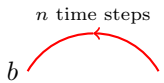
## V. RULES TO CALCULATE $\mathcal{Y}_\pi$ AND $\mathcal{Y}_\pi^{\{n,n\}}$

We here list the rules for finding  $\mathcal{Y}_\pi$  and  $\mathcal{Y}_\pi^{\{n,n\}}$  for systems in the absence of  $\mathcal{T}$ -symmetry.

(i) First draw a diagram representing a permutation  $\pi$  (e.g., a sub-sequence reversal shown in Fig. 5).

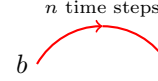
(ii) Represent a state repeated twice by green circles, “●”, at the corresponding time steps (e.g., Fig. 3b).

(iii) For a red arc of length  $n$  time steps with a counterclockwise arrow, insert a factor as

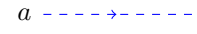

  $\equiv (\mathcal{M}^n)_{a,b} = \sum_{i=0}^{\mathcal{N}-1} \lambda_i^n \mathcal{M}_{a,b}^{(i)}$ . The doubly stochastic matrix  $\mathcal{M}$  is non-symmetric due to the non-symmetric nature of the matrix  $V$ , thus,  $\mathcal{M}^{(i)} =$



${}_R|\lambda_i\rangle\langle\lambda_i|_L$ , where  ${}_R|\lambda_i\rangle$  and  $\langle\lambda_i|_L$  are the right and left eigenvectors of  $\mathcal{M}$  with an eigenvalue  $\lambda_i$ .

(iv) For a red arc of length  $n$  time steps with a clockwise arrow insert

  $\equiv (\tilde{\mathcal{M}}^n)_{a,b} = \sum_{i=0}^{\mathcal{N}-1} \lambda_i^n \tilde{\mathcal{M}}_{a,b}^{(i)}$ . The

matrix  $\tilde{\mathcal{M}}$  is complex Hermitian with eigenvalues,  $\chi_0, \chi_1, \dots, \chi_{\mathcal{N}-1}$ , satisfying  $1 > |\chi_0| \geq |\chi_1| \geq \dots \geq |\chi_{\mathcal{N}-1}|$  (following the Geršgorin circle theorem as we explain in App. B), and  $\tilde{\mathcal{M}}^{(i)} = |\chi_i\rangle\langle\chi_i|$ , where  $|\chi_i\rangle$  is an eigenvector of  $\tilde{\mathcal{M}}$  corresponding to eigenvalue  $\chi_i$ .

(v)   $\equiv V_{a,b}$ ,   $\equiv V_{b,a}$ .

(vi)   $\equiv V_{a,b}^*$ ,   $\equiv V_{b,a}^*$ .

(vii) Take sum over all the matrix indices, which are repeated twice or more.

We give a derivation of the above rules in App. C. We can apply the above rules to evaluate the contribution  $\mathcal{Y}_S$  of a sub-sequence reversal described in Fig. 5 as

$$\mathcal{Y}_S = \sum_{i,j=0}^{\mathcal{N}-1} \lambda_i^{\nu_1} \lambda_j^{\nu_2} Q_S^{ij}, \quad (52)$$

where  $Q_S^{ij} = \mathcal{M}_{d,a}^{(i)} \tilde{\mathcal{M}}_{b,c}^{(j)} V_{a,b} V_{c,d} V_{a,c}^* V_{b,d}^*$ , and  $\nu_1, \nu_2$  are the same as in Sec. IV. As mentioned in the rules above, the contribution of red arcs with counterclockwise and clockwise arrows is different when  $\mathcal{T}$ -symmetry is absent, therefore, we separate their indices by a semicolon, as in  $Q_S^{i;j}$ .

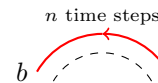
## VI. RULES TO CALCULATE $\mathcal{Z}_{\pi,\bar{\sigma}}, \mathcal{Z}_{\pi,\bar{\sigma}}^{\{n,n\}}$ , AND $\mathcal{Z}_{\pi,\bar{\sigma}}^{\{n,\mathcal{T}n\}}$

We give the rules for evaluating  $\mathcal{Z}_{\pi,\bar{\sigma}}, \mathcal{Z}_{\pi,\bar{\sigma}}^{\{n,n\}}$ , and  $\mathcal{Z}_{\pi,\bar{\sigma}}^{\{n,\mathcal{T}n\}}$  for  $\mathcal{T}$ -invariant systems with  $\mathcal{T}^2 = -1$ . The rules are:

(i) Draw a dashed blue circle representing initial states  $\{\underline{n}_1, \dots, \underline{n}_t\}$  and a concentric dashed black circle of smaller radius denoting the time-reversed states  $\{\mathcal{T}\underline{n}_1, \dots, \mathcal{T}\underline{n}_t\}$ . Draw next the red curve representing a permutation  $\pi$  and a configuration  $\bar{\sigma}$  (e.g., Fig. 6).

(ii) Draw green circles, “●”, for a state repeated twice at the corresponding time steps (e.g., Fig. 4c). Draw green and white circles, “○”, for two states related by  $\mathcal{T}$  at the corresponding time steps (e.g., Fig. 4d).

(iii) For a red arc of length  $n$  time steps with a counterclockwise arrow on the outer circle, insert a factor as

  $\equiv (\mathcal{M}^n)_{a,b} = \sum_{i=0}^{\mathcal{N}-1} \lambda_i^n \mathcal{M}_{a,b}^{(i)}$ . The doubly stochastic matrix  $\mathcal{M}$  is non-symmetric due to the non-symmetric nature of the matrix  $V$ , thus,  $\mathcal{M}^{(i)} =$

${}_R|\lambda_i\rangle\langle\lambda_i|_L$ , where  ${}_R|\lambda_i\rangle$  and  $\langle\lambda_i|_L$  are respectively the right and left eigenvectors of  $\mathcal{M}$  corresponding to eigenvalue  $\lambda_i$ .

(iv) For a red arc of length  $n$  time steps with a clockwise arrow on the outer circle, insert a factor as

$$b \overset{n \text{ time steps}}{\curvearrowright} a \equiv \left( \tilde{\mathcal{M}}^n \right)_{a,b} = \sum_{i=0}^{\mathcal{N}-1} \chi_i^n \tilde{\mathcal{M}}_{a,b}^{(i)}. \quad \text{The}$$

matrix  $\tilde{\mathcal{M}}$  is complex Hermitian with eigenvalues  $\chi_0, \dots, \chi_{\mathcal{N}-1}$  satisfying  $1 > |\chi_0| \geq |\chi_1| \geq \dots \geq |\chi_{\mathcal{N}-1}|$  (again following the Geršgorin circle theorem as discussed in App. B), and  $\tilde{\mathcal{M}}^{(i)} = |\chi_i\rangle\langle\chi_i|$ , where  $|\chi_i\rangle$  is an eigenvector of  $\tilde{\mathcal{M}}$  corresponding to eigenvalue  $\chi_i$ .

(v) For a red arc with a clockwise arrow on the inner circle, insert a factor as

$$b \overset{n \text{ time steps}}{\curvearrowright} a \equiv (\mathcal{M}^n)_{a,b} = \sum_{i=0}^{\mathcal{N}-1} \lambda_i^n \mathcal{M}_{a,b}^{(i)}.$$

(vi) For a red arc with a counterclockwise arrow on the inner circle, insert a factor as

$$b \overset{n \text{ time steps}}{\curvearrowleft} a \equiv \left( \tilde{\mathcal{M}}^n \right)_{a,b} = \sum_{i=0}^{\mathcal{N}-1} \chi_i^n \tilde{\mathcal{M}}_{a,b}^{(i)}.$$

(vii)  $a \overset{\text{---}}{\curvearrowright} b \equiv V_{a,b}$ ,  $a \overset{\text{---}}{\curvearrowleft} b \equiv V_{b,a}$ .

(viii)  $a \overset{\text{---}}{\curvearrowright} b \equiv V_{a,b}^*$ ,  $a \overset{\text{---}}{\curvearrowleft} b \equiv V_{b,a}^*$ .

(ix) Take sum over all the matrix indices, which are repeated twice or more.

Since the matrix  $V$  is non-symmetric in the computational basis, the rules here are identical to those in Sec. V for systems in the absence of  $\mathcal{T}$ -symmetry except the rules (v) and (vi), which follow naturally from the **Theorem 1**. Following the above rules, the contribution  $\mathcal{Z}_{T,\vec{\sigma}}$  of a transposition with configuration  $\vec{\sigma}$  as shown in Fig. 6 can be expressed as

$$\mathcal{Z}_{T,\vec{\sigma}} = \sum_{i,j=0}^{\mathcal{N}-1} \lambda_i^{\nu_1} \chi_j^{\nu_2} Q_T^{i;j;j}, \quad (53)$$

where

$$Q_T^{i;j;j} = \mathcal{M}_{f,a}^{(i)} \tilde{\mathcal{M}}_{c,d}^{(j)} V_{a,b} V_{b,c} V_{d,e} V_{e,f} V_{ae}^* V_{e,Tc}^* V_{Td,b}^* V_{b,f}^*, \quad (54)$$

and  $\nu_1, \nu_2$  are the same as in Sec. IV. In general,  $i_1, i_2, i_3$  and  $i_4$  in the superscript of  $Q_\pi^{i_1;i_2;i_3;i_4}$  represent, respectively, the indices coming from red arcs with counterclockwise arrow on the outer circle, the indices coming from red arcs with clockwise arrow on the outer circle, the indices coming from red arcs with counterclockwise arrow on the inner circle, and the indices coming from red arcs with clockwise arrow on the inner circle. Since, Fig. 53 does not contain arcs with clockwise arrow on the inner or outer circle,  $Q_T^{i;j;j}$  contains empty slots, separated by semicolon, for such arcs.

## VII. PROOF OF THEOREM 2

We now prove the **Theorem 2** in Sec. II for all three cases of  $\mathcal{T}$ -symmetry.

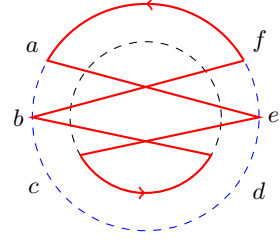


FIG. 6: A diagram representing a transposition of states at time steps  $\tau_1$  and  $\tau_2$  with  $\vec{\sigma} = (\sigma_1, \dots, \sigma_t)$  such that  $\sigma_\tau = 1$  for  $\tau \in [\tau_1 + 1, \tau_2 - 1]$  and  $\sigma_\tau = 0$  for  $\tau \notin [\tau_1 + 1, \tau_2 - 1]$ . The labels at the vertices denote states on the blue circle at those time steps,  $a \equiv \underline{n}_{\tau_1-1}$ ,  $b \equiv \underline{n}_{\tau_1}$ ,  $c \equiv \underline{n}_{\tau_1+1}$ ,  $d \equiv \underline{n}_{\tau_2-1}$ ,  $e \equiv \underline{n}_{\tau_2}$ ,  $f \equiv \underline{n}_{\tau_2+1}$ . The labels  $b$  and  $e$  represent the transposed states.

### A. $\mathcal{T}^2 = 1$

We first consider a permutation  $\pi$ , whose diagram contains number  $r$  of red arcs of lengths  $\nu_1, \dots, \nu_r$  with no repetition of states. Following the rules in Sec. IV, the contribution to SFF can be written similar to Eq. (51) as

$$\mathcal{X}_\pi = \sum_{\{i_q\}} \left( \prod_{q=1}^r \lambda_{i_q}^{\nu_q} \right) Q_\pi^{i_1 \dots i_r}, \quad (55)$$

where  $\sum_{\{i_q\}} = \sum_{i_1, \dots, i_r}$  with  $i_q = 0, \dots, \mathcal{N} - 1$ ,  $\forall q$ . For a nontrivial permutation, such as the one shown in Fig. 5, some of the red line segments do not overlap with the blue circle. Let  $\delta$  be the total number of such red line segments. Then, we have

$$\sum_q \nu_q = t - \delta. \quad (56)$$

In Eq. (55), the factor  $\left( \prod_{q=1}^r \lambda_{i_q}^{\nu_q} \right)$  determines the behavior of different terms at long time as  $|\lambda_{i_q}| < 1$  when  $i_q \neq 0$  and  $\lambda_{i_q} = 1$  when  $i_q = 0$ . Thus, all the terms in Eq. (55) can be divided into three different categories as following.

**Case 1:**  $i_q = 0, \forall q$ . Since  $\lambda_0 = 1$ , the right side of Eq. (55) gives the term  $Q_\pi^{0 \dots 0}$ , which is a function of  $\mathcal{M}^{(0)}$ ,  $V$  and  $V^*$ . Since  $\mathcal{M}$  is a doubly stochastic matrix, we have  $\langle \lambda_0 \rangle \equiv (1/\sqrt{\mathcal{N}})(1 \dots 1)$ . Therefore, all the matrix elements of  $\mathcal{M}^{(0)}$  are  $1/\mathcal{N}$ . A study of different permutations reveals that  $Q_\pi^{0 \dots 0}$  can typically be simplified to the form  $1/\mathcal{N}^\mu$  (check App. D), where  $\mu$  is a non-negative integer. The absence of Hamiltonian parameters implies that this is a universal term. This is the Type I term in the **Theorem 2**. If  $Q_\pi^{0 \dots 0}$  can not be simplified to a form independent of Hamiltonian parameters, the term is nonuniversal and considered as a Type II term because it remains finite at long times.

**Case 2:**  $i_q \neq 0, \forall q$ . In this case,  $|\lambda_{i_q}| < 1, \forall q$ , so  $\prod_{q=1}^r \lambda_{i_q}^{\nu_q}$  can be interpreted as a product of  $(t - \delta)$  real numbers of magnitude less than one. Thus, it decays exponentially with  $t$ . Therefore, such terms are Type III.

**Case 3:** All the remaining terms involve at least one  $i_{q'} = 0$  and at least one  $i_{q''} \neq 0$ . Thus, we can divide the set  $\{1, \dots, r\}$  into two subsets  $Q_1 = \{q'_1, \dots, q'_{r_1}\}$  and  $Q_2 = \{q''_1, \dots, q''_{r_2}\}$  with  $r_1, r_2 \geq 1$  and  $r_1 + r_2 = r$ , such that,  $i_q = 0, \forall q \in Q_1$  and  $i_q \neq 0, \forall q \in Q_2$ . Therefore,

$$\prod_{q=1}^r \lambda_{i_q}^{\nu_q} = \left( \prod_{q \in Q_1} \lambda_0^{\nu_q} \right) \left( \prod_{q \in Q_2} \lambda_{i_q}^{\nu_q} \right) = \prod_{q \in Q_2} \lambda_{i_q}^{\nu_q}. \quad (57)$$

Since  $\sum_{q=1}^r \nu_q = t - \delta$ ,  $\sum_{q=1}^r \nu_q$  diverges with increasing time. We can further write  $\sum_{q=1}^r \nu_q = \sum_{q \in Q_1} \nu_q + \sum_{q \in Q_2} \nu_q$ . Therefore,  $\sum_{q \in Q_2} \nu_q$  exhibits two possible behaviors in the long time limit: (a) it diverges, or (b) it remains finite. Consequently,  $\prod_{q=1}^r \lambda_{i_q}^{\nu_q}$  falls exponentially at long times for case (a), and it remains finite in case (b). We substitute the long-time form of  $\prod_{q=1}^r \lambda_{i_q}^{\nu_q}$  in Eq. (55) to find that the terms with case (a) behavior fall exponentially with time, and the terms with case (b) behavior diverge. Therefore, the case (a) terms are Type III and the case (b) terms, as they depend on the Hamiltonian parameters, are Type II.

Therefore,  $\mathcal{X}_\pi$  can be expressed as a sum of Type I, Type II, and Type III terms in accordance with **Theorem 2**. A similar analysis can be performed to show that **Theorem 2** is also valid for  $\mathcal{X}_\pi^{\{n, \bar{n}\}}$ .

## B. Absence of $\mathcal{T}$ -symmetry

We now consider a permutation  $\pi$ , whose diagram contains  $r$  number of red arcs with counterclockwise arrows and lengths  $\nu_1, \dots, \nu_r$ , and  $\tilde{r}$  number of red arcs with clockwise arrows and lengths  $\tilde{\nu}_1, \dots, \tilde{\nu}_{\tilde{r}}$ . Following the rules in Sec. V, the contribution to SFF can be written similar to Eq. (52):

$$\mathcal{Y}_\pi = \sum_{\{i_q\}} \sum_{\{\tilde{i}_q\}} \left( \prod_{q=1}^r \lambda_{i_q}^{\nu_q} \right) \left( \prod_{q=1}^{\tilde{r}} \chi_{\tilde{i}_q}^{\tilde{\nu}_q} \right) \times Q_\pi^{i_1 \dots i_r; \tilde{i}_1 \dots \tilde{i}_{\tilde{r}}}, \quad (58)$$

where

$$\sum_{q=1}^r \nu_q + \sum_{q=1}^{\tilde{r}} \tilde{\nu}_q = t - \delta. \quad (59)$$

Since  $|\chi_i| < 1$  for  $i = 0, \dots, \mathcal{N} - 1$ ,  $|\lambda_i| < 1$  for  $i = 1, \dots, \mathcal{N} - 1$ , and  $\lambda_0 = 1$ , all the terms in Eq. (58) can be categorized as following.

**Case 1:**  $\tilde{r} = 0$  and  $i_q = 0, \forall q$ . The right-hand side of Eq. (58) gives the term  $Q_\pi^{0 \dots 0}$ . Like the  $\mathcal{T} = 1$  case, typically,  $Q_\pi^{0 \dots 0} = 1/\mathcal{N}^\mu$ , where  $\mu$  is a non-negative integer and thus it leads to a Type I term. If  $Q_\pi^{0 \dots 0}$  can not be simplified to a form independent of the Hamiltonian parameters, it is a Type II term.

**Case 2:**  $i_q \neq 0, \forall q$  or  $r = 0$ . In this case, the factor  $\left( \prod_{q=1}^r \lambda_{i_q}^{\nu_q} \right) \left( \prod_{q=1}^{\tilde{r}} \chi_{\tilde{i}_q}^{\tilde{\nu}_q} \right)$  in Eq. (58) is a product of  $(t - \delta)$  real or complex numbers of magnitude less than one. Therefore, the corresponding terms fall exponentially with time. Such terms are Type III.

**Case 3:** All the remaining terms have at least one  $i_q = 0$ , and if  $\tilde{r} = 0$ , then at least one  $i_q \neq 0$ . Therefore, the set  $\{1, \dots, r\}$  can be divided into two subsets  $Q_1 = \{q | i_q = 0\}$  and  $Q_2 = \{q | i_q \neq 0\}$ . We have

$$\sum_{q=1}^r \nu_q + \sum_{q=1}^{\tilde{r}} \tilde{\nu}_q = \sum_{q \in Q_1} \nu_q + \sum_{q \in Q_2} \nu_q + \sum_{q=1}^{\tilde{r}} \tilde{\nu}_q = t - \delta, \quad (60)$$

and

$$\left( \prod_{q=1}^r \lambda_{i_q}^{\nu_q} \right) \left( \prod_{q=1}^{\tilde{r}} \chi_{\tilde{i}_q}^{\tilde{\nu}_q} \right) = \left( \prod_{q \in Q_1} \lambda_0^{\nu_q} \prod_{q \in Q_2} \lambda_{i_q}^{\nu_q} \right) \left( \prod_{q=1}^{\tilde{r}} \chi_{\tilde{i}_q}^{\tilde{\nu}_q} \right) = \left( \prod_{q \in Q_2} \lambda_{i_q}^{\nu_q} \right) \left( \prod_{q=1}^{\tilde{r}} \chi_{\tilde{i}_q}^{\tilde{\nu}_q} \right). \quad (61)$$

Thus,  $\left( \prod_{q=1}^r \lambda_{i_q}^{\nu_q} \right) \left( \prod_{q=1}^{\tilde{r}} \chi_{\tilde{i}_q}^{\tilde{\nu}_q} \right)$  can be interpreted as a product of  $(\sum_{q \in Q_2} \nu_q + \sum_{q=1}^{\tilde{r}} \tilde{\nu}_q)$  real or complex numbers of magnitude less than one. Therefore, when  $\sum_{q \in Q_2} \nu_q + \sum_{q=1}^{\tilde{r}} \tilde{\nu}_q$  diverges with time, the corresponding terms in Eq. (58) decay exponentially with time. When  $\sum_{q \in Q_2} \nu_q + \sum_{q=1}^{\tilde{r}} \tilde{\nu}_q$  remains finite at long times, the corresponding terms in Eq. (58) also remain finite. Thus, this case includes both Type II and Type III terms. The above analysis can be extended to demonstrate that **Theorem 2** is also valid for  $\mathcal{Y}_\pi^{\{n, \bar{n}\}}$ .

## C. $\mathcal{T}^2 = -1$

We here take a permutation  $\pi$  and a configuration  $\vec{\sigma}$ , whose diagram contains  $r_o$  number of red arcs on the outer circle with counterclockwise arrows and lengths  $\nu_1, \dots, \nu_{r_o}$ ,  $\tilde{r}_o$  number of red arcs on the outer circle with clockwise arrows and lengths  $\tilde{\nu}_1, \dots, \tilde{\nu}_{\tilde{r}_o}$ ,  $r_i$  number of red arcs on the inner circle with counterclockwise arrows and lengths  $\xi_1, \dots, \xi_{r_i}$ , and  $\tilde{r}_i$  number of red arcs on the inner circle with clockwise arrows and lengths  $\tilde{\xi}_1, \dots, \tilde{\xi}_{\tilde{r}_i}$ . Following the rules in Sec. VI, the contribution to SFF can be written following Eq. (53) as

$$\mathcal{Z}_{\pi, \vec{\sigma}} = \sum_{\{i_q\}} \sum_{\{\tilde{i}_q\}} \sum_{\{j_q\}} \sum_{\{\tilde{j}_q\}} \times \left( \prod_{q=1}^{r_o} \lambda_{i_q}^{\nu_q} \right) \left( \prod_{q=1}^{\tilde{r}_o} \chi_{\tilde{i}_q}^{\tilde{\nu}_q} \right) \left( \prod_{q=1}^{r_i} \chi_{j_q}^{\xi_q} \right) \left( \prod_{q=1}^{\tilde{r}_i} \lambda_{\tilde{j}_q}^{\tilde{\xi}_q} \right) \times Q_\pi^{i_1 \dots i_{r_o}; \tilde{i}_1 \dots \tilde{i}_{\tilde{r}_o}; j_1 \dots j_{r_i}; \tilde{j}_1 \dots \tilde{j}_{\tilde{r}_i}}, \quad (62)$$

where the sum of lengths of all the red arcs satisfy

$$\sum_{q=1}^{r_o} \nu_q + \sum_{q=1}^{\tilde{r}_o} \tilde{\nu}_q + \sum_{q=1}^{r_i} \xi_q + \sum_{q=1}^{\tilde{r}_i} \tilde{\xi}_q = t - \delta. \quad (63)$$

Similar to the case without  $\mathcal{T}$ -symmetry in Eq. (58), the different terms on the right-hand side of Eq. (62) can be categorized as follows:

**Case 1:**  $\tilde{r}_o = 0$ ,  $r_i = 0$ , and  $i_q = 0$  and  $j_q = 0$ ,  $\forall q$ . The right-hand side of Eq. (62) gives the term  $Q_\pi^{0\dots 0;0;\dots 0}$ . Similar to  $\mathcal{T}^2 = 1$  and without  $\mathcal{T}$ -symmetry cases, typically  $Q_\pi^{0\dots 0;0;\dots 0} = 1/\mathcal{N}^\mu$ , where  $\mu$  is a non-negative integer. Therefore, this is a Type I term. If  $Q_\pi^{0\dots 0;0;\dots 0}$  can not be simplified to a form independent of Hamiltonian parameters, it is a Type II term.

**Case 2:**  $i_q \neq 0$  and  $j_q \neq 0$ ,  $\forall q$  or  $r_o = \tilde{r}_i = 0$ . The factor  $\left(\prod_{q=1}^{r_o} \lambda_{i_q}^{\nu_q}\right) \left(\prod_{q=1}^{\tilde{r}_o} \chi_{\tilde{i}_q}^{\tilde{\nu}_q}\right) \left(\prod_{q=1}^{r_i} \chi_{j_q}^{\xi_q}\right) \left(\prod_{q=1}^{\tilde{r}_i} \lambda_{\tilde{j}_q}^{\tilde{\xi}_q}\right)$  can be interpreted as a product of  $(t - \delta)$  real or complex numbers of magnitude less than one. Therefore, the corresponding terms fall exponentially with time. Consequently, such terms are Type III.

**Case 3:** All the remaining terms have at least one  $i_q = 0$  or at least one  $\tilde{j}_q = 0$ , and if  $\tilde{r}_o = r_i = 0$  then at least one  $i_q \neq 0$  or at least one  $\tilde{j}_q \neq 0$ . Therefore, the set  $\{1, \dots, r_o\}$  can be divided into two subsets  $Q_{o,1} = \{q | i_q = 0\}$  and  $Q_{o,2} = \{q | i_q \neq 0\}$ . Similarly, the set  $\{1, \dots, \tilde{r}_i\}$  can be divided into two subsets  $Q_{i,1} = \{q | \tilde{j}_q = 0\}$  and  $Q_{i,2} = \{q | \tilde{j}_q \neq 0\}$ . Thus, we have

$$\begin{aligned} & \left(\prod_{q=1}^{r_o} \lambda_{i_q}^{\nu_q}\right) \left(\prod_{q=1}^{\tilde{r}_o} \chi_{\tilde{i}_q}^{\tilde{\nu}_q}\right) \left(\prod_{q=1}^{r_i} \chi_{j_q}^{\xi_q}\right) \left(\prod_{q=1}^{\tilde{r}_i} \lambda_{\tilde{j}_q}^{\tilde{\xi}_q}\right) \\ &= \left(\prod_{q \in Q_{o,1}} \lambda_0^{\nu_q} \prod_{q \in Q_{o,2}} \lambda_{i_q}^{\nu_q}\right) \left(\prod_{q=1}^{\tilde{r}_o} \chi_{\tilde{i}_q}^{\tilde{\nu}_q}\right) \left(\prod_{q=1}^{r_i} \chi_{j_q}^{\xi_q}\right) \\ & \quad \times \left(\prod_{q \in Q_{i,1}} \lambda_0^{\tilde{\xi}_q} \prod_{q \in Q_{i,2}} \lambda_{\tilde{j}_q}^{\tilde{\xi}_q}\right) \\ &= \left(\prod_{q \in Q_{o,2}} \lambda_{i_q}^{\nu_q}\right) \left(\prod_{q=1}^{\tilde{r}_o} \chi_{\tilde{i}_q}^{\tilde{\nu}_q}\right) \left(\prod_{q=1}^{r_i} \chi_{j_q}^{\xi_q}\right) \left(\prod_{q \in Q_{i,2}} \lambda_{\tilde{j}_q}^{\tilde{\xi}_q}\right). \end{aligned} \quad (64)$$

The right-hand side in Eq. (64) can be interpreted as a product of  $t'$  real or complex numbers of magnitude less than one, where

$$t' = \sum_{q \in Q_{o,2}} \nu_q + \sum_{q=1}^{\tilde{r}_o} \tilde{\nu}_q + \sum_{q=1}^{r_i} \xi_q + \sum_{q \in Q_{i,2}} \tilde{\xi}_q. \quad (65)$$

According to Eq. (63),  $t'$  can either diverge or remain finite at long times, resulting in Type III and Type II terms, respectively. Thus,  $\mathcal{Z}_{\pi,\bar{\sigma}}$  can be expressed as sum of Type I, Type II, and Type III terms in accordance with **Theorem 2**. A similar analysis indicates that **Theorem 2** is also valid for  $\mathcal{Z}_{\pi,\bar{\sigma}}^{\{n,n\}}$  and  $\mathcal{Z}_{\pi,\bar{\sigma}}^{\{n,\mathcal{T}n\}}$ .

The above analysis for all three cases of  $\mathcal{T}$ -symmetry provides further insights into the contribution of different diagrams. More specifically, red arcs whose length diverges with increasing time lead to Type III terms, whereas red arcs whose length remains finite with increasing time lead to Type II terms.

## VIII. REDUCED DIAGRAMS

Computing  $\mathcal{X}_\pi$ ,  $\mathcal{X}_\pi^{\{n,n\}}$ ,  $\mathcal{Y}_\pi$ ,  $\mathcal{Y}_\pi^{\{n,n\}}$ ,  $\mathcal{Z}_{\pi,\bar{\sigma}}$ ,  $\mathcal{Z}_{\pi,\bar{\sigma}}^{\{n,n\}}$ , and  $\mathcal{Z}_{\pi,\bar{\sigma}}^{\{n,\mathcal{T}n\}}$  for all permutations using the rules in Secs. IV, V, and VI is practically impossible. However, **Theorem 2** has shown a general pattern in each of them. More specifically, each of them can be expressed as a sum of a universal Type I term, and nonuniversal Type II and Type III terms. Since Type III terms decay exponentially with time, they don't determine the SFF beyond  $t^*$ . Therefore, the Type I and Type II terms are only significant for studying emergence of RMT behavior beyond  $t^*$ . With this motivation, we now define a reduced diagram. In the proof of **Theorem 2** in Sec. VII, **Case 2** terms are all Type III in each case of  $\mathcal{T}$ -symmetry. A reduced diagram eliminates **Case 2** terms. A precise definition of a reduced diagram is different for  $\mathcal{T}^2 = 1$ , in the absence of  $\mathcal{T}$ -symmetry, and  $\mathcal{T}^2 = -1$  cases. Thus, we present them explicitly for each case.

$\mathcal{T}^2 = 1$ : In Eq. (55), **Case 2** terms can be eliminated by fixing any one of  $i_{q'} = 0$  while allowing  $i_q \in \{0, 1, \dots, \mathcal{N} - 1\}$  when  $q \neq q'$ . This is diagrammatically equivalent to inserting a factor of  $\lambda_0^{\nu_{q'}} \mathcal{M}_{a,b}^{(0)} (= 1/\mathcal{N})$  for a red arc of length  $\nu_{q'}$  as in Fig. 7, instead of  $\sum_{i_{q'}} \lambda_{i_{q'}}^{\nu_{q'}} \mathcal{M}_{a,b}^{(i_{q'})}$  as mentioned in Sec. IV.

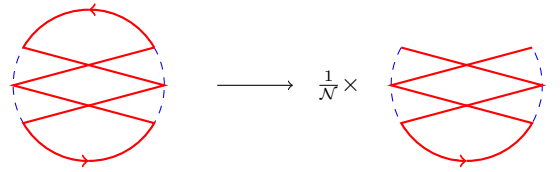


FIG. 7: A diagram and the corresponding reduced diagram obtained by inserting a factor of  $1/\mathcal{N}$  for the upper arc. The reduced diagram eliminates some of the Type III terms, which do not contribute to the SFF beyond  $t^*$ .

**Absence of  $\mathcal{T}$ -symmetry:** In Eq. (58), **Case 2** terms can be eliminated by fixing any one of  $i_{q'} = 0$  while allowing  $i_q \in \{0, 1, \dots, \mathcal{N} - 1\}$  when  $q \neq q'$ . This is diagrammatically equivalent to inserting a factor of  $\lambda_0^{\nu_{q'}} \mathcal{M}_{a,b}^{(0)} (= 1/\mathcal{N})$  for a red arc with a counterclockwise arrow and length  $\nu_{q'}$  as in Fig. 8, instead of  $\sum_{i_{q'}} \lambda_{i_{q'}}^{\nu_{q'}} \mathcal{M}_{a,b}^{(i_{q'})}$  as given in Sec. V.

$\mathcal{T}^2 = -1$ : In Eq. (62), **Case 2** terms can be eliminated by fixing any one of  $i_{q'} = 0$  while allowing

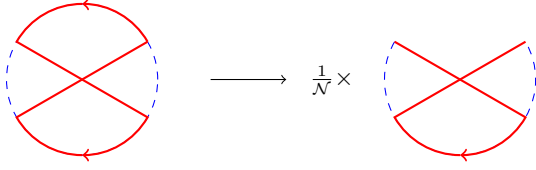


FIG. 8: A diagram and the corresponding reduced diagram obtained by inserting a factor of  $1/\mathcal{N}$  for the upper arc with a counterclockwise arrow. The lower arc has a clockwise arrow and can not be removed to get a reduced diagram.

$i_q \in \{0, 1, \dots, \mathcal{N} - 1\}$  when  $q \neq q'$  or fixing any one of  $\tilde{j}_{q'} = 0$  while allowing  $\tilde{j}_q \in \{0, 1, \dots, \mathcal{N} - 1\}$  when  $q \neq q'$ . This is diagrammatically equivalent to inserting a factor of  $\lambda_0^{\nu_{q'}} \mathcal{M}_{a,b}^{(0)} (= 1/\mathcal{N})$  for a red arc with a counterclockwise arrow and length  $\nu_{q'}$  on the outer circle or  $\lambda_0^{\tilde{\xi}_{q'}} \mathcal{M}_{a,b}^{(0)} (= 1/\mathcal{N})$  for a red arc with a clockwise arrow and length  $\tilde{\xi}_{q'}$  on the inner circle as shown in Fig. 9, instead of  $\sum_{i_{q'}} \lambda_{i_{q'}}^{\nu_{q'}} \mathcal{M}_{a,b}^{(i_{q'})}$  and  $\sum_{\tilde{j}_{q'}} \lambda_{\tilde{j}_{q'}}^{\tilde{\xi}_{q'}} \mathcal{M}_{a,b}^{(\tilde{j}_{q'})}$ , respectively, as mentioned in Sec. VI.

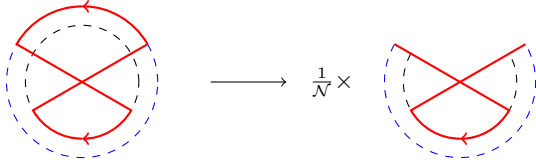


FIG. 9: A diagram and a corresponding reduced diagram obtained by inserting a factor of  $1/\mathcal{N}$  for the upper arc with counterclockwise arrow on the outer circle. The lower arc is present on the inner circle and has a clockwise arrow, therefore, unlike the  $\mathcal{T}$  absent case, Fig. 8, a reduced diagram can be obtained by removing this arc as well.

The reduced diagrams have some natural properties as follows:

**Property 1:** When  $\mathcal{T}^2 = 1$ , a diagram containing  $r$  number of red arcs has  $r$  different reduced diagrams. In the absence of  $\mathcal{T}$ -symmetry, a diagram containing  $r$  number of red arcs with counterclockwise arrows has  $r$  different reduced diagrams. When  $\mathcal{T}^2 = -1$ , a diagram containing  $r_o$  number of red arcs with counterclockwise arrows on the outer circle and  $\tilde{r}_i$  number of red arcs with clockwise arrows on the inner circle has  $r_o + \tilde{r}_i$  different reduced diagrams.

**Property 2:** If Type I term exists then each reduced diagram gives the same Type I term when evaluated using the rules in Secs. IV-VI.

**Property 3:** A reduced diagram does not give Type II terms if the size of each arc increases with time.

When  $\mathcal{T}^2 = -1$ , the basis states related by time reversal are orthogonal to each other as described in Tab. I. This property results in the following theorem for the corresponding reduced diagrams.

**Theorem 5:** For a diagram, containing a red arc with a counterclockwise arrow on the outer circle or a clockwise arrow on the inner circle such that the arc makes a jump to the other circle at one end, the reduced diagram with respect to the same arc has a vanishing contribution.

**Proof:** Fig. 10a shows a portion of an arbitrary diagram containing a red arc with a counterclockwise arrow on the outer circle. The arc follows the outer circle until state  $a$ , then instead of connecting the next state  $b$  on the same circle, it connects to the time reversed state  $\mathcal{T}b$  on the inner circle. A reduced diagram can be obtained by removing this arc and inserting a factor of  $1/\mathcal{N}$  as in Fig. 10b. Applying the rules in Sec. VI to the blue and red line segments connected to the state  $a$  and summing over  $a$  implies that the reduced diagram has a vanishing contribution.

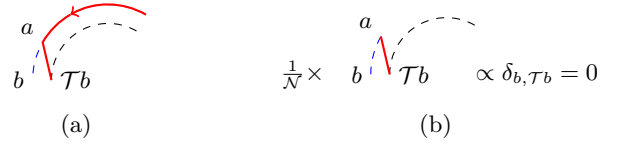


FIG. 10: (a) Portion of an allowed diagram containing a red arc with a counterclockwise arrow on the outer circle and a jump to the inner circle at one end of the arc. (b) The reduced diagram with respect to this arc has a vanishing contribution since  $b$  and  $\mathcal{T}b$  are orthogonal.

In the other case, when arc is on the inner circle, it can be pushed to the outer circle by applying **Theorem 1** as in Fig. 11. Following the arguments presented above, the reduced diagram vanishes once again.

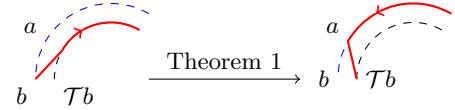


FIG. 11

## IX. EXACT CANCELLATION OF REDUCED DIAGRAMS

In Eq. (20),  $\mathcal{X}_\pi$  denotes the contribution of a diagram, where the states at different time steps are considered different even though there is an implicit repetition of states. However,  $\mathcal{X}_\pi^{\{n,n\}}$  represents the contribution of a diagram, where we explicitly consider a state appearing at two different time steps. We find that the two kinds of diagrams have identical reduced diagrams. The same is true for the other two cases of  $\mathcal{T}$ -symmetry. Since  $K_1(t)$  in Eq. (20) is a difference between the contribution of these two kinds of diagrams ( $\mathcal{X}_\pi, \mathcal{X}_\pi^{\{n,n\}}$ ), the identical reduced diagrams cancel each other. Consequently, their

Type I and Type II contributions also cancel. This is a crucial detail for finding the diagrams responsible for the universal RMT behavior. We already presented the precise statement for cancellation of reduced diagrams as **Theorem 3** and **Theorem 4** in Sec. II. In the following subsections, we present their proofs.

### A. $\mathcal{T}^2 = 1$ and absence of $\mathcal{T}$ -symmetry

**Proof of Theorem 3:** In an arbitrary diagram, e.g., in Fig. 12, a red arc starts from a state  $d$  following the blue circle up to another state  $a$ , and then connects to a state  $c$ , other than the immediate next state  $b$  on the blue circle. The rest of the red curve is irrelevant for the proof. A reduced diagram can be obtained by removing this arc and inserting a factor of  $1/\mathcal{N}$  as given in Fig. 12. We apply the rules in Sec. IV or Sec. V to the blue and red line segments, respectively, between the states  $a$  and  $b$  and the states  $a$  and  $c$ , and sum over  $a$  to find

$$\mathcal{X}_\pi(\text{reduced}) \propto V_{a,b}V_{a,c}^* = \delta_{b,c}. \quad (66)$$

Thus, the states  $b$  and  $c$  are identical in the reduced diagram in Fig. 12. It suggests that an original diagram in Fig. 13 with identical states  $b$  and  $c$ , whose contribution is denoted by  $\mathcal{X}_\pi^{\{n,\bar{n}\}}$ , also has a similar reduced diagram with respect to the same arc. This diagram in the left of Fig. 13 represents a permutation of  $t$  states, two of which are identical.

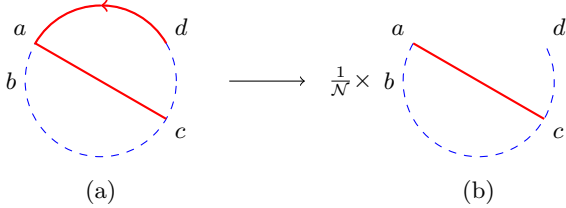


FIG. 12: A diagram with only a portion of the red path emphasizing the general structure at one end of a red arc along with a reduced diagram. A sum over the state  $a$  implies that the states  $b$  and  $c$  are identical in the reduced diagram.

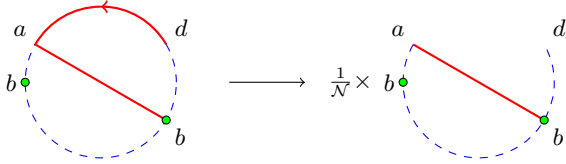


FIG. 13: A diagram with the states  $b$  and  $c$  of the diagram in Fig. 12a being identical from the beginning. This diagram also has a reduced diagram identical to that in Fig. 12b.

### B. $\mathcal{T}^2 = -1$

**Proof of Theorem 4:** In an arbitrary diagram, a red arc with a counterclockwise arrow on the outer circle starts

from a state  $d$  following the blue path up to another state  $a$ , and then connects to a state  $c$  on the outer circle as in Fig. 14a or a state  $\mathcal{T}c$  on the inner circle as in Fig. 15a, other than the immediate next state  $b$  on the outer circle. When state  $c$  is connected as in Fig. 14a, an analysis similar to the proof of **Theorem 3** implies that there exists an identical diagram with the state  $c$  same as the state  $b$  as shown in Fig. 14b. These two diagrams in Figs. 14a,14b have identical reduced diagrams. When the state  $\mathcal{T}c$  is connected in the diagram in Fig. 15a, another diagram with an identical reduced diagram has a state and its time reversed state at two different time steps on the outer circle as in Fig. 15b.

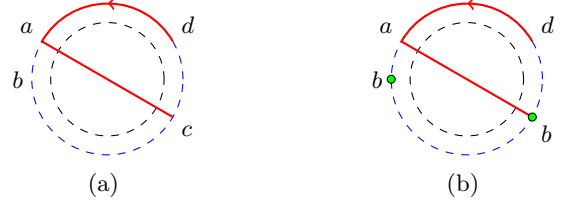


FIG. 14

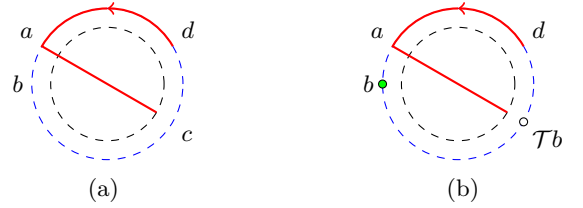


FIG. 15

## X. LEADING-ORDER SFF: LINEAR RAMP

In all three cases of  $\mathcal{T}$ -symmetry, the leading-order SFF is determined by the identity permutation and its variants.

### A. $\mathcal{T}^2 = 1$

For  $\mathcal{T}$ -invariant systems with  $\mathcal{T}^2 = 1$ , the identity permutation has  $t$  cyclic and  $t$  anticyclic variants, all of which have the same contribution due to PBC in time and the symmetric nature of the matrix  $V$ . Therefore,

$$K_1^{(1)}(t) = \sum_{l=0}^{t-1} \mathcal{X}_{C^l I} + \mathcal{X}_{\mathcal{R}C^l I} = 2t \mathcal{X}_I, \quad (67)$$

where the subscript  $I$  denotes the identity permutation, which is described diagrammatically by overlapping blue and red circles. Therefore, we find by applying the rules in Sec. IV:

$$\mathcal{X}_I = \text{tr} \mathcal{M}^t, \quad (68)$$

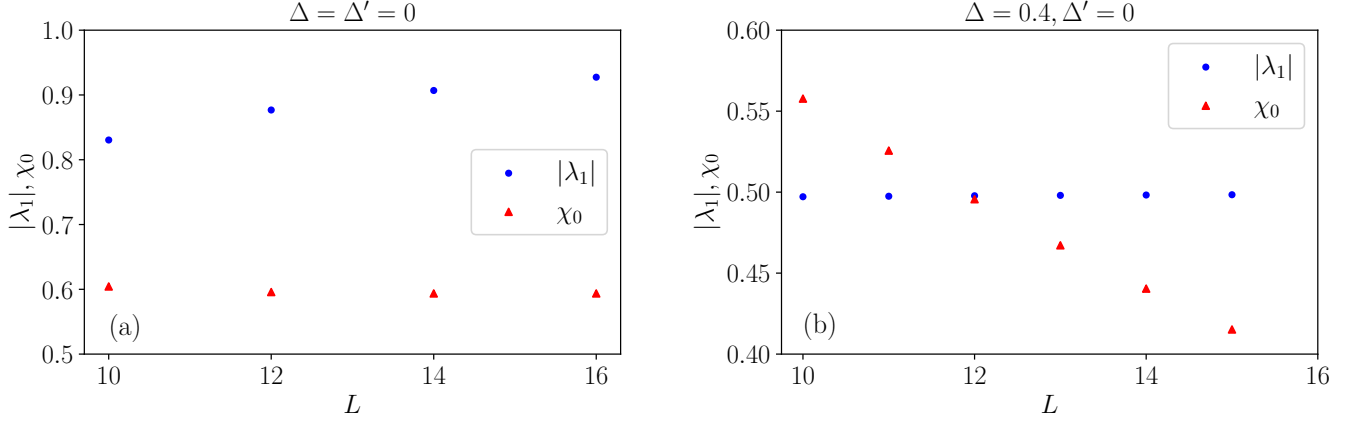


FIG. 16: Second-largest eigenvalue  $\lambda_1$  of  $\mathcal{M}$  and largest eigenvalue  $\chi_0$  of  $\tilde{\mathcal{M}}$  for different system sizes  $L$  for a kicked strongly interacting spinless fermionic chain in the absence of  $\mathcal{T}$ -symmetry, and (a) with ( $\Delta = \Delta' = 0$ ) and (b) without ( $\Delta = 0.4, \Delta' = 0$ ) particle-number conservation. We use the Hamiltonian in Eq. (35) with parameters in Eqs. (45,46). We apply PBC in real space, and take half filling for  $\Delta = \Delta' = 0$ . Here,  $J = 0.5$  and  $g = 0.25$ .

which gives the leading-order SFF:

$$K_1^{(1)}(t) = 2t \operatorname{tr} \mathcal{M}^t = 2t(1 + \lambda_1^t + \dots + \lambda_{\mathcal{N}-1}^t). \quad (69)$$

Since  $|\lambda_i| < 1$  for  $i = 1, \dots, \mathcal{N} - 1$ , we find at long times  $K_1^{(1)}(t) \simeq 2t$ , which is the COE result up to the first order in time. We notice that all the Type III terms are exponentially decaying in accordance with **Theorem 2**. The last Type III term to vanish is  $\lambda_1^t$ . This term determines  $t^*$ . We define  $t^*$  as the solution of the equation:

$$d_1 \lambda_1^{t^*} \simeq \frac{1}{e}, \quad (70)$$

where  $d_1$  is the degeneracy of eigenvalue  $\lambda_1$ . We find  $t^*$  by solving Eq. (70):

$$t^* \simeq \frac{\ln(d_1) + 1}{|\ln \lambda_1|}. \quad (71)$$

Following Roy and Prosen [26], we study a periodically kicked strongly interacting spinless fermion chain in Eqs. (34,35) with the parameters in Eqs. (43,44) to determine  $t^*$  in the presence and absence of a  $U(1)$  symmetry. When  $\Delta = 0$ , the Hamiltonians in Eqs. (34,35) commute with  $\hat{N}$  in Tab. II. Therefore, the model has  $U(1)$  symmetry for  $\Delta = 0$ . Our numerical study reveals that the matrix  $\mathcal{M}$  is  $SU(2)$  invariant, which implies the existence of  $SU(2)$  multiplets, with descendant states in different particle-number sectors. The eigenvalue  $\lambda_1$  is independent of the total number of particles. Therefore, the corresponding eigenstate is a descendant state. We can find  $\lambda_1$  numerically for very large system sizes  $L$  for one-particle sector. In thermodynamic limit of  $L \rightarrow \infty$ , we have

$$\lambda_1 \simeq 1 - \frac{c_\beta}{L^2}, \quad (72)$$

where  $c_\beta$  is a constant, which depends on hopping  $J$  (see Tab. II). Substituting Eq. (72) and  $d_1 = 2$  (as our numerical study reveals that  $\lambda_1$  is doubly degenerate) into Eq. (71), we can find  $t^*$  as [26, 30],

$$t^* \propto L^2. \quad (73)$$

We can find  $\lambda_1$  and  $d_1$  analytically by mapping the matrix  $\mathcal{M}$  to a many-body spin 1/2 Hamiltonian in the Trotter regime of small parameters  $|J|, |\Delta| \ll 1/\tau_p = 1$  [26, 30].

$$\mathcal{M} \simeq (1 - c_1 L) \mathbf{1}_{\mathcal{N}} + \sum_{x=1}^L \sum_{\nu} c_\nu s_x^\nu s_{x+1}^\nu, \quad (74)$$

where  $\nu = 1, 2, 3$ ,  $c_1 = (|J|^2 + |\Delta|^2)/2$ ,  $c_2 = c_3 = (|J|^2 - |\Delta|^2)/2$ , and  $s_x^\nu$  are the Pauli matrices at site  $x$ . In the presence of  $U(1)$  symmetry when  $\Delta = 0$ ,  $\mathcal{M}$  becomes an  $XXX$ -Heisenberg spin 1/2 chain, which gives  $\lambda_1 \simeq 1 - 2\pi^2 J^2/L^2$  for pseudo-momenta  $k = 2\pi/L, 2\pi - 2\pi/L$  in the thermodynamic limit. Consequently,  $t^* \propto L^2$ . When  $\Delta \neq 0$ ,  $U(1)$  symmetry is absent and the Eq. (74) becomes an  $XXZ$ -Heisenberg chain, which is well known to have a gapped spectrum. Therefore,  $\lambda_1 \simeq \mathcal{O}(L^0)$  and  $d_1 = 2$  due to reflection symmetry. Thus,  $t^* \propto L^0$ . The above system-size scalings of  $t^*$  following a similar analysis were studied in [26]. However, two other regimes of parameters were missed in [26]. When  $|J| = |\Delta|$ , the Eq. (74) becomes an Ising Hamiltonian, leading to  $\lambda_1 = 1 - 4J^2$  and  $d_1 = L(L+1)/2$ . Thus, we have  $t^* \propto \ln(L)$ , which matches with the system-size scalings of  $t^*$  for a local kicking model studied in Kos *et al.* [19]. Further, for  $J = 0$  but  $\Delta \neq 0$ , the Eq. (74) is equivalent to an  $XXZ$ -Heisenberg Hamiltonian with an anisotropy parameter  $-1$ . For even  $L$ , alternating site spins of such Hamiltonian can be rotated to transform  $\mathcal{M}$  back to an  $XXX$ -Heisenberg Hamiltonian, which implies  $t^* \propto L^2$ . In this case, the conserved charge is  $\hat{N}_s$  in Tab. II. Thus,

the model is still  $U(1)$  symmetric, and we expect  $t^* \propto L^2$ . The above findings suggest that the various  $L$ -scalings of  $\lambda_1$  and its degeneracy  $d_1$  lead to different  $L$ -scaling of  $t^*$ . We here provide a unified description of such scalings.

### B. Absence of $\mathcal{T}$ -symmetry

In this case, the contribution of  $t$  cyclic variants and  $t$  anticyclic variants are different due to the non-symmetric nature of the matrix  $V$ . Therefore, the leading-order SFF is

$$K_0^{(1)}(t) = \sum_{l=0}^{t-1} \mathcal{Y}_{C^l I} + \mathcal{Y}_{\mathcal{R}C^l I} = t[\mathcal{Y}_I + \mathcal{Y}_{\mathcal{R}I}]. \quad (75)$$

Applying the rules in Sec. V to the cyclic and anticyclic variants of the identity permutation, we obtain

$$\mathcal{Y}_I = \text{tr} \mathcal{M}^t, \quad (76)$$

$$\mathcal{Y}_{\mathcal{R}I} = \text{tr} \tilde{\mathcal{M}}^t. \quad (77)$$

Substituting Eqs. (76, 77) in Eq. (75), we find

$$\begin{aligned} K_0^{(1)}(t) &= t \left( \text{tr} \mathcal{M}^t + \text{tr} \tilde{\mathcal{M}}^t \right) \\ &= t \left( 1 + \lambda_1^t + \dots + \lambda_{\mathcal{N}-1}^t + \chi_0^t + \dots + \chi_{\mathcal{N}-1}^t \right). \end{aligned} \quad (78)$$

Beyond  $t^*$ , determined by  $\max(\lambda_1, \chi_0)$ , the SFF takes form  $K_0^{(1)}(t) \simeq t$ , which is the CUE prediction. We next study the Hamiltonians in Eqs. (34,35) with the parameters in Eqs. (45,46) to determine  $t^*$  for a physical model in the absence of  $\mathcal{T}$ -symmetry. Our numerical study with different parameters shows that  $\lambda_1$  of  $\mathcal{M}$  is larger than the largest eigenvalue  $\chi_0$  of  $\tilde{\mathcal{M}}$  for longer system sizes as shown in Figs. 16a, 16b. Thus,  $\lambda_1$  determines  $t^*$ . When  $\Delta = \Delta' = 0$ , the Hamiltonians in Eqs. (34,35) commute with  $\hat{N}$  in Tab. II indicating a  $U(1)$  symmetry of the model. We also numerically find that the matrix  $\mathcal{M}$  is  $SU(2)$  invariant for arbitrary  $J$  and  $g$ , which indicates the existence of descendant states. Our numerical study further reveals that  $\lambda_1$  is independent of total number of particles, and the corresponding eigenstate is a descendant state. We numerically determine  $\lambda_1$  for very long system sizes from one-particle sector. In thermodynamic limit of  $L \rightarrow \infty$ , we find

$$\lambda_1 \simeq 1 - \frac{c_\beta}{L^2}, \quad (79)$$

where  $c_\beta$  is a constant and it depends on hopping  $J$  and  $g$ . Substituting Eq. (79) and  $d_1 = 2$  (as a numerical study shows that  $\lambda_1$  is doubly degenerate) in Eq. (71), we obtain

$$t^* \propto L^2. \quad (80)$$

We can find an analytical expression for  $\lambda_1$  by mapping the matrix  $\mathcal{M}$  in the Trotter regime ( $J, g, \Delta, \Delta'$

$\ll 1/\tau_p = 1$ ), to an  $XXZ$ -Heisenberg spin 1/2 Hamiltonian with nearest-neighbor and next-nearest-neighbor couplings as

$$\mathcal{M} \simeq (1 - (c_1 + c'_1)L)\mathbb{1}_{\mathcal{N}} + \sum_{x=1}^L \sum_{\nu} c_\nu s_x^\nu s_{x+1}^\nu + c'_\nu s_x^\nu s_{x+2}^\nu, \quad (81)$$

where  $c_\nu$  are the same as in the previous sub-section and  $c'_1 = (|g|^2 + |\Delta'|^2)/2$ , and  $c'_2 = c'_3 = (|g|^2 - |\Delta'|^2)/2$ . For  $\Delta = \Delta' = 0$ , Eq. (81) becomes a  $SU(2)$  symmetric  $XXX$ -Heisenberg chain with nearest-neighbor and next-nearest-neighbor couplings, which leads to  $\lambda_1 \simeq 1 - (2\pi^2 J^2 + 8\pi^2 g^2)/L^2$  in the thermodynamic limit. It gives  $t^* \propto L^2$  [25]. When  $|\Delta| = |J|$  and  $|\Delta'| = |g|$ , Eq. (81) becomes an Ising Hamiltonian with nearest-neighbor and next-nearest-neighbor couplings, leading to  $\lambda_1 = 1 - 4|J|^2 - 4|g|^2$  and  $d_1 = L$ . Thus, we have  $t^* \propto \ln L$ , which matches with the system size scalings of  $t^*$  for a quantum circuit model in Chan *et al.* [21]. When  $|\Delta| \neq |J|$  or  $|\Delta'| \neq |g|$ , our numerical study in Fig. 16b shows that  $\lambda_1$  is a constant as  $L$  increases, and  $d_1 = 1$ , which gives  $t^* \propto L^0$ . Therefore, the system size scalings of  $t^*$  do not change for systems without  $\mathcal{T}$ -symmetry from those  $\mathcal{T}$ -invariant systems with  $\mathcal{T}^2 = 1$ . We confirm our analytical predictions of  $t^* \propto L^2$  in Figs. 17a, 17b and  $t^* \propto L^0$  in Fig. 17c by numerically computing the SFF directly using Eq. (9) without the RPA.

### C. $\mathcal{T}^2 = -1$

Following Eq. (22), the leading-order SFF can be expressed as a sum of contributions of the variants of identity permutation as follows:

$$K_{-1}^{(1)} = \sum_{\vec{\sigma}} \sum_{l=0}^{t-1} (\mathcal{Z}_{C^l I, \vec{\sigma}} + \mathcal{Z}_{\mathcal{R}C^l I, \vec{\sigma}}). \quad (82)$$

Similar to the systems without  $\mathcal{T}$ -symmetry, the matrix  $V$  is also non-symmetric for  $\mathcal{T}$ -invariant systems with  $\mathcal{T}^2 = -1$ . Further, due to PBC in time, the  $t$  cyclic variants for each  $\vec{\sigma}$  give identical contributions. Similarly, the  $t$  anticyclic variants for each  $\vec{\sigma}$  also give identical contributions but differ from the cyclic variants due to the non-symmetric nature of the matrix  $V$ . Therefore,

$$K_{-1}^{(1)} = t \sum_{\vec{\sigma}} (\mathcal{Z}_{I, \vec{\sigma}} + \mathcal{Z}_{\mathcal{R}I, \vec{\sigma}}). \quad (83)$$

To find which diagrams determine the leading-order SFF, we consider the diagram of an arbitrary variant as shown in Fig. 18. We notice that the diagram contains red arcs on the inner or outer circle connected via jumps between the two circles. **Theorem 5** implies that all the reduced diagrams of such variants have vanishing contributions. Therefore, such diagrams do not contribute to the SFF in the ergodic phase. **Theorem 5** also implies that Type I



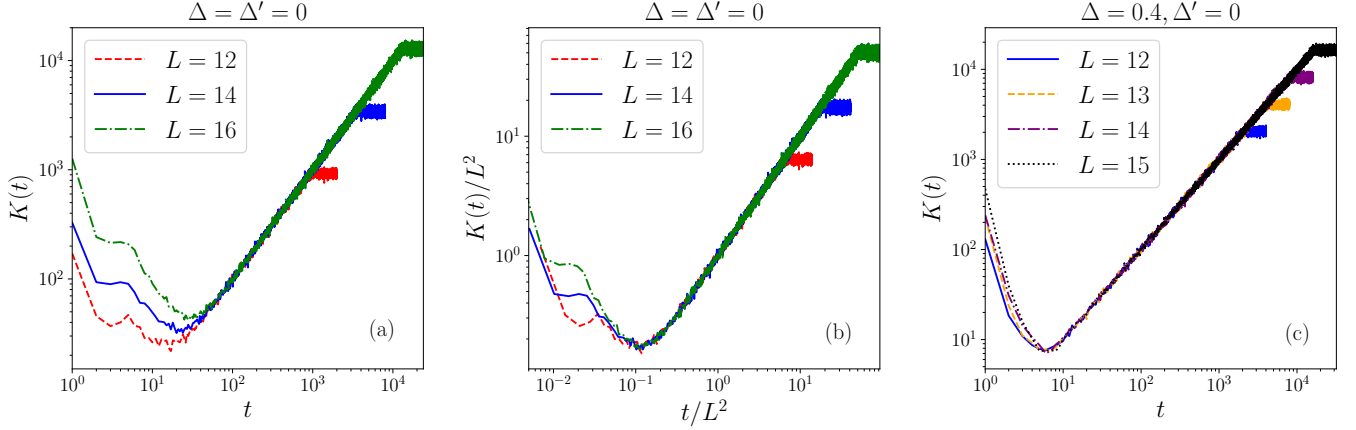


FIG. 17: Spectral form factor  $K(t)$  for different system sizes  $L$  calculated numerically using Eq. (9) for a kicked strongly interacting spinless fermionic chain in the absence of  $\mathcal{T}$ -symmetry, and (a), (b) with  $(\Delta = \Delta' = 0)$  and (c) without  $(\Delta = 0.4, \Delta' = 0)$  particle-number conservation. We use the Hamiltonians in Eqs. (34,35) with parameters in Eqs. (45,46). Here,  $\Delta\epsilon = 1, U_0 = 15, \alpha = 1.5, J = 0.5, g = 0.25$ . We apply PBC in real space, and take half filling  $N/L = 1/2$  for  $\Delta = \Delta' = 0$ . In (b), we show the data collapse in scaled time  $t/L^2$ . An averaging over 400 realizations of disorder is performed in each case.

contribution can only come from diagrams with no jump to the inner or outer circle as shown in Figs. 19a and 19b, which correspond to  $\vec{\sigma} = (0, \dots, 0)$  and  $\vec{\sigma} = (1, \dots, 1)$ , respectively. Thus, the leading-order SFF is

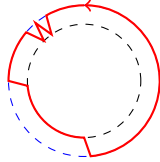
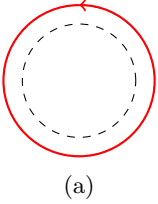
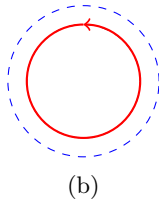


FIG. 18



(a)



(b)

FIG. 19

$$K_{-1}^{(1)}(t) = t \left[ \mathcal{Z}_{I,(0,\dots,0)} + \mathcal{Z}_{\mathcal{R}I,(0,\dots,0)} + \mathcal{Z}_{I,(1,\dots,1)} + \mathcal{Z}_{\mathcal{R}I,(1,\dots,1)} \right]. \quad (84)$$

Applying the rules in Sec. VI, we obtain

$$\mathcal{Z}_{I,(0,\dots,0)} = \mathcal{Z}_{\mathcal{R}I,(1,\dots,1)} = \text{tr} \mathcal{M}^t, \quad (85)$$

$$\mathcal{Z}_{\mathcal{R}I,(0,\dots,0)} = \mathcal{Z}_{I,(1,\dots,1)} = \text{tr} \tilde{\mathcal{M}}^t. \quad (86)$$

Substituting Eqs. (85,86) in Eq. (84), we find

$$K_{-1}^{(1)}(t) = 2t \left( \text{tr} \mathcal{M}^t + \text{tr} \tilde{\mathcal{M}}^t \right)$$

$$= 2t \left( 1 + \lambda_1^t + \dots + \lambda_{N-1}^t + \chi_0^t + \dots + \chi_{N-1}^t \right). \quad (87)$$

The SFF becomes  $K_{-1}^{(1)} \simeq 2t$  beyond  $t^*$ , which is determined by  $\max(\lambda_1, \chi_0)$ . This is the leading-order CSE result in Eq. (4). We study the Hamiltonians in Eqs. (36,37) to determine  $t^*$  in a physical system. We find numerically that  $\lambda_1 > \chi_0$  for longer  $L$  and different parameters as shown in Fig. 21. So  $\lambda_1$  determines  $t^*$  in this case also. When  $\Delta_{\sigma\sigma'} = 0$ , the Hamiltonians in Eqs. (36,37) commute with  $\hat{N}_i$  in Tab. II. Therefore, the model has  $U(1)$  symmetry. Once again, we find that the matrix  $\mathcal{M}$  is  $SU(2)$  invariant for arbitrary values of  $J_{\sigma\sigma'}$ , which indicates the existence of descendant states. Thus,  $\lambda_1$  is independent of total number of particles. We obtain numerically  $\lambda_1$  for large  $L$ 's in the one-particle sector. We find that in thermodynamic limit of  $L \rightarrow \infty$ :

$$\lambda_1 \simeq 1 - \frac{c_\beta}{L^2}, \quad (88)$$

where  $c_\beta$  is a constant, which depends on hopping  $J_{\sigma\sigma'}$ . We substitute Eq. (88) and  $d_1 = 2$  (as our numerical study reveals that  $\lambda_1$  is doubly degenerate) in Eq. (71) to find

$$t^* \propto L^2. \quad (89)$$

We can analytically determine the eigenvalues of  $\mathcal{M}$  by mapping it to a spin 1/2 Hamiltonian in the Trotter regime ( $|J_{\sigma\sigma'}|, |\Delta_{\sigma\sigma'}| \ll 1/\tau_p = 1$ ):

$$\mathcal{M} \simeq \left( 1 - L \sum_{\sigma\sigma'} c_1^{\sigma\sigma'} \right) \mathbf{1}_{\mathcal{N}} + \sum_{x=1}^L \sum_{\sigma\sigma'} \sum_{\nu} c_\nu^{\sigma\sigma'} s_{x,\sigma}^\nu s_{x+1,\sigma'}^\nu, \quad (90)$$

where  $c_1^{\sigma\sigma'} = (|J_{\sigma\sigma'}|^2 + |\Delta_{\sigma\sigma'}|^2)/2$ ,  $c_2^{\sigma\sigma'} = c_3^{\sigma\sigma'} = (|J_{\sigma\sigma'}|^2 - |\Delta_{\sigma\sigma'}|^2)/2$ ,  $\nu = 1, 2, 3$ , and  $s_{x,\sigma}^\nu$  are the Pauli

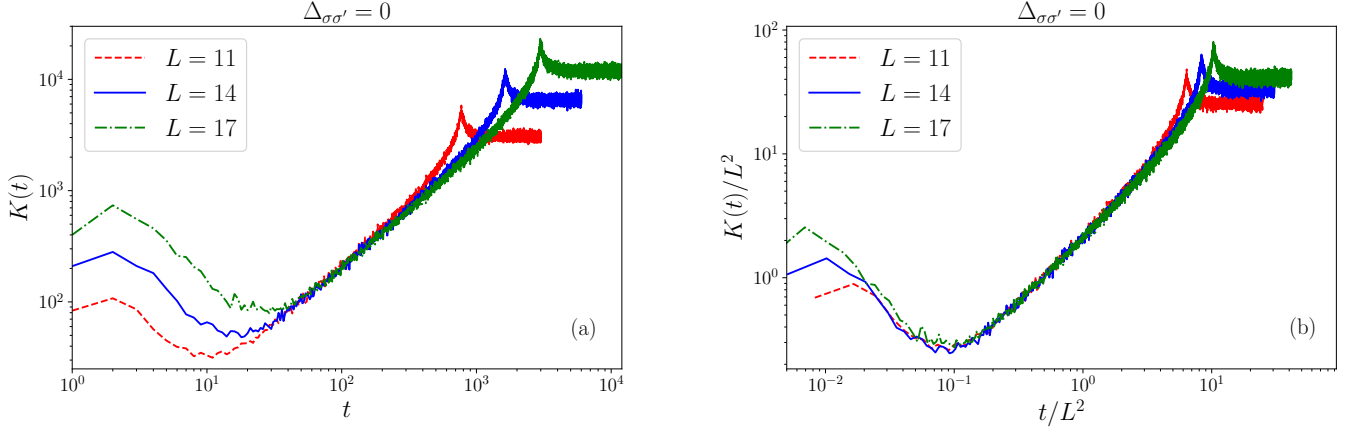


FIG. 20: Spectral form factor  $K(t)$  for different system sizes  $L$  calculated numerically using Eq. (9) for a kicked strongly interacting spinful fermionic chain in the presence of  $\mathcal{T}$ -symmetry ( $\mathcal{T}^2 = -1$ ), and particle-number conservation. We use the Hamiltonians in Eqs. (36,37). Here,  $\Delta\epsilon = 1, U_0 = 25, \Delta U_0 = 3, \alpha = 1.3, \bar{U} = 20, \Delta\bar{U} = 0.1, J_{\uparrow\uparrow} = 0.5 + 0.25i, J_{\uparrow\downarrow} = 0.5 + 0.25i$ . We apply PBC in real space, and take a fixed total number of particles ( $N_t = 3$ ). In (b), we show the data collapse in scaled time  $t/L^2$ . An averaging over 320 realizations of disorder is performed in each case.

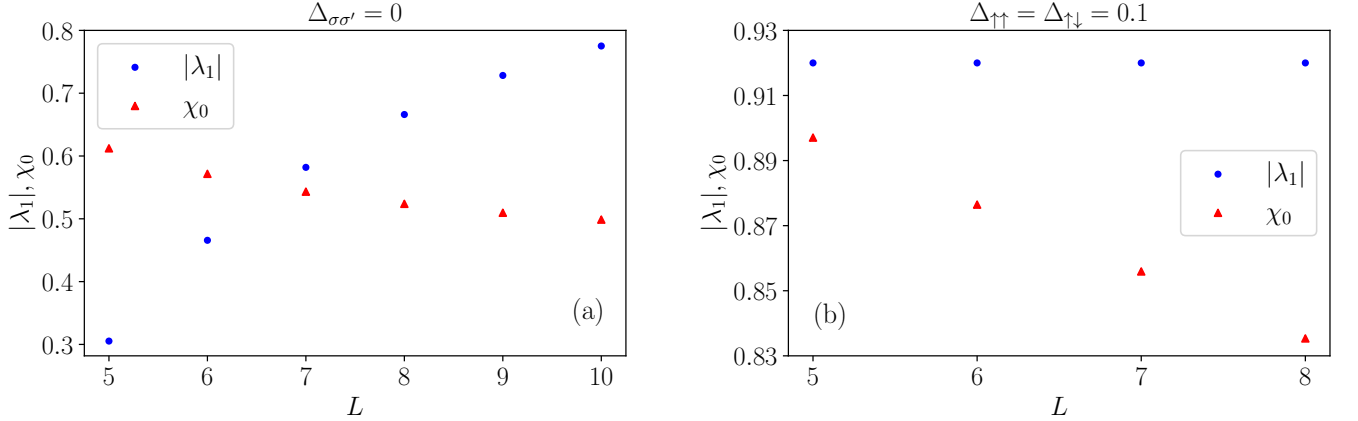


FIG. 21: Second-largest eigenvalue  $|\lambda_1|$  of  $\mathcal{M}$  and largest eigenvalue  $\chi_0$  of  $\tilde{\mathcal{M}}$  for different system sizes  $L$  for a kicked spinful  $\mathcal{T}$ -invariant fermionic chain with  $\mathcal{T}^2 = -1$ , and (a) with ( $\Delta_{\sigma\sigma'} = 0$ ) and (b) without ( $\Delta_{\uparrow\uparrow} = \Delta_{\uparrow\downarrow} = 0.1$ ) particle-number conservation. We use the Hamiltonian in Eq. (37), and apply PBC in real space. In (a), we take  $J_{\uparrow\uparrow} = 0.5 + 0.25i, J_{\uparrow\downarrow} = 0.5 + 0.25i$  and a fixed total number of particles ( $N_t = 5$ ), and in (b), we take  $J_{\uparrow\uparrow} = 0.1 + 0.1i, J_{\uparrow\downarrow} = 0.1 + 0.05i$ .

matrices at site  $x$  for each  $\sigma$ . In the presence of  $U(1)$  symmetry ( $\Delta_{\sigma\sigma'} = 0$ ),  $\mathcal{M}$  is a  $SU(2)$  invariant spin 1/2 ladder Hamiltonian. The doubly-degenerate second-largest eigenvalue calculated from the one-excitation sector reads as  $\lambda_1 \simeq 1 - 4\pi^2(|J_{\uparrow\uparrow}|^2 + |J_{\uparrow\downarrow}|^2)/L^2$  in the limit of  $L \rightarrow \infty$ . Thus,  $t^* \propto L^2$ . We confirm our analytical predictions of  $t^* \propto L^2$  in Fig. 20 for the systems of CSE class by numerically computing the SFF directly using Eq. (9) without the RPA. When  $|J_{\sigma\sigma'}| = |\Delta_{\sigma\sigma'}|$ ,  $\mathcal{M}$  becomes a spin ladder with Ising-type interaction, which gives  $\lambda_1 = 1 - 4|J_{\uparrow\uparrow}|^2 - 4|J_{\uparrow\downarrow}|^2$  with a degeneracy  $d_1 \simeq L$ . Therefore,  $t^* \propto \ln(L)$ . When  $|J_{\sigma\sigma'}| \neq |\Delta_{\sigma\sigma'}| \neq 0$ , a numerical study of the spectra of the matrix  $\mathcal{M}$  reveals that  $\lambda_1$  remains constant as  $L$  increases, as shown in Fig. (21)b, and  $d_1 = 1$ . Therefore,  $t^* \propto L^0$ . The above

$L$ -scalings of  $t^*$  for strongly interacting systems of the CSE class have not been explored earlier.

## XI. SECOND-ORDER CORRECTION

As discussed in Sec. III B, the second-order correction to the SFF is determined by the permutations, whose contributions contain Type I term of form  $1/\mathcal{N}$ . In Sec. III B, we introduce these permutations contributing to the second-order term of SFF. In the following subsections, we compute their contribution for each case of  $\mathcal{T}$ -symmetry.

A.  $\mathcal{T}^2 = 1$

Following Eq. (20), the second-order correction can be expressed in terms of the contributions of these permutations, along with their cyclic and anticyclic variants as follows:

$$K_1^{(2)} = \sum_{l=0}^{t-1} \left[ \sum_T (\mathcal{X}_{C^l T} + \mathcal{X}_{R^l T}) + \sum_S (\mathcal{X}_{C^l S} + \mathcal{X}_{R^l S}) - \sum_R (\mathcal{X}_{C^l I}^{\{n,n\}} + \mathcal{X}_{R^l I}^{\{n,n\}}) - \sum_{SR} (\mathcal{X}_{C^l S}^{\{n,n\}} + \mathcal{X}_{R^l S}^{\{n,n\}}) \right]. \quad (91)$$

Since, the cyclic and anticyclic variants give identical contribution due to PBC in time and the symmetric nature of the matrix  $V$  for systems with  $\mathcal{T}^2 = 1$ , we obtain

$$K_1^{(2)} = 2t \left[ \sum_T \mathcal{X}_T + \sum_S \mathcal{X}_S - \sum_R \mathcal{X}_I^{\{n,n\}} - \sum_{SR} \mathcal{X}_S^{\{n,n\}} \right]. \quad (92)$$

The right-hand side terms in Eq. (92) can be explicitly calculated using the rules in Sec. IV (check App. D). However, we proceed with a much insightful approach based on the reduced diagrams, since, only Type I and Type II terms can contribute to the SFF at long times. We begin by analyzing transpositions. We observe that single transpositions can be further classified into three distinct categories based on the different shapes of the diagrams representing them: (a) nearest-neighbor transposition ( $T^{(1)}$ ), where the interchanged states are adjacent on the blue circle, (b) next-nearest-neighbor transposition ( $T^{(2)}$ ), where the interchanged states are separated by two time steps on the blue circle, and (c) all other transpositions ( $T'$ ). All these transpositions are shown diagrammatically in Fig. 22. From **Theorem 3**, we find

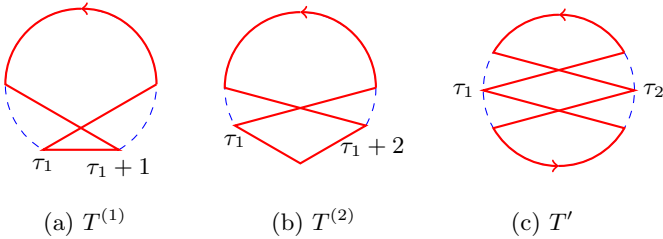


FIG. 22: Transposition ( $T$ ) diagrams of : (a) two nearest-neighbor states at time steps  $\tau_1$  and  $\tau_1 + 1$ , (b) two next-nearest-neighbor states at time steps  $\tau_1$  and  $\tau_1 + 2$ , and (c) two states at time steps  $\tau_1$  and  $\tau_2$ , where  $\tau_2 - \tau_1 > 2$ .

that the reduced diagrams of the diagrams with a state repeated twice in Figs. 23a, 23b, and 23c are identical to the reduced diagrams of the diagrams in Figs. 22a, 22b, and 22c, respectively. Since the diagrams in Figs. 23a, 23b, and 23c represent the transposition of a repeated state, they are identical to the identity permutation with a state repeated twice. Therefore, these are the  $R$  diagrams in Fig. 24. Since there are equal numbers of  $T$  and

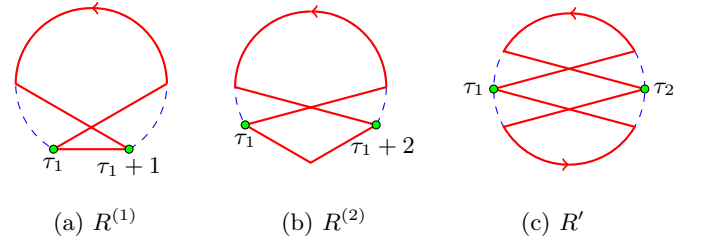


FIG. 23: Diagrams whose reduced diagrams are identical to the reduced diagrams of transpositions in Fig. 22: (a) the reduced diagram of  $R^{(1)}$  obtained by removing the upper arc cancels the reduced diagram of  $T^{(1)}$  obtained by removing the same arc, (b) the reduced diagram of  $R^{(2)}$  obtained by removing the upper arc cancels the reduced diagram of  $T^{(2)}$  obtained by removing the same arc, and (c) both the reduced diagrams of  $R'$  obtained by removing either the upper or the lower arc cancel the corresponding reduced diagrams of  $T'$ .

$R$  diagrams, as we need to choose two states from  $t$  states for both operations, and since the reduced diagrams of  $T$  and  $R$  diagrams exactly cancel, we obtain

$$\sum_T \mathcal{X}_T - \sum_R \mathcal{X}_I^{\{n,n\}} = \text{Type III terms}. \quad (93)$$

Because Type III terms decay exponentially in time, we conclude that the  $T$  and  $R$  diagrams together do not contribute to the SFF in the universal regime. Now, we con-

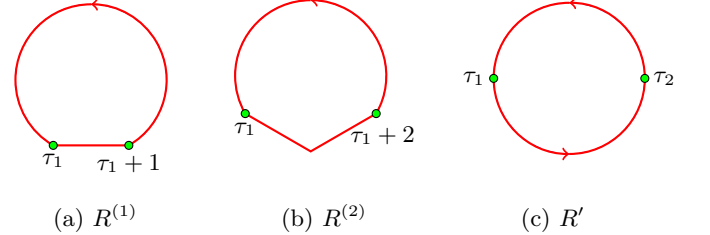


FIG. 24: Diagrams representing an identity permutation with (a) a repeated state at time steps  $\tau_1$  and  $\tau_1 + 1$ , (b) a repeated state at time steps  $\tau_1$  and  $\tau_1 + 2$ , and (c) a repeated state at time steps  $\tau_1$  and  $\tau_2$ .

sider an  $S$  diagram with the order of states reversed from  $\tau_1$  to  $\tau_2$  in Fig. 25a. When a reduced diagram is obtained by removing the upper arc, **Theorem 3** implies that an  $SR$  diagram with a repeated state at time steps  $\tau_1$  and  $\tau_2$  (see Fig. 25b) also has an identical reduced diagram after the upper arc is removed. However, when a reduced diagram is obtained by removing the lower arc of the  $S$  diagram in Fig. 25a, a different  $SR$  diagram results in an identical reduced diagram. This  $SR$  diagram, shown in Fig. 26, has identical states at time steps  $\tau_1 - 1$  and  $\tau_2 + 1$ . Unlike the  $T$  and  $R$  diagrams, the total number of  $SR$  diagrams is two more than that of  $S$  diagrams. It can be understood by noticing that the minimum value of  $\tau_2 - \tau_1$  for an  $S$  diagram is 3 to avoid overlap with nearest-neighbor and next-nearest-neighbor transpositions, and

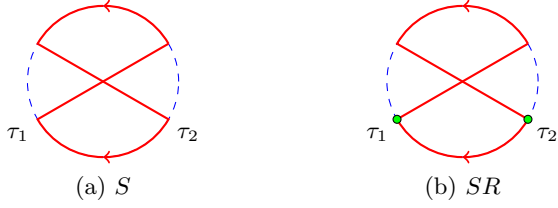


FIG. 25: Diagrams representing (a) a sub-sequence reversal ( $S$ ), and (b) a sub-sequence reversal with a state repeated twice ( $SR$ ).

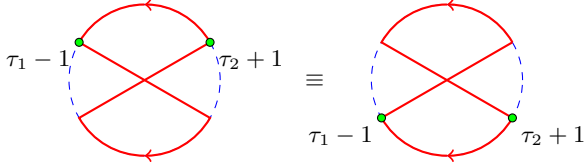


FIG. 26

its maximum value is  $t - 5$  as the minimum length of the upper arc is also 3 for the same reason. However, for an  $SR$  diagram in Fig. 25b, the minimum value of  $\tau_2 - \tau_1$  is 3 as a repeated state must be at least three time steps far for a sub-sequence reversal to give a different permutation ( $aa \rightarrow aa, aba \rightarrow aba, abca \rightarrow acba$ ) and its maximum value is  $t - 3$  as the minimum length of the upper arc can be 1. Thus, there are two extra  $SR$  diagrams compared to  $S$  diagrams. These extra  $SR$  diagrams must determine the second-order correction to the SFF in the universal regime. To calculate their contributions, we must know the lengths of the red arcs in these diagrams.

**Statement:** The lengths of both red arcs in the extra two  $SR$  diagrams diverge with increasing time.

**Proof:** Consider the  $SR$  diagram in Fig. 25b. The sum of the lengths of both red arcs is  $(t - 2)$ . Therefore, the length of at least one red arc diverges with increasing time. Now, consider the case where the lower arc in Fig. 25b has fixed length, i.e.,  $(\tau_2 - \tau_1)$  remains constant with respect to  $t$ . As mentioned at the end of Sec. VII, only red arcs of finite length determine Type II terms, while a Type I term is identical for each reduced diagram, according to **Property 1**. Therefore, it suffices to study a single reduced diagram of the  $SR$  diagram in Fig. 25b, which contains the fixed length red arc. In Fig. 25b, such a reduced diagram can be obtained by removing the upper red arc. As explained previously, there exists an  $S$  diagram, shown in Fig. 25a, with a lower red arc of length  $(\tau_2 - \tau_1)$ . The reduced diagram of this  $S$  diagram, obtained by removing the upper red arc, cancels out the corresponding reduced diagram of the  $SR$  diagram. Similarly, when length of the upper red arc,  $(t - \tau_2 + \tau_1 - 2)$ , of an  $SR$  diagram in Fig. 25b remains constant with respect to time, there exists an  $S$  diagram with the length of the upper red arc  $(t - \tau_2 + \tau_1)$ . The reduced diagrams of such  $S$  and  $SR$  diagrams, obtained by removing the lower arc, cancel each other out.

We have shown that for each  $SR$  diagram containing at least one red arc whose size remains finite with increasing time, there exists an  $S$  diagram such that they cancel the Type I and Type II terms in each other's contributions in Eq. (92). Therefore, the lengths of the red arcs in the extra two  $SR$  diagrams must diverge with increasing time.

Additionally, instead of representing a repeated state as two separate points, we can denote it by a single point by merging the points. This leads to an alternative diagrammatic representation. In this representation, the two extra  $SR$  diagrams can be drawn as in Fig. 27a. We draw the blue and red curves separately in Fig. 27b to find that these curves, respectively, resemble near-miss and self-crossing orbits of the Sieber-Richter pairs [12] of a semiclassical analysis. Applying the rules in Sec. IV to this diagram in Fig. 27a, we get

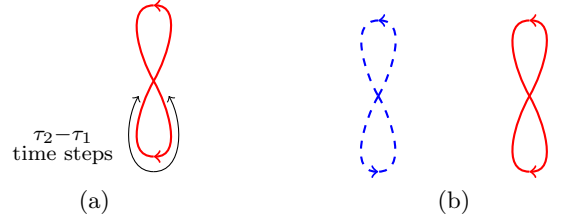


FIG. 27: (a) An  $SR$  diagram in an alternative diagrammatic representation, where the two points representing a repeated state are merged. (b) Its blue and red curves are separated to show resemblance with the Sieber-Richter pairs.

$$\begin{aligned}
 K_1^{(2)}(t) &= -\frac{2t}{2} \sum_{\tau_1=1}^t \sum_{\tau_2=\tau_1+\nu, \tau_1+\nu'} \sum_a \mathcal{M}_{a,a}^{\tau_2-\tau_1} \mathcal{M}_{a,a}^{t-\tau_2+\tau_1} \\
 &= -t^2 \sum_a \left( \mathcal{M}_{a,a}^\nu \mathcal{M}_{a,a}^{t-\nu} + \mathcal{M}_{a,a}^{\nu'} \mathcal{M}_{a,a}^{t-\nu'} \right) \\
 &= -t^2 \sum_a \sum_{ij} \left( \lambda_i^\nu \lambda_j^{t-\nu} + \lambda_i^{\nu'} \lambda_j^{t-\nu'} \right) \mathcal{M}_{a,a}^{(i)} \mathcal{M}_{a,a}^{(j)},
 \end{aligned} \tag{94}$$

where  $a$  represents a repeated state. The factor  $2t$  in the first line accounts for the  $t$  cyclic and  $t$  anticyclic variants, which contribute identically. Furthermore, the extra factor  $1/2$  is included to avoid double counting in summing over  $\tau_1, \tau_2$  since a change in the order of  $\tau_1, \tau_2$  does not lead to a new permutation when both cyclic and anticyclic variants have been considered (check App. D). As the arc sizes  $t - \nu, t - \nu', \nu,$  and  $\nu'$  diverge with time for these extra  $SR$  diagrams, we obtain at long times

$$\begin{aligned}
 K_1^{(2)}(t) &= -t^2(1+1) \sum_a \mathcal{M}_{a,a}^{(0)} \mathcal{M}_{a,a}^{(0)} + \mathcal{O}(\lambda_1^\nu) \\
 &= -\frac{2t^2}{\mathcal{N}} + \mathcal{O}(\lambda_1^\nu).
 \end{aligned} \tag{95}$$

The first term on the right side of Eq. (95) only survives for  $t > t^*$ , which is the second-order correction

for the COE class. We can further interpret this contribution as  $K_1^{(2)}(t) = -2t^2 \sum_{\underline{n}} P_t^{(2)}(\underline{n})$ , where  $P_t^{(2)}(\underline{n}) \equiv \text{tr} \mathcal{M}^\nu \text{tr} \mathcal{M}^{t-\nu}$  is the probability of returning to an initial state  $|\underline{n}\rangle$  twice in time  $t$  with the constraint that the interval  $\nu$  between two returns diverges with  $t$ . Fig. 28 shows a comparison between the SFF computed using Eq. (9) and that obtained using the RPA up to the first- and second-order universal terms along with all the Type III terms (check App. D). It shows a good match beyond  $t^*$  up to a longer time when the second-order universal term is included. The difference between the SFF computed directly and that obtained using the RPA in the nonuniversal regime of  $t < t^*$  in Fig. 28 is due to the RPA and the exclusion of all higher-order contributions beyond second order.

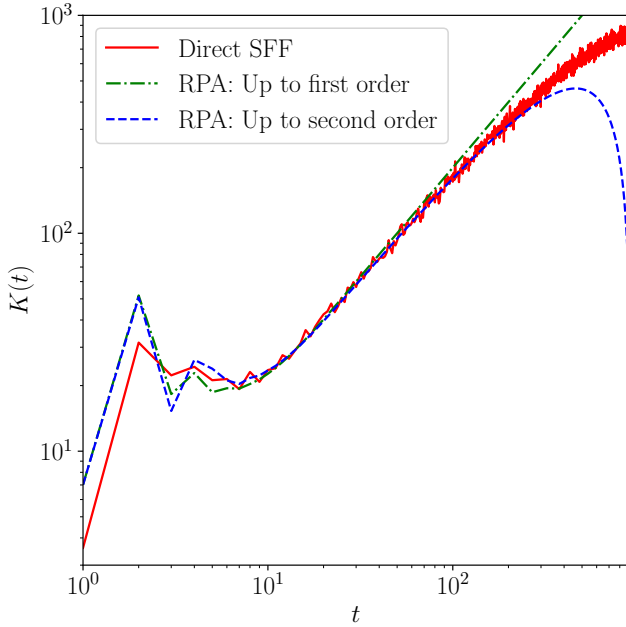


FIG. 28: A comparison of directly calculated SFF,  $K(t)$ , using Eq. (9) with that obtained using the RPA up to first and second order in time including both the universal and nonuniversal terms for a kicked spinless fermionic chain with  $\mathcal{T}^2 = 1$  and particle-number conservation. We use the Hamiltonians in Eqs. (34,35) with parameters in Eqs. (43,44). We take  $L = 12, N = 6, J = 1, \langle \epsilon \rangle = 0, \Delta \epsilon = 1, U_0 = 22, \alpha = 1.5$ . An averaging over 400 realizations of disorder is performed for the direct simulation of  $K(t)$ .

### B. Absence of $\mathcal{T}$ -symmetry

In the absence of  $\mathcal{T}$ -symmetry, matrix  $V$  is not symmetric. Therefore, the cyclic and anticyclic variants contribute differently. Consequently, the second-order correction can be expressed as follows:

$$K_0^{(2)} = t \left[ \sum_T (\mathcal{Y}_T + \mathcal{Y}_{\mathcal{RT}}) + \sum_S (\mathcal{Y}_S + \mathcal{Y}_{\mathcal{RS}}) \right].$$

$$- \sum_R (\mathcal{Y}_I^{\{\underline{n}, \underline{n}\}} + \mathcal{Y}_{\mathcal{RI}}^{\{\underline{n}, \underline{n}\}}) - \sum_{SR} (\mathcal{Y}_S^{\{\underline{n}, \underline{n}\}} + \mathcal{Y}_{\mathcal{RS}}^{\{\underline{n}, \underline{n}\}}) \Big]. \quad (96)$$

We get Type I and Type II terms from a diagram only if it has a reduced diagram, which can be figured out from Eq. (58). Thus, the anticyclic variants of  $T$  and  $R$  diagrams can only contribute Type III terms, as they contain red arcs with clockwise arrows. Therefore,

$$\sum_T \mathcal{Y}_{\mathcal{RT}} = \text{Type III terms}, \quad (97)$$

$$\sum_R \mathcal{Y}_{\mathcal{RI}}^{\{\underline{n}, \underline{n}\}} = \text{Type III terms}. \quad (98)$$

Furthermore, like the  $\mathcal{T}^2 = 1$  case, the cyclic variants of  $T$  and  $R$  diagrams cancel out their corresponding reduced diagrams. Therefore,

$$\sum_T \mathcal{Y}_T - \sum_R \mathcal{Y}_I^{\{\underline{n}, \underline{n}\}} = \text{Type III terms}. \quad (99)$$

In addition, all the reduced diagrams of the  $S$  diagrams are canceled by the reduced diagrams of the  $SR$  diagrams. Once again, there are two extra  $SR$  diagrams in which length of the red arcs diverges with increasing time. Therefore, Eq. (96) gives the following expression by ignoring the Type III terms:

$$K_0^{(2)}(t) = -t \sum_{\substack{\text{extra } SR \\ \text{diagrams}}} (\mathcal{Y}_S^{\{\underline{n}, \underline{n}\}} + \mathcal{Y}_{\mathcal{RS}}^{\{\underline{n}, \underline{n}\}}). \quad (100)$$

Since one of the red arcs has a clockwise arrow and the other has a counterclockwise arrow as in Fig. 27a, we find following the rules in Sec. V:

$$\begin{aligned} \sum_{\substack{\text{extra } SR \\ \text{diagrams}}} \mathcal{Y}_S^{\{\underline{n}, \underline{n}\}} &= \frac{1}{2} \sum_{\tau_1=1}^t \sum_{\substack{\tau_2=\tau_1+\nu, \\ \tau_1+\nu'}} \sum_a \tilde{\mathcal{M}}_{a,a}^{\tau_2-\tau_1} \mathcal{M}_{a,a}^{t-\tau_2+\tau_1} \\ &= \frac{t}{2} \sum_a (\tilde{\mathcal{M}}_{a,a}^\nu \mathcal{M}_{a,a}^{t-\nu} + \tilde{\mathcal{M}}_{a,a}^{\nu'} \mathcal{M}_{a,a}^{t-\nu'}) \\ &= \frac{t}{2} \sum_a \sum_{ij} (\chi_i^\nu \lambda_j^{t-\nu} + \chi_i^{\nu'} \lambda_j^{t-\nu'}) \tilde{\mathcal{M}}_{a,a}^{(i)} \mathcal{M}_{a,a}^{(j)}. \end{aligned} \quad (101)$$

As the arc lengths  $\nu, \nu', t-\nu, t-\nu'$  diverge with increasing time, we find that at long times:

$$\sum_{\substack{\text{extra } SR \\ \text{diagrams}}} \mathcal{Y}_S^{\{\underline{n}, \underline{n}\}} = \mathcal{O}(\lambda_1^{t-\nu}, \chi_0^\nu). \quad (102)$$

Similarly,

$$\begin{aligned} \sum_{\substack{\text{extra } SR \\ \text{diagrams}}} \mathcal{Y}_{\mathcal{RS}}^{\{\underline{n}, \underline{n}\}} &= \frac{1}{2} \sum_{\tau_1=1}^t \sum_{\substack{\tau_2=\tau_1+\nu, \\ \tau_1+\nu'}} \sum_a \mathcal{M}_{a,a}^{\tau_2-\tau_1} \tilde{\mathcal{M}}_{a,a}^{t-\tau_2+\tau_1} \\ &= \mathcal{O}(\lambda_1^\nu, \chi_0^{t-\nu}). \end{aligned} \quad (103)$$

Substituting Eqs. (102) and (103) in Eq. (100), we obtain

$$K_0^{(2)}(t) = \mathcal{O}(\lambda_1^{t-\nu}, \lambda_0^\nu). \quad (104)$$

In App. E, we show an exact calculation based on the rules in Sec. V also leads to the same result. Therefore, unlike the  $\mathcal{T}^2 = 1$  case, there is no universal term in second order in time, which is identical to the result of the CUE class.

### C. $\mathcal{T}^2 = -1$

In this case also, the matrix  $V$  is not symmetric. Thus, the second-order correction to the SFF following Eq. (22) reads as below:

$$\begin{aligned} K_{-1}^{(2)} = t \sum_{\vec{\sigma}} & \left[ \sum_T (\mathcal{Z}_{T,\vec{\sigma}} + \mathcal{Z}_{\mathcal{R}T,\vec{\sigma}}) + \sum_S (\mathcal{Z}_{S,\vec{\sigma}} + \mathcal{Z}_{\mathcal{R}S,\vec{\sigma}}) \right. \\ & - \sum_R (\mathcal{Z}_{I,\vec{\sigma}}^{\{n,n\}} + \mathcal{Z}_{\mathcal{R}I,\vec{\sigma}}^{\{n,n\}}) - \sum_{SR} (\mathcal{Z}_{S,\vec{\sigma}}^{\{n,n\}} + \mathcal{Z}_{\mathcal{R}S,\vec{\sigma}}^{\{n,n\}}) \\ & - \sum_R (\mathcal{Z}_{I,\vec{\sigma}}^{\{n,\mathcal{T}n\}} + \mathcal{Z}_{\mathcal{R}I,\vec{\sigma}}^{\{n,\mathcal{T}n\}}) \\ & \left. - \sum_{SR} (\mathcal{Z}_{S,\vec{\sigma}}^{\{n,\mathcal{T}n\}} + \mathcal{Z}_{\mathcal{R}S,\vec{\sigma}}^{\{n,\mathcal{T}n\}}) \right]. \quad (105) \end{aligned}$$

In Eq. (105), the sum over configurations  $\vec{\sigma}$  leads to  $2^t$  different variants for each permutation. We analyze the diagrams of different variants using **Theorem 1**, **Theorem 4** and **Theorem 5** to identify the diagrams responsible for the second-order correction. We start by analyzing the  $T$  and  $R$  diagrams followed by the  $S$  and  $SR$  diagrams.

#### 1. $T$ and $R$

An arbitrary variant of a transposition diagram is shown in Fig. 29. A necessary requirement for a vari-

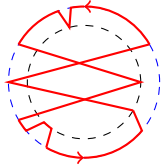


FIG. 29

ant to have Type I or Type II terms in its contribution is the existence of non-vanishing reduced diagrams. From the definition of reduced diagrams in Sec. VIII, a diagram must contain either a red arc with a counterclockwise arrow on the outer circle or a red arc with a clockwise arrow on the inner circle. We study the former case in Fig. 29, as the latter case is related to the former by **Theorem 1**. **Theorem 5** implies that the reduced diagrams of such variants give a non-vanishing contribution when at

least one of the arcs does not have a jump to the inner circle at its ends, as shown in Fig. 30a. We obtain the reduced diagram in Fig. 30b by removing the lower red arc from Fig. 30a. This reduced diagram has a vanishing contribution due to the time reversal of one of the transposed states. To ensure that the reduced diagram has a non-vanishing contribution, either both of the transposed states must be time-reversed, or neither should be time-reversed. This is diagrammatically equivalent to keeping both transposed states either on the outer circle or on the inner circle, as shown in Fig. 31. **Theorem 4** implies

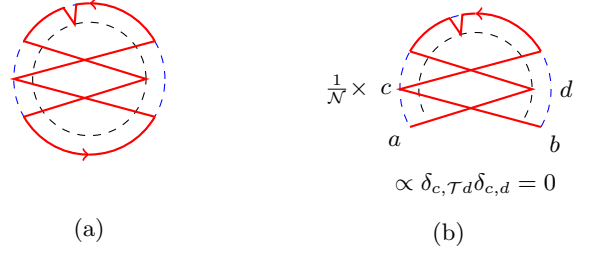


FIG. 30



FIG. 31

that the diagrams in Fig. 32 containing a state repeated twice or a state and its time-reversed state cancel the reduced diagrams of the diagrams in Fig. 31. The diagrams in Fig. 32 are equivalent to Fig. 33. We note that Fig. 33a is a variant of identity permutation with a state repeated twice, and Fig. 33b is a variant of identity permutation with a state and its time-reversed state appearing at two different time steps. We refer to Fig. 33a and Fig. 33b collectively as variants of the  $R$  diagrams. Similarly to the  $\mathcal{T}^2 = 1$  and absence of  $\mathcal{T}$ -symmetry cases, the  $T$  and  $R$  diagrams cancel the reduced diagrams of each other in Eq. (22). Therefore, the  $T$  and  $R$  diagrams together once again do not contribute to the SFF in the universal regime,

$$\begin{aligned} \sum_{\vec{\sigma}} & \left[ \sum_T (\mathcal{Z}_{T,\vec{\sigma}} + \mathcal{Z}_{\mathcal{R}T,\vec{\sigma}}) - \sum_R (\mathcal{Z}_{I,\vec{\sigma}}^{\{n,n\}} + \mathcal{Z}_{\mathcal{R}I,\vec{\sigma}}^{\{n,n\}}) \right. \\ & \left. - \sum_R (\mathcal{Z}_{I,\vec{\sigma}}^{\{n,\mathcal{T}n\}} + \mathcal{Z}_{\mathcal{R}I,\vec{\sigma}}^{\{n,\mathcal{T}n\}}) \right] = \text{Type III terms.} \quad (106) \end{aligned}$$

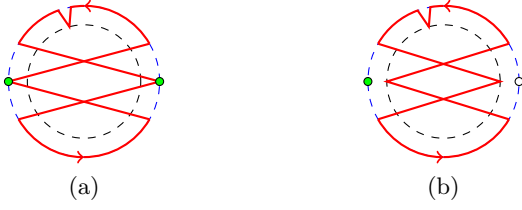


FIG. 32

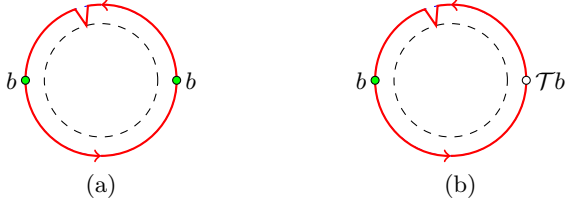


FIG. 33

## 2. $S$ and $SR$

As in the case of transposition, the variants of a  $S$  diagram containing a red arc with a counterclockwise arrow on the outer circle or a red arc with a clockwise arrow on the inner circle can contribute Type I and Type II terms. Also, both the endpoints of the reversed part should lie on the same circle as in Fig. 34. Otherwise, the reduced diagrams have vanishing contribution similar to a variant of the  $T$  diagram in Fig. 30. Applying **Theorem 4**, the

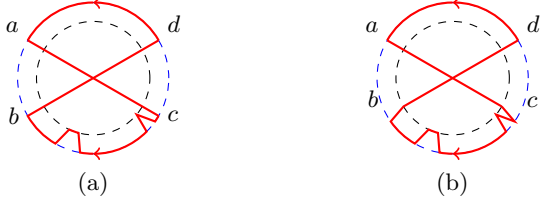


FIG. 34

reduced diagram of the  $SR$  diagram in Fig. 35a obtained by removing the upper red arc cancels out the reduced diagram of the  $S$  diagram in Fig. 34a obtained by removing the upper red arc. Furthermore, the reduced diagram of the  $SR$  diagram in Fig. 35b obtained by removing the upper red arc cancels out the reduced diagram of the

$S$  diagram in Fig. 34b obtained by removing the upper red arc. As in the cases of  $\mathcal{T}^2 = 1$  and the absence of  $\mathcal{T}$ -symmetry, there are two additional  $SR$  diagrams for each case in Fig. 35. According to Eq. (62), only diagrams containing red arcs with counterclockwise arrows on the outer circle or red arcs with clockwise arrows on the inner circle can contribute in the ergodic phase. Therefore, all red arcs with clockwise arrows in Fig. 35 must be pushed to the inner circle. Further, in Fig. 35a, the endpoints of the reversed parts must lie on the outer circle, whereas in Fig. 35b, they must lie on the inner circle. Thus, only

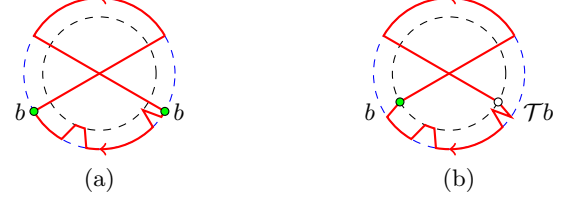


FIG. 35

the diagrams in Fig. 36 contribute to the SFF in the ergodic phase. Due to jumps at the ends of the lower arc in Fig. 36a, the reduced diagram obtained by removing the lower arc vanishes according to **Theorem 5**. According to **Property 2** in Sec. VIII, all reduced diagrams of a given diagram have identical Type I terms. Therefore, if even one reduced diagram vanishes, the original diagram does not contribute Type I term. Thus, Fig. 36a does not contribute to the SFF in the ergodic phase. We evaluate Fig. 36b by applying the rules in Sec. VI. The symbols  $\mathcal{T}c$  and  $c$  in Fig. 36b represent the states at time steps  $\tau_1$  and  $\tau_2$ . Therefore, Eq. 105 gives the below expression by ignoring the Type III terms:

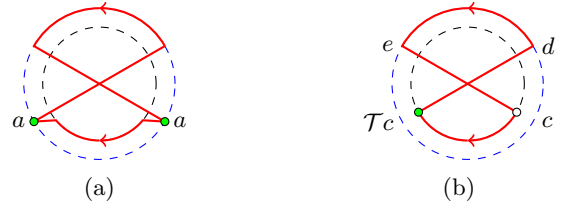


FIG. 36

$$\begin{aligned}
 K_{-1}^{(2)}(t) &= -\frac{t}{2} \sum_{\tau_1=1}^t \sum_{\substack{\tau_2=\tau_1+\nu, \\ \tau_1+\nu'}} \sum_{ij} \lambda_i^{t-\tau_2+\tau_1-2} \lambda_j^{\tau_2-\tau_1} \mathcal{M}_{d,e}^{(i)} \mathcal{M}_{\mathcal{T}c,c}^{(j)} V_{e,\mathcal{T}c} V_{c,d} V_{e,\mathcal{T}c}^* V_{-c,d}^* \\
 &= -\frac{t^2}{2} \sum_{ij} \left( \lambda_i^{t-\nu-2} \lambda_j^\nu + \lambda_i^{t-\nu'-2} \lambda_j^{\nu'} \right) \mathcal{M}_{d,e}^{(i)} \mathcal{M}_{\mathcal{T}c,c}^{(j)} V_{e,\mathcal{T}c} V_{c,d} V_{e,\mathcal{T}c}^* V_{-c,d}^*
 \end{aligned}$$

$$\begin{aligned}
&= -\frac{t^2}{\mathcal{N}^2} V_{e,\mathcal{T}c} V_{c,d} V_{e,\mathcal{T}c}^* V_{-c,d}^* - \frac{t^2}{2\mathcal{N}} \sum_{i \neq 0} \left( (\lambda_j^\nu + \lambda_j^{\nu'}) \mathcal{M}_{\mathcal{T}c,c}^{(i)} + (\lambda_i^{t-\nu-2} + \lambda_i^{t-\nu'-2}) \mathcal{M}_{d,e}^{(i)} \right) V_{e,\mathcal{T}c} V_{c,d} V_{e,\mathcal{T}c}^* V_{-c,d}^* \\
&\quad - \frac{t^2}{2} \sum_{\substack{i \neq 0, \\ j \neq 0}} \left( \lambda_i^{t-\nu-2} \lambda_j^\nu + \lambda_i^{t-\nu'-2} \lambda_j^{\nu'} \right) \mathcal{M}_{d,e}^{(i)} \mathcal{M}_{\mathcal{T}c,c}^{(j)} V_{e,\mathcal{T}c} V_{c,d} V_{e,\mathcal{T}c}^* V_{-c,d}^*. \tag{107}
\end{aligned}$$

We find by summing over matrix indices using the unitary property of the matrix  $V$ :

$$V_{e,\mathcal{T}c} V_{c,d} V_{e,\mathcal{T}c}^* V_{-c,d}^* = -\mathcal{N}. \tag{108}$$

We substitute Eq. (108) in Eq. (107) and use the fact that all the arc sizes  $\nu$ ,  $\nu'$ ,  $t - \nu - 2$ , and  $t - \nu'$  diverge with increasing time to get

$$K_{-1}^{(2)}(t) = \frac{t^2}{\mathcal{N}} + \mathcal{O}(\lambda_1^\nu). \tag{109}$$

According to **Theorem 1**, each diagram has a time-reversed counterpart that contributes identically. Thus, we must include a factor of 2, which leads to

$$K_{-1}^{(2)}(t) = \frac{2t^2}{\mathcal{N}} + \mathcal{O}(\lambda_1^\nu). \tag{110}$$

The last result is the second-order correction to the SFF for the CSE class of RMT in Eq. (4). Further, the extra SR diagrams for this case do not resemble near-miss and self-crossing orbits of the Sieber-Richter pairs of a semiclassical analysis [42]. Unlike  $\mathcal{T}^2 = 1$ , we could not give a simple probabilistic interpretation of the second-order correction in this, which probably indicates a fully quantum origin of this contribution.

## XII. HIGHER DIMENSIONS

Previous studies using RPA have explored the emergence of a universal RMT form of SFF, mainly in 1D physical models of strongly interacting fermions, bosons, qubits, and their mixtures [19, 26, 30, 37]. Nevertheless, as we mentioned in Sec. I, it would be easier to experimentally probe our many results in higher dimensions with less control. Further, higher dimensional models are abundant in nature contrary to strictly 1D models, which are more of a simplification. An example below shows that the above formalism to derive SFF analytically works in higher dimensions. Particularly, the Eqs. (20)-(22) are equally valid for higher dimensional many-body systems. We take a two-dimensional (2D) version of the  $\mathcal{T}$ -invariant system of interacting spinless fermions with  $\mathcal{T}^2 = 1$  given in Eq. (35):

$$\hat{H}_0^0 = \sum_{\vec{x}} \epsilon_{\vec{x}} \hat{n}_{\vec{x}} + \frac{1}{2} \sum_{\vec{x} \neq \vec{y}} \frac{U_0}{|\vec{x} - \vec{y}|^\alpha} \hat{n}_{\vec{x}} \hat{n}_{\vec{y}}, \tag{111}$$

$$\hat{H}_1^0 = \sum_{\langle \vec{x}, \vec{y} \rangle} -J \hat{c}_{\vec{x}}^\dagger \hat{c}_{\vec{y}} + \Delta \hat{c}_{\vec{x}}^\dagger \hat{c}_{\vec{y}}^\dagger + h.c., \tag{112}$$

where  $\vec{x} \equiv (x_1, x_2)$  is the position of a site on the 2D square lattice with  $1 \leq x_1 \leq L_1, 1 \leq x_2 \leq L_2$ , and  $\langle \vec{x}, \vec{y} \rangle$  denotes nearest-neighbor sites. We use PBC in both directions of the lattice. Here,  $J$  and  $\Delta$  represent hopping and pairing amplitude between nearest-neighbor sites in both directions. We choose them to be real for the COE class. Further,  $\alpha$  denotes the range of particle-particle interactions between different sites. We noticed that the RPA works better for 2D models than 1D ones, even for larger  $\alpha$  values (e.g.,  $\alpha > 1.5$ ). This is due to the higher number of neighbors (coordination numbers) at a fixed distance for 2D rather than 1D, which improves the approximation of independent and uniformly distributed eigenphases  $\theta_n$  made of eigenvalues of  $\hat{H}_0$ .

We can again write the leading-order SFF for 2D model by Eq. (69). The Markov matrix  $\mathcal{M}$  now can be mapped to a 2D XXZ-Heisenberg Hamiltonian in the Trotter regime of small parameters ( $|J|, |\Delta| \ll 1$ ):

$$\mathcal{M} = (1 - c_1 L_1 L_2) \mathbb{1}_{\mathcal{N}} + \sum_{\langle \vec{x}, \vec{y} \rangle} \sum_{\nu} c_{\nu} s_{\vec{x}}^{\nu} s_{\vec{y}}^{\nu} + \mathcal{O}(J^4, \Delta^4), \tag{113}$$

where  $c_1 = (|J|^2 + |\Delta|^2)/2, c_2 = c_3 = (|J|^2 - |\Delta|^2)/2$  and  $s_{\vec{x}}^{\nu}, \nu = 1, 2, 3$  are Pauli matrices at site  $\vec{x}$ . In the absence of pairing ( $\Delta = 0$ ), we have a  $SU(2)$  invariant mapped Hamiltonian in Eq. 113, whose second-largest eigenvalue  $\lambda_1$  is independent of total number of particles,  $\hat{N} = \sum_{\vec{x}} \hat{n}_{\vec{x}}$ . Thus,  $\lambda_1$  can be calculated analytically in the single particle sector. We find  $\lambda_1 \approx 1 - 2\pi^2 J^2/L^2$  in the thermodynamic limit, where  $L = \max(L_1, L_2)$ . This leads to  $t^* \propto L^2$ , which is similar to 1D case. For  $\Delta = J$ , the mapped Hamiltonian in Eq. 113 becomes a 2D Ising Hamiltonian:

$$\mathcal{M} = (1 - J^2 L_1 L_2) \mathbb{1}_{\mathcal{N}} + J^2 \sum_{\langle \vec{x}, \vec{y} \rangle} s_{\vec{x}}^1 s_{\vec{y}}^1 + \mathcal{O}(J^4, \Delta^4). \tag{114}$$

The second-largest eigenvalue of  $\mathcal{M}$  for this case is  $1 - 8J^2$  with a degeneracy of  $L_1 L_2$ . Therefore, we then have  $t^* \propto \ln(L_1 L_2)$ , indicating a logarithmic system-size dependence, which is again similar to the 1D case. While we demonstrate that our formalism works for 2D systems of the COE class, the above argument can be generalized for all three Wigner-Dyson classes in both 2D and three-dimensional systems.



### XIII. CONCLUSION

This work extends many recent efforts to analytically calculate the spectral statistics in periodically kicked interacting many-body quantum systems in chaotic regimes to all three of Dyson's circular ensembles. Our work is the first study of such systems with a CSE class. For this, we have developed an ingenious scheme to include contributions from many diagrams of different permutations of basis states. We derived SFFs up to two leading orders in time for generic periodically kicked systems supporting the RPA. We showed that leading-order SFF is determined by identity permutation similar to the diagonal approximation in semiclassical proof [11]. In contrast, the diagrams leading to second-order correction for  $\mathcal{T}$ -invariant systems with  $\mathcal{T}^2 = 1$  are identical to the Sieber-Richter pairs [13], even in pure quantum systems without classical limits. We provided general rules to calculate the contribution of different diagrams and discovered reduced diagrams that contain information on the contribution to SFF in the ergodic phase. Reduced diagrams allow more analytical control and can play a significant role in deriving the complete SFF in the ergodic phase. Our study also reveals an underlying stochastic mechanism determining the emergence of universal RMT behavior. More specifically, the general properties of the doubly stochastic matrix  $\mathcal{M}$  determine the universal RMT form of SFF in all the three cases of  $\mathcal{T}$ -symmetry ( $\mathcal{T}^2 = 1$ , absence of  $\mathcal{T}$ , and  $\mathcal{T}^2 = -1$ ). Further, we studied chains of spinless and spinful fermions to derive system-size scaling of the Thouless time using the second-largest eigenvalue of  $\mathcal{M}$ , which can be obtained numerically for large system sizes and analytically calculated in the Trotter regime due to the  $SU(2)$  symmetry of  $\mathcal{M}$  for all the three classes in the presence of  $U(1)$  symmetry. Without  $U(1)$  symmetry, numerical study reveals that the second-largest eigenvalue of  $\mathcal{M}$  is independent of system size. If the eigenvalue has degeneracy  $\mathcal{O}(L^0)$ , then  $t^*$  is also  $\mathcal{O}(L^0)$ ; whereas if the degeneracy is  $\mathcal{O}(L^\zeta)$ , then  $t^*$  is  $\mathcal{O}(\ln(L))$ . In the end, we showed that similar system-size scalings of the Thouless time can also be found in higher dimensions.

In recent years, many proposals have been made using cold atoms [36] and quantum simulators [35] to detect spectral statistics in various many-body quantum chaotic systems [43]. There have also been recent efforts to measure SFF and various correlations in different many-body quantum chaotic systems using quantum processors [44] or computers [45]. We thus hope our findings, particularly system-size scaling of  $t^*$  for the emergence of RMT SFF form with different unitary and anti-unitary symmetries (Tab. II) can be tested in coming years using these above methods. The techniques developed in this article can be applied to derive other physically relevant quanti-

ties like correlation functions and entanglement entropies in periodically kicked interacting many-body quantum systems supporting the RPA [23]. It would be interesting to check if the formalism can be extended to account for other symmetries leading to a ten-fold classification of Altland and Zirnbauer [46]. Some of the challenges in this direction in the near future are improving the RPA beyond the present form and deriving spectral statistics in autonomous systems.

### ACKNOWLEDGMENT

This research was supported in part by the International Centre for Theoretical Sciences (ICTS) for participating in the program - Stability of Quantum Matter in and out of Equilibrium at Various Scales (code:ICTS/SQMVS2024/01). TP acknowledges support by European Research Council (ERC) through Advanced grant QUEST (Grant Agreement No. 101096208), and Slovenian Research and Innovation agency (ARIS) through the Program P1-0402 and Grants N1-0219, N1-0368. We would like to thank Ajay Sharma for useful discussions.

#### Appendix A: Derivation of the rules to evaluate $\chi_\pi$ and $\chi_\pi^{\{\underline{n}, \underline{n}\}}$

We consider a permutation with the following diagram in Fig. 37.

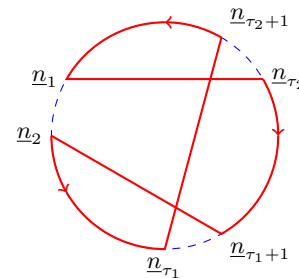


FIG. 37

The initial configuration of the states can be obtained from the blue circle by reading them in a counterclockwise direction, i.e.,  $\{\underline{n}_1, \underline{n}_2, \dots, \underline{n}_{\tau_1}, \underline{n}_{\tau_1+1}, \dots, \underline{n}_{\tau_2}, \underline{n}_{\tau_2+1}, \dots, \underline{n}_t\}$ . Similarly, the configuration of the states after a permutation can be obtained from the red curve, i.e.,  $\{\underline{n}_1, \underline{n}_{\tau_2}, \dots, \underline{n}_{\tau_1+1}, \underline{n}_2, \dots, \underline{n}_{\tau_1}, \underline{n}_{\tau_2+1}, \dots, \underline{n}_t\}$ . According to Eq. (23), the contribution to the SFF is

$$\begin{aligned}
\mathcal{X}_\pi &= \sum_{\underline{n}_1, \dots, \underline{n}_t} V_{\underline{n}_1, \underline{n}_2} \left( \prod_{\tau=2}^{\tau_1-1} V_{\underline{n}_\tau, \underline{n}_{\tau+1}} \right) V_{\underline{n}_{\tau_1}, \underline{n}_{\tau_1+1}} \left( \prod_{\tau=\tau_1+1}^{\tau_2-1} V_{\underline{n}_\tau, \underline{n}_{\tau+1}} \right) V_{\underline{n}_{\tau_2}, \underline{n}_{\tau_2+1}} \left( \prod_{\tau=\tau_2+1}^{t-1} V_{\underline{n}_\tau, \underline{n}_{\tau+1}} \right) V_{\underline{n}_t, \underline{n}_1} \\
&\times V_{\underline{n}_1, \underline{n}_{\tau_2}}^* \left( \prod_{\tau=\tau_1+1}^{\tau_2-1} V_{\underline{n}_{\tau+1}, \underline{n}_\tau}^* \right) V_{\underline{n}_{\tau_1+1}, \underline{n}_2}^* \left( \prod_{\tau=2}^{\tau_1-1} V_{\underline{n}_\tau, \underline{n}_{\tau+1}}^* \right) V_{\underline{n}_{\tau_1}, \underline{n}_{\tau_2+1}}^* \left( \prod_{\tau=\tau_2+1}^{t-1} V_{\underline{n}_\tau, \underline{n}_{\tau+1}}^* \right) V_{\underline{n}_t, \underline{n}_1}^*. \tag{A1}
\end{aligned}$$

As the matrix  $V$  is symmetric for  $\mathcal{T}$ -invariant systems when  $\mathcal{T}^2 = 1$ , and  $\mathcal{M}_{\underline{n}, \underline{n}'} = |V_{\underline{n}, \underline{n}'}|^2$ , we can rewrite the above expression as

$$\begin{aligned}
\mathcal{X}_\pi &= \sum_{\underline{n}_1, \dots, \underline{n}_t} \left( \prod_{\tau=2}^{\tau_1-1} \mathcal{M}_{\underline{n}_\tau, \underline{n}_{\tau+1}} \right) \left( \prod_{\tau=\tau_1+1}^{\tau_2-1} \mathcal{M}_{\underline{n}_\tau, \underline{n}_{\tau+1}} \right) \left( \prod_{\tau=\tau_2+1}^{t-1} \mathcal{M}_{\underline{n}_\tau, \underline{n}_{\tau+1}} \right) \mathcal{M}_{\underline{n}_t, \underline{n}_1} \\
&\times V_{\underline{n}_1, \underline{n}_2} V_{\underline{n}_{\tau_1}, \underline{n}_{\tau_1+1}} V_{\underline{n}_{\tau_2}, \underline{n}_{\tau_2+1}} V_{\underline{n}_1, \underline{n}_{\tau_2}}^* V_{\underline{n}_{\tau_1+1}, \underline{n}_2}^* V_{\underline{n}_{\tau_1}, \underline{n}_{\tau_2+1}}^* \\
&= \sum_{\substack{\underline{n}_1, \underline{n}_2 \\ \underline{n}_{\tau_1}, \underline{n}_{\tau_1+1} \\ \underline{n}_{\tau_2}, \underline{n}_{\tau_2+1}}} (\mathcal{M}^{\tau_1-2})_{\underline{n}_2, \underline{n}_{\tau_1}} (\mathcal{M}^{\tau_2-\tau_1-1})_{\underline{n}_{\tau_1+1}, \underline{n}_{\tau_2}} (\mathcal{M}^{t-\tau_2})_{\underline{n}_{\tau_2+1}, \underline{n}_1} \\
&\times V_{\underline{n}_1, \underline{n}_2} V_{\underline{n}_{\tau_1}, \underline{n}_{\tau_1+1}} V_{\underline{n}_{\tau_2}, \underline{n}_{\tau_2+1}} V_{\underline{n}_1, \underline{n}_{\tau_2}}^* V_{\underline{n}_{\tau_1+1}, \underline{n}_2}^* V_{\underline{n}_{\tau_1}, \underline{n}_{\tau_2+1}}^*. \tag{A2}
\end{aligned}$$

We insert the eigendecomposition of  $\mathcal{M}^n = \sum_i \lambda_i^n \mathcal{M}^{(i)}$ , where  $\mathcal{M}^{(i)} = |\lambda_i\rangle\langle\lambda_i|$  to find

$$\begin{aligned}
\mathcal{X}_\pi &= \sum_{\substack{\underline{n}_1, \underline{n}_2 \\ \underline{n}_{\tau_1}, \underline{n}_{\tau_1+1} \\ \underline{n}_{\tau_2}, \underline{n}_{\tau_2+1}}} \left( \sum_i \lambda_i^{\tau_1-2} \mathcal{M}_{\underline{n}_2, \underline{n}_{\tau_1}}^{(i)} \right) \left( \sum_j \lambda_j^{\tau_2-\tau_1-1} \mathcal{M}_{\underline{n}_{\tau_1+1}, \underline{n}_{\tau_2}}^{(j)} \right) \left( \sum_k \lambda_k^{t-\tau_2} \mathcal{M}_{\underline{n}_{\tau_2+1}, \underline{n}_1}^{(k)} \right) \\
&\times V_{\underline{n}_1, \underline{n}_2} V_{\underline{n}_{\tau_1}, \underline{n}_{\tau_1+1}} V_{\underline{n}_{\tau_2}, \underline{n}_{\tau_2+1}} V_{\underline{n}_1, \underline{n}_{\tau_2}}^* V_{\underline{n}_{\tau_1+1}, \underline{n}_2}^* V_{\underline{n}_{\tau_1}, \underline{n}_{\tau_2+1}}^*. \tag{A3}
\end{aligned}$$

The right-hand side of Eq. (A3) naturally leads to the rules outlined in Sec. IV.

### Appendix B: Proof that the spectral radius of $\tilde{\mathcal{M}}$ is less than one

*Geršgorin circle theorem:* Let  $M$  be a complex  $\mathcal{N} \times \mathcal{N}$  matrix, with entries  $m_{i,j}$ . For each row index  $i \in \{1, \dots, \mathcal{N}\}$ , define

$$R_i = \sum_{j \neq i} |m_{i,j}| \tag{B1}$$

as the sum of the absolute values of the non-diagonal entries in the  $i^{\text{th}}$  row. Let  $D(m_{i,i}, R_i) \subseteq \mathbb{C}$  be a closed disc centered at  $m_{i,i}$  with radius  $R_i$ . Such a disc is called a Geršgorin disc. The theorem states that every eigenvalue of  $M$  lies within at least one of the Geršgorin discs  $D(m_{i,i}, R_i)$  [47, 48].

We use this theorem to show that the eigenvalues of the  $\mathcal{N} \times \mathcal{N}$  matrix  $\tilde{\mathcal{M}}$  have magnitudes less than one. The matrix elements of  $\tilde{\mathcal{M}}$  are

$$\tilde{\mathcal{M}}_{a,b} = V_{a,b} V_{b,a}^*, \tag{B2}$$

where  $a, b = 1, \dots, \mathcal{N}$ . Since  $V$  is a unitary matrix, all the columns of  $V$  form a complete set of orthonormal basis states. The same is true for all the rows as well. However, the row states are generally different from the column states for a non-symmetric  $V$ . Next, we consider the sum of the absolute values of the elements of  $\tilde{\mathcal{M}}$  along  $a^{\text{th}}$  row:

$$\sum_b |\tilde{\mathcal{M}}_{a,b}| = \sum_b |V_{a,b}| |V_{b,a}|. \tag{B3}$$

The right-hand side of the above expression can be interpreted as the Euclidean inner product between two real non-negative vectors normalized to unity, which are

$$\begin{pmatrix} |V_{a,1}| \\ |V_{a,2}| \\ \vdots \\ |V_{a,\mathcal{N}}| \end{pmatrix}, \quad \begin{pmatrix} |V_{1,a}| \\ |V_{2,a}| \\ \vdots \\ |V_{\mathcal{N},a}| \end{pmatrix}.$$

If the two vectors are distinct for each  $a$ , their inner product is always less than 1, i.e.,

$$\sum_b |V_{a,b}| |V_{b,a}| < 1 \implies \sum_b |\tilde{\mathcal{M}}_{a,b}| < 1. \tag{B4}$$

Thus, the radius of the Geršgorin disc,  $R_a = \sum_{b \neq a} |\tilde{\mathcal{M}}_{a,b}| < 1 - |\tilde{\mathcal{M}}_{a,a}|$ . The center of the disc is  $\tilde{\mathcal{M}}_{a,a}$ , and the farthest point of  $a^{\text{th}}$  Geršgorin disc from the origin of the complex plane has a radial distance from the origin given by  $R_a + |\tilde{\mathcal{M}}_{a,a}| < 1$ . Therefore, all the eigenvalues will have magnitude less than 1. If the two vectors are identical for some  $a$ , then the largest eigenvalue can be 1. Our numerical study of the spectra of  $\tilde{\mathcal{M}}$  for Hamiltonian  $\hat{H}_1$  in Eq. (36) with arbitrary complex hopping parameters reveals that the largest eigenvalue of  $\tilde{\mathcal{M}}$  is one when  $\hat{H}_1$  has a non-conventional time reversal symmetry [40].

### Appendix C: Derivation of the rules to evaluate $\mathcal{Y}_\pi$ and $\mathcal{Y}_\pi^{\{\underline{n}, \underline{n}'\}}$

We again consider the permutation diagram in Fig. 37. According to the Eq. (25), the contribution to the SFF is

$$\begin{aligned} \mathcal{Y}_\pi = & \sum_{\underline{n}_1, \dots, \underline{n}_t} V_{\underline{n}_1, \underline{n}_2} \left( \prod_{\tau=2}^{\tau_1-1} V_{\underline{n}_\tau, \underline{n}_{\tau+1}} \right) V_{\underline{n}_{\tau_1}, \underline{n}_{\tau_1+1}} \left( \prod_{\tau=\tau_1+1}^{\tau_2-1} V_{\underline{n}_\tau, \underline{n}_{\tau+1}} \right) V_{\underline{n}_{\tau_2}, \underline{n}_{\tau_2+1}} \left( \prod_{\tau=\tau_2+1}^{t-1} V_{\underline{n}_\tau, \underline{n}_{\tau+1}} \right) V_{\underline{n}_t, \underline{n}_1} \\ & \times V_{\underline{n}_1, \underline{n}_{\tau_2}}^* \left( \prod_{\tau=\tau_1+1}^{\tau_2-1} V_{\underline{n}_{\tau+1}, \underline{n}_\tau}^* \right) V_{\underline{n}_{\tau_1+1}, \underline{n}_2}^* \left( \prod_{\tau=2}^{\tau_1-1} V_{\underline{n}_\tau, \underline{n}_{\tau+1}}^* \right) V_{\underline{n}_{\tau_1}, \underline{n}_{\tau_2+1}}^* \left( \prod_{\tau=\tau_2+1}^{t-1} V_{\underline{n}_\tau, \underline{n}_{\tau+1}}^* \right) V_{\underline{n}_t, \underline{n}_1}^*. \end{aligned} \quad (\text{C1})$$

Since the matrix  $V$  is not symmetric in the absence of  $\mathcal{T}$ -symmetry, we define  $\tilde{\mathcal{M}}_{\underline{n}, \underline{n}'} = V_{\underline{n}, \underline{n}'} V_{\underline{n}', \underline{n}}^*$  and  $\mathcal{M}_{\underline{n}, \underline{n}'} = V_{\underline{n}, \underline{n}'} V_{\underline{n}, \underline{n}'}$ . Thus, the above expression for  $\mathcal{Y}_\pi$  reduces to

$$\begin{aligned} \mathcal{Y}_\pi = & \sum_{\underline{n}_1, \dots, \underline{n}_t} \left( \prod_{\tau=2}^{\tau_1-1} \mathcal{M}_{\underline{n}_\tau, \underline{n}_{\tau+1}} \right) \left( \prod_{\tau=\tau_1+1}^{\tau_2-1} \tilde{\mathcal{M}}_{\underline{n}_\tau, \underline{n}_{\tau+1}} \right) \left( \prod_{\tau=\tau_2+1}^{t-1} \mathcal{M}_{\underline{n}_\tau, \underline{n}_{\tau+1}} \right) \mathcal{M}_{\underline{n}_t, \underline{n}_1} \\ & \times V_{\underline{n}_1, \underline{n}_2} V_{\underline{n}_{\tau_1}, \underline{n}_{\tau_1+1}} V_{\underline{n}_{\tau_2}, \underline{n}_{\tau_2+1}} V_{\underline{n}_1, \underline{n}_{\tau_2}}^* V_{\underline{n}_{\tau_1+1}, \underline{n}_2}^* V_{\underline{n}_{\tau_1}, \underline{n}_{\tau_2+1}}^* \\ = & \sum_{\substack{\underline{n}_1, \underline{n}_2 \\ \underline{n}_{\tau_1}, \underline{n}_{\tau_1+1} \\ \underline{n}_{\tau_2}, \underline{n}_{\tau_2+1}}} (\mathcal{M}^{\tau_1-2})_{\underline{n}_2, \underline{n}_{\tau_1}} (\tilde{\mathcal{M}}^{\tau_2-\tau_1-1})_{\underline{n}_{\tau_1+1}, \underline{n}_{\tau_2}} (\mathcal{M}^{t-\tau_2})_{\underline{n}_{\tau_2+1}, \underline{n}_1} \\ & \times V_{\underline{n}_1, \underline{n}_2} V_{\underline{n}_{\tau_1}, \underline{n}_{\tau_1+1}} V_{\underline{n}_{\tau_2}, \underline{n}_{\tau_2+1}} V_{\underline{n}_1, \underline{n}_{\tau_2}}^* V_{\underline{n}_{\tau_1+1}, \underline{n}_2}^* V_{\underline{n}_{\tau_1}, \underline{n}_{\tau_2+1}}^* \\ = & \sum_{\substack{\underline{n}_1, \underline{n}_2 \\ \underline{n}_{\tau_1}, \underline{n}_{\tau_1+1} \\ \underline{n}_{\tau_2}, \underline{n}_{\tau_2+1}}} \left( \sum_i \lambda_i^{\tau_1-2} \mathcal{M}_{\underline{n}_2, \underline{n}_{\tau_1}}^{(i)} \right) \left( \sum_j \chi_j^{\tau_2-\tau_1-1} \tilde{\mathcal{M}}_{\underline{n}_{\tau_1+1}, \underline{n}_{\tau_2}}^{(j)} \right) \left( \sum_k \lambda_k^{t-\tau_2} \mathcal{M}_{\underline{n}_{\tau_2+1}, \underline{n}_1}^{(k)} \right) \\ & \times V_{\underline{n}_1, \underline{n}_2} V_{\underline{n}_{\tau_1}, \underline{n}_{\tau_1+1}} V_{\underline{n}_{\tau_2}, \underline{n}_{\tau_2+1}} V_{\underline{n}_1, \underline{n}_{\tau_2}}^* V_{\underline{n}_{\tau_1+1}, \underline{n}_2}^* V_{\underline{n}_{\tau_1}, \underline{n}_{\tau_2+1}}^*, \end{aligned} \quad (\text{C2})$$

where we use the eigendecomposition of  $\mathcal{M}^n = \sum_i \lambda_i^n \mathcal{M}^{(i)}$  and  $\tilde{\mathcal{M}}^n = \sum_i \chi_i^n \tilde{\mathcal{M}}^{(i)}$  in the last line, and  $\mathcal{M}^{(i)} = {}_R |\lambda_i\rangle \langle \lambda_i|_L$  and  $\tilde{\mathcal{M}}^{(i)} = |\chi_i\rangle \langle \chi_i|$ . The right-hand side in Eq. (C2) naturally leads to the rules in Sec. V.

### Appendix D: Derivation of the second-order correction for $\mathcal{T}^2 = 1$ using only the rules in Sec. IV

#### a. Transposition ( $T$ )

A single transposition leads to three kinds of diagrams: (a) a transposition between nearest-neighbor states ( $T^{(1)}$ ), (b) a transposition between next-nearest-neighbor states ( $T^{(2)}$ ), and (c) a transposition of all other pairs of states ( $T'$ ).

Following the rules in Sec. IV, we can find the contribution of the transpositions as

$$\begin{aligned} \mathcal{X}_{T'} = & \left( \sum_i \lambda_i^{\tau_2-\tau_1-2} \mathcal{M}_{c,d}^{(i)} \right) \left( \sum_j \lambda_j^{t-\tau_2+\tau_1-2} \mathcal{M}_{f,a}^{(j)} \right) \\ & \times V_{a,b} V_{b,c} V_{d,e} V_{e,f} V_{a,e}^* V_{e,c}^* V_{d,b}^* V_{b,f}^*, \end{aligned} \quad (\text{D1})$$

$$\mathcal{X}_{T^{(1)}} = \left( \sum_i \lambda_i^{t-3} \mathcal{M}_{d,a}^{(i)} \right) V_{a,b} \mathcal{M}_{b,c} V_{c,d} V_{a,c}^* V_{b,d}^*, \quad (\text{D2})$$

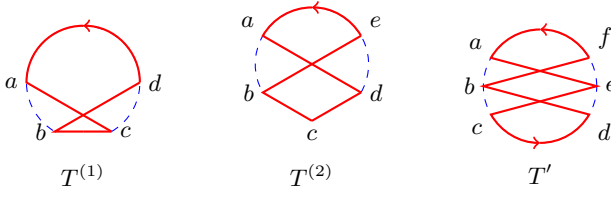


FIG. 38: The state  $b$  at time  $\tau_1$  and the state  $c$  at time  $\tau_1 + 1$  are interchanged in transposition  $T^{(1)}$ . The state  $b$  at time  $\tau_1$  and the state  $d$  at time  $\tau_1 + 2$  are interchanged in transposition  $T^{(2)}$ . The state  $b$  at time  $\tau_1$  and the state  $e$  at time  $\tau_2$  are interchanged in transposition  $T'$ .

$$\mathcal{X}_{T^{(2)}} = \left( \sum_i \lambda_i^{t-4} \mathcal{M}_{e,a}^{(i)} \right) V_{a,b} (\mathcal{M}^2)_{b,d} V_{d,e} V_{a,d}^* V_{b,e}^*. \quad (\text{D3})$$

We separately calculate the contribution of different single transpositions and their cyclic and anticyclic variants by summing over allowed values of  $\tau_1, \tau_2$  and multiplying by a factor of  $2t$ , respectively. For each case of transposition  $1 \leq \tau_1 \leq t$ . Since, each arc has minimum size 1 and we have PBC in time,  $\tau_1 + 3 \leq \tau_2 \leq t + \tau_1 - 3$  for  $T'$ . Therefore,

$$\bar{\mathcal{X}}_{T'} = (2t) \frac{1}{2} \sum_{\tau_1=1}^t \sum_{\tau_2=\tau_1+3}^{t+\tau_1-3} \sum_{ij} \lambda_i^{\tau_2-\tau_1-2} \lambda_j^{t-\tau_2+\tau_1-2} Q_{T'}^{ij}, \quad (\text{D4})$$

$$\bar{\mathcal{X}}_{T^{(1)}} = (2t) \sum_{\tau_1=1}^t \sum_i \lambda_i^{t-3} Q_{T^{(1)}}^i, \quad (\text{D5})$$

$$\bar{\mathcal{X}}_{T^{(2)}} = (2t) \sum_{\tau_1=1}^t \sum_i \lambda_i^{t-4} Q_{T^{(2)}}^i, \quad (\text{D6})$$

where

$$Q_{T'}^{ij} = \mathcal{M}_{c,d}^{(i)} \mathcal{M}_{d,a}^{(j)} \times V_{a,b} V_{b,c} V_{d,e} V_{e,f} V_{a,e}^* V_{e,c}^* V_{d,b}^* V_{b,f}^*, \quad (\text{D7})$$

$$Q_{T^{(1)}}^i = \mathcal{M}_{d,a}^{(i)} V_{a,b} \mathcal{M}_{b,c} V_{c,d} V_{a,c}^* V_{b,d}^*, \quad (\text{D8})$$

$$Q_{T^{(2)}}^i = \mathcal{M}_{e,a}^{(i)} V_{a,b} (\mathcal{M}^2)_{b,d} V_{d,e} V_{a,d}^* V_{b,e}^*, \quad (\text{D9})$$

and a factor of  $1/2$  is inserted in (D4) to avoid double counting as changing the order of  $\tau_1, \tau_2$  does not lead to a new transposition. We need the following relations for our next step

$$\mathcal{M}_{a,b}^{(0)} = \frac{1}{\mathcal{N}}, \quad (\text{D10})$$

$$\mathcal{M}^{(i)} \mathcal{M}^{(j)} = \mathcal{M}^{(i)} \delta_{ij}, \quad (\text{D11})$$

$$\text{tr} \mathcal{M}^{(i)} = 1. \quad (\text{D12})$$

Applying these relations along with the unitary property of the matrix  $V$ , we obtain

$$Q_{T'}^{00} = \frac{1}{\mathcal{N}}, \quad (\text{D13})$$

$$Q_{T'}^{i0} = Q_{T'}^{0i} = \frac{\lambda_i^2}{\mathcal{N}}, \quad i = 1, 2, \dots, \mathcal{N} - 1 \quad (\text{D14})$$

$$Q_{T^{(1)}}^{(0)} = \frac{1}{\mathcal{N}} \sum_i \lambda_i, \quad (\text{D15})$$

$$Q_{T^{(2)}}^{(0)} = \frac{1}{\mathcal{N}} \sum_i \lambda_i^2. \quad (\text{D16})$$

We next substitute Eqs. (D13),(D14) in Eq. (D4), Eq. (D15) in Eq. (D5), and Eq. (D16) in Eq. (D6) to find

$$\begin{aligned} \bar{\mathcal{X}}_{T'} &= \frac{t^2(t-5)}{\mathcal{N}} + \sum_{i \neq 0} \frac{2t^2(\lambda_i^3 - \lambda_i^{t-2})}{\mathcal{N}(1-\lambda_i)} \\ &+ t^2 \sum_{\substack{i \neq 0 \\ j \neq 0}} \frac{\lambda_i^{t-4} \lambda_j - \lambda_i \lambda_j^{t-4}}{\lambda_i - \lambda_j} Q_{T'}^{ij}, \end{aligned} \quad (\text{D17})$$

$$\bar{\mathcal{X}}_{T^{(1)}} = \frac{2t^2}{\mathcal{N}} + \frac{2t^2}{\mathcal{N}} \sum_{i \neq 0} \lambda_i + 2t^2 \sum_{i \neq 0} \lambda_i^{t-3} Q_{T^{(1)}}^i, \quad (\text{D18})$$

$$\bar{\mathcal{X}}_{T^{(2)}} = \frac{2t^2}{\mathcal{N}} + \frac{2t^2}{\mathcal{N}} \sum_{i \neq 0} \lambda_i^2 + 2t^2 \sum_{i \neq 0} \lambda_i^{t-4} Q_{T^{(2)}}^i. \quad (\text{D19})$$

We find the total contribution of all the single transpositions ( $T$ ) by adding the contributions in Eqs. (D17), (D18), and (D19):

$$\begin{aligned} \bar{\mathcal{X}}_T &= \frac{t^2(t-1)}{\mathcal{N}} + \frac{2t^2}{\mathcal{N}} \sum_{i \neq 0} \frac{\lambda_i}{1-\lambda_i} \\ &+ t^2 \sum_{i \neq 0} \left( -\frac{2\lambda_i^{t-2}}{\mathcal{N}(1-\lambda_i)} + 2\lambda_i^{t-3} Q_{T^{(1)}}^i + 2\lambda_i^{t-4} Q_{T^{(2)}}^i \right) \\ &+ t^2 \sum_{\substack{i \neq 0 \\ j \neq 0}} \frac{\lambda_i^{t-4} \lambda_j - \lambda_i \lambda_j^{t-4}}{\lambda_i - \lambda_j} Q_{T'}^{ij}. \end{aligned} \quad (\text{D20})$$

### b. Sub-sequence reversal ( $S$ )

A sub-sequence reversal permutation reverses the order of some consecutive states. Let us Consider a configuration of states on the blue circle for  $t = 9$  as  $\{\underline{n}_1, \underline{n}_2, \underline{n}_3, \underline{n}_4, \underline{n}_5, \underline{n}_6, \underline{n}_7, \underline{n}_8, \underline{n}_9\}$ . The configuration  $\{\underline{n}_1, \underline{n}_2, \underline{n}_6, \underline{n}_5, \underline{n}_4, \underline{n}_3, \underline{n}_7, \underline{n}_8, \underline{n}_9\}$  can be obtained by performing a sub-sequence reversal from time steps 3 to 6. A sub-sequence reversal is shown diagrammatically in Fig. 39. We apply the rules in Sec. IV to find

$$\mathcal{X}_S = \sum_{ij} \lambda_i^{\tau_2-\tau_1} \lambda_j^{t-\tau_2+\tau_1-2} Q_S^{ij}, \quad (\text{D21})$$

where

$$Q_S^{ij} = \mathcal{M}_{b,c}^{(i)} \mathcal{M}_{d,a}^{(j)} V_{a,b} V_{c,d} V_{a,c}^* V_{b,d}^* \quad (\text{D22})$$

To determine the contribution of all the  $S$  diagrams, we sum over all the allowed values of  $\tau_1$  and  $\tau_2$ . Naturally,  $1 \leq \tau_1 \leq t$ , however, we observe that the  $S$

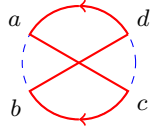


FIG. 39: A diagram representing sub-sequence reversal, where the order of states from time step  $\tau_1$  to  $\tau_2$  is reversed and the states at time steps  $\tau_1$  and  $\tau_2$  are denoted by  $b$  and  $c$ , respectively.

diagrams resemble those of nearest-neighbor and next-nearest-neighbor transpositions. Therefore, the allowed values of  $\tau_2$  should be such that the  $S$  diagrams do not overlap with nearest-neighbor and next-nearest-neighbor transposition diagrams. This leads to  $\tau_1 + 3 \leq \tau_2 \leq t + \tau_1 - 5$ . Additionally, we observe that changing the order of  $\tau_1, \tau_2$  leads to a different sub-sequence reversal shown in Fig. 40b. However, the new sub-sequence reversal is just an anticyclic variant, shown in Fig. 40d, of a sub-sequence reversal from  $\tau_1 + 1$  to  $\tau_2 - 1$  in Fig. 40c. Since we sum over all allowed values of  $\tau_1, \tau_2$  and explicitly include contribution of cyclic and anticyclic variants by including a factor of  $2t$ , we must include a factor of  $1/2$  while summing the contribution of all the  $S$  diagrams:

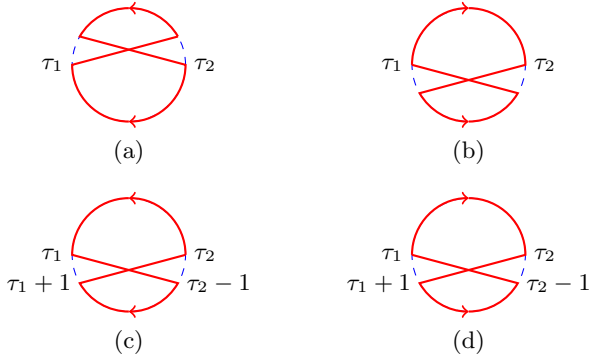


FIG. 40

$$\begin{aligned}
\bar{\mathcal{X}}_S &= (2t) \frac{1}{2} \sum_{\tau_1=1}^t \sum_{\tau_2=\tau_1+3}^{t+\tau_1-5} \mathcal{X}_S \\
&= t^2 \sum_{ij} \frac{\lambda_i^{t-4} \lambda_j^3 - \lambda_i^3 \lambda_j^{t-4}}{\lambda_i - \lambda_j} Q_S^{ij} \\
&= \frac{t^2(t-7)}{\mathcal{N}} + 2t^2 \sum_{i \neq 0} \frac{\lambda_i^3}{\mathcal{N}(1-\lambda_i)} \\
&\quad - 2t^2 \sum_{i \neq 0} \frac{\lambda_i^{t-3}}{\mathcal{N}(1-\lambda_i)} + t^2 \sum_{\substack{i \neq 0 \\ j \neq 0}} \frac{\lambda_i^{t-4} \lambda_j^3 - \lambda_i^3 \lambda_j^{t-4}}{\lambda_i - \lambda_j} Q_S^{ij},
\end{aligned} \tag{D23}$$

where we have used  $Q_S^{00} = 1/\mathcal{N}$ ,  $Q_S^{i0} = Q_S^{0i} = 1/\mathcal{N}$ .

c. Identity permutation with repetition ( $R$ )

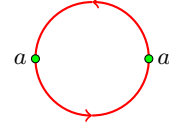


FIG. 41: A diagram representing identity permutation with repetition, where the states at time step  $\tau_1$  and  $\tau_2$  are the same and referred to as  $a$ .

The contribution of the  $R$  diagram in Fig. 41 can be found using the rules in Sec. IV. It is

$$\begin{aligned}
\mathcal{X}_I^{\{n, n\}} &= \left( \sum_i \lambda_i^{\tau_2 - \tau_1} \mathcal{M}_{a,a}^{(i)} \right) \left( \sum_j \lambda_j^{\tau_2 - \tau_1} \mathcal{M}_{a,a}^{(j)} \right) \\
&= \sum_{ij} \lambda_i^{\tau_2 - \tau_1} \lambda_j^{t - \tau_2 + \tau_1} Q_R^{ij},
\end{aligned} \tag{D24}$$

where

$$Q_R^{ij} = \mathcal{M}_{a,a}^{(i)} \mathcal{M}_{a,a}^{(j)}. \tag{D25}$$

For this case, all possible combinations of  $\tau_1, \tau_2$  are allowed. Thus,  $1 \leq \tau_1 \leq t$  and  $\tau_1 + 1 \leq \tau_2 \leq t + \tau_1 - 1$ . We also include a factor of  $1/2$  to avoid double counting of pairs of  $\tau_1, \tau_2$ :

$$\begin{aligned}
\bar{\mathcal{X}}_I^{\{n, n\}} &= (2t) \frac{1}{2} \sum_{\tau_1=1}^t \sum_{\tau_2=\tau_1+1}^{t+\tau_1-1} \sum_{ij} \lambda_i^{\tau_2 - \tau_1} \lambda_j^{t - \tau_2 + \tau_1} Q_R^{ij} \\
&= t^2 \sum_{ij} \frac{\lambda_i^t \lambda_j - \lambda_i \lambda_j^t}{\lambda_i - \lambda_j} Q_R^{ij}.
\end{aligned} \tag{D26}$$

We have  $Q_R^{00} = 1/\mathcal{N}$  and  $Q_R^{0i} = Q_R^{i0} = 1/\mathcal{N}$  for  $i = 1, \dots, \mathcal{N} - 1$ . Thus,

$$\begin{aligned}
\bar{\mathcal{X}}_I^{\{n, n\}} &= \frac{t^2(t-1)}{\mathcal{N}} + 2t^2 \sum_{i \neq 0} \frac{\lambda_i}{\mathcal{N}(1-\lambda_i)} \\
&\quad - 2t^2 \sum_{i \neq 0} \frac{\lambda_i^t}{\mathcal{N}(1-\lambda_i)} + t^2 \sum_{\substack{i \neq 0 \\ j \neq 0}} \frac{\lambda_i^t \lambda_j - \lambda_i \lambda_j^t}{\lambda_i - \lambda_j} Q_R^{ij}.
\end{aligned} \tag{D27}$$

d. Sub-sequence reversal with repetition ( $SR$ )

The contribution of the  $SR$  diagram in Fig. 42 can be calculated using the rules in Sec. IV. We obtain

$$\mathcal{X}_S^{\{n, n\}} = \sum_{ij} \lambda_i^{\tau_2 - \tau_1 - 2} \lambda_j^{t - \tau_2 + \tau_1} Q_{SR}^{ij}, \tag{D28}$$

where

$$Q_{SR}^{ij} = \sum_{a,b,c} \mathcal{M}_{c,b}^{(i)} \mathcal{M}_{a,a}^{(j)} V_{a,b} V_{c,a} V_{a,c}^* V_{b,a}^*. \tag{D29}$$

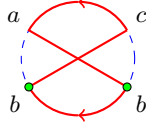


FIG. 42: A diagram representing sub-sequence reversal with repetition, where the order of states from time step  $\tau_1$  to  $\tau_2$  is reversed and the states at time steps  $\tau_1$  and  $\tau_2$  are the same and denoted by  $b$ .

The allowed values of  $\tau_1$  and  $\tau_2$  are  $1 \leq \tau_1 \leq t, \tau_1 + 3 \leq \tau_2 \leq t + \tau_1 - 3$ . Therefore, the total contribution is

$$\begin{aligned} \bar{\mathcal{X}}_S^{\{n,n\}} &= (2t) \frac{1}{2} \sum_{\tau_1=1}^t \sum_{\tau_2=\tau_1+3}^{t+\tau_1-3} \sum_{ij} \lambda_i^{\tau_2-\tau_1-2} \lambda_j^{t-\tau_2+\tau_1} Q_{SR}^{ij} \\ &= t^2 \sum_{ij} \frac{\lambda_i^{t-4} \lambda_j^3 - \lambda_i \lambda_j^{t-2}}{\lambda_i - \lambda_j} Q_{SR}^{ij}. \end{aligned} \quad (\text{D30})$$

Using  $Q_{SR}^{00} = 1/\mathcal{N}, Q_{SR}^{0i} = Q_{SR}^{i0} = 1/\mathcal{N}$ , we find,

$$\begin{aligned} \bar{\mathcal{X}}_S^{\{n,n\}} &= \frac{t^2(t-5)}{\mathcal{N}} + 2t^2 \sum_{i \neq 0} \frac{\lambda_i^3}{\mathcal{N}(1-\lambda_i)} \\ &\quad - 2t^2 \sum_{i \neq 0} \frac{\lambda_i^{t-2}}{\mathcal{N}(1-\lambda_i)} \\ &\quad + t^2 \sum_{\substack{i \neq 0 \\ j \neq 0}} \frac{\lambda_i^{t-4} \lambda_j^3 - \lambda_i \lambda_j^{t-2}}{\lambda_i - \lambda_j} Q_{SR}^{ij}. \end{aligned} \quad (\text{D31})$$

The second-order correction to the SFF is

$$K_1^{(2)}(t) = \bar{\mathcal{X}}_T + \bar{\mathcal{X}}_S - \bar{\mathcal{X}}_T^{\{n,n\}} - \bar{\mathcal{X}}_S^{\{n,n\}}. \quad (\text{D32})$$

Substituting Eqs. (D20), (D23), (D27), and (D31) in Eq. (D32), we obtain

$$\begin{aligned} K_1^{(2)}(t) &= -\frac{2t^2}{\mathcal{N}} + 2t^2 \sum_{i \neq 0} \left( \lambda_i^{t-3} Q_{T(1)}^i + \lambda_i^{t-4} Q_{T(2)}^i - \frac{\lambda_i^{t-3}}{\mathcal{N}(1-\lambda_i)} + \frac{\lambda_i^t}{\mathcal{N}(1-\lambda_i)} \right) \\ &\quad + t^2 \sum_{\substack{i \neq 0 \\ j \neq 0}} \left( \frac{\lambda_i^{t-4} \lambda_j - \lambda_i \lambda_j^{t-4}}{\lambda_i - \lambda_j} Q_{T'}^{ij} + \frac{\lambda_i^{t-4} \lambda_j^3 - \lambda_i^3 \lambda_j^{t-4}}{\lambda_i - \lambda_j} Q_S^{ij} - \frac{\lambda_i^t \lambda_j - \lambda_i \lambda_j^t}{\lambda_i - \lambda_j} Q_R^{ij} - \frac{\lambda_i^{t-4} \lambda_j^3 - \lambda_i \lambda_j^{t-2}}{\lambda_i - \lambda_j} Q_{SR}^{ij} \right) \\ &= -\frac{2t^2}{\mathcal{N}} + \mathcal{O}(\lambda_1^t) \end{aligned} \quad (\text{D33})$$

We include the contribution of all the Type III terms in Eq. D33, which we ignore in our calculation with the reduced diagrams in Eq. 95.

### Appendix E: Derivation of the second-order correction in the absence of $\mathcal{T}$ -symmetry using only the rules in Sec. V

#### a. Transposition

Following the rules in Sec. V, the calculation for the cyclic variants of transposition is carried out in a similar way to the  $\mathcal{T}^2 = 1$  case.

$$\begin{aligned} \sum_{l=0}^{t-1} \sum_T \mathcal{Y}_{C^l T} &= \frac{t^2(t-1)}{2\mathcal{N}} + \frac{t^2}{\mathcal{N}} \sum_{i \neq 0} \frac{\lambda_i - \lambda_i^{t-2}}{1-\lambda_i} \\ &\quad + t^2 \sum_{i \neq 0} (\lambda_i^{t-3} Q_{T(1)}^i + \lambda_i^{t-4} Q_{T(2)}^i) \\ &\quad + \frac{t^2}{2} \sum_{\substack{i \neq 0 \\ j \neq 0}} \frac{\lambda_i^{t-4} \lambda_j - \lambda_i \lambda_j^{t-4}}{\lambda_i - \lambda_j} Q_{T'}^{ij}. \end{aligned} \quad (\text{E1})$$

The contribution from the anticyclic variants is

$$\begin{aligned} \sum_{l=0}^{t-1} \sum_T \mathcal{Y}_{\mathcal{R}C^l T} &= \frac{t^2}{2} \sum_{ij} \frac{\chi_i^{t-4} \chi_j - \chi_i \chi_j^{t-4}}{\chi_i - \chi_j} \tilde{Q}_{T'}^{ij} \\ &\quad + t^2 \sum_i \chi_i^{t-3} \tilde{Q}_{T(1)}^i + t^2 \sum_i \chi_i^{t-4} \tilde{Q}_{T(2)}^i, \end{aligned} \quad (\text{E2})$$

where

$$\tilde{Q}_{T'}^{ij} = \tilde{\mathcal{M}}_{f,a}^{(i)} \tilde{\mathcal{M}}_{c,d}^{(j)} V_{a,b} V_{b,c} V_{d,e} V_{e,f} V_{e,a}^* V_{c,e}^* V_{b,d}^* V_{f,b}^*, \quad (\text{E3})$$

$$\tilde{Q}_{T(1)}^i = \tilde{\mathcal{M}}_{d,a}^{(i)} V_{a,b} V_{b,c} V_{c,d} V_{c,a}^* V_{b,c}^* V_{d,b}^*, \quad (\text{E4})$$

$$\tilde{Q}_{T(2)}^i = \tilde{\mathcal{M}}_{e,a}^{(i)} V_{a,b} V_{b,c} V_{c,d} V_{d,e} V_{d,a}^* V_{c,d}^* V_{b,c}^* V_{e,b}^*. \quad (\text{E5})$$

The total contribution from all single transposition diagrams is then:

$$\begin{aligned}
\bar{\mathcal{Y}}_T &= \sum_{l=0}^{t-1} \sum_T \mathcal{Y}_{C^l T} + \sum_{l=0}^{t-1} \sum_T \mathcal{Y}_{RC^l T} \\
&= \frac{t^2(t-1)}{2\mathcal{N}} + \frac{t^2}{\mathcal{N}} \sum_{i \neq 0} \frac{\lambda_i}{1-\lambda_i} + t^2 \sum_{i \neq 0} \left( -\frac{\lambda_i^{t-2}}{\mathcal{N}(1-\lambda_i)} + \lambda_i^{t-3} Q_{T^{(1)}}^i + \lambda_i^{t-4} Q_{T^{(2)}}^i \right) + \frac{t^2}{2} \sum_{\substack{i \neq 0 \\ j \neq 0}} \frac{\lambda_i^{t-4} \lambda_j - \lambda_i \lambda_j^{t-4}}{\lambda_i - \lambda_j} Q_{T'}^{ij} \\
&+ \frac{t^2}{2} \sum_{ij} \frac{\lambda_i^{t-4} \lambda_j - \lambda_i \lambda_j^{t-4}}{\lambda_i - \lambda_j} \tilde{Q}_{T'}^{ij} + t^2 \sum_i \lambda_i^{t-3} \tilde{Q}_{T^{(1)}}^i + t^2 \sum_i \lambda_i^{t-4} \tilde{Q}_{T^{(2)}}^i. \tag{E6}
\end{aligned}$$

b. *Sub-sequence reversal*

The contribution of the sub-sequence reversal diagrams can be found again following the rules in Sec. V as

$$\begin{aligned}
\bar{\mathcal{Y}}_S &= \frac{t}{2} \sum_{\tau_1=1}^t \sum_{\tau_2=\tau_1+3}^{t+\tau_1-5} \sum_{ij} \lambda_i^{\tau_2-\tau_1} \lambda_j^{t-\tau_2+\tau_1-2} Q_S^{ij} \\
&+ \frac{t}{2} \sum_{\tau_1=1}^t \sum_{\tau_2=\tau_1+3}^{t+\tau_1-5} \sum_{ij} \lambda_i^{\tau_2-\tau_1} \lambda_j^{t-\tau_2+\tau_1-2} \tilde{Q}_S^{ij} \\
&= \frac{t^2}{2} \sum_{ij} \frac{\lambda_i^{t-4} \lambda_j^3 - \lambda_i^3 \lambda_j^{t-4}}{\lambda_i - \lambda_j} Q_S^{ij} \\
&+ \frac{t^2}{2} \sum_{ij} \frac{\lambda_i^{t-4} \lambda_j^3 - \lambda_i^3 \lambda_j^{t-4}}{\lambda_i - \lambda_j} \tilde{Q}_S^{ij}, \tag{E7}
\end{aligned}$$

where

$$Q_S^{ij} = \tilde{\mathcal{M}}_{b,c}^{(i)} \mathcal{M}_{d,a}^{(j)} V_{a,b} V_{c,d} V_{a,c}^* V_{b,d}^*, \tag{E8}$$

$$\tilde{Q}_S^{ij} = \mathcal{M}_{b,c}^{(i)} \tilde{\mathcal{M}}_{d,a}^{(j)} V_{a,b} V_{c,d} V_{c,a}^* V_{d,b}^*. \tag{E9}$$

It can be shown that  $Q_{SR}^{i0} = \tilde{Q}_{SR}^{0i} = \text{tr} \tilde{\mathcal{M}}^{(i)} / \mathcal{N} = 1/\mathcal{N}$ . Thus, we get

$$\begin{aligned}
\bar{\mathcal{Y}}_S &= \frac{t^2}{\mathcal{N}} \sum_i \frac{\lambda_i^{t-2} - \lambda_i^3}{\lambda_i - 1} \\
&+ \frac{t^2}{2} \sum_i \sum_{j \neq 0} \frac{\lambda_i^{t-4} \lambda_j^3 - \lambda_i^3 \lambda_j^{t-4}}{\lambda_i - \lambda_j} Q_S^{ij} \\
&+ \frac{t^2}{2} \sum_{i \neq 0} \sum_j \frac{\lambda_i^{t-4} \lambda_j^3 - \lambda_i^3 \lambda_j^{t-4}}{\lambda_i - \lambda_j} \tilde{Q}_S^{ij}. \tag{E10}
\end{aligned}$$

c. *Identity permutation with repetition*

The calculation of the cyclic variants of repetitions is also similar to  $\mathcal{T}^2 = 1$  case.

$$\sum_{l=0}^{t-1} \sum_R \mathcal{Y}_{C^l I}^{\{n,n\}} = \frac{t^2(t-1)}{2\mathcal{N}} + \frac{t^2}{\mathcal{N}} \sum_{i \neq 0} \frac{\lambda_i}{1-\lambda_i}$$

$$- \frac{t^2}{\mathcal{N}} \sum_{i \neq 0} \frac{\lambda_i^t}{1-\lambda_i} + \frac{t^2}{2} \sum_{\substack{i \neq 0 \\ j \neq 0}} \frac{\lambda_i^t \lambda_j - \lambda_i \lambda_j^t}{\lambda_i - \lambda_j} Q_R^{ij}, \tag{E11}$$

Following the rules in Sec. V, total contribution of all the anticyclic variants take the following form:

$$\sum_{l=0}^{t-1} \sum_R \mathcal{Y}_{RC^l I}^{\{n,n\}} = \frac{t^2}{2} \sum_{ij} \frac{\lambda_i^t \lambda_j - \lambda_i \lambda_j^t}{\lambda_i - \lambda_j} \tilde{Q}_R^{ij}, \tag{E12}$$

where

$$\tilde{Q}_R^{ij} = \sum_a \tilde{\mathcal{M}}_{a,a}^{(i)} \tilde{\mathcal{M}}_{a,a}^{(j)}. \tag{E13}$$

Thus, we get the total contribution from the cyclic and anticyclic variants as

$$\begin{aligned}
\bar{\mathcal{Y}}_R^{\{n,n\}} &= \sum_{l=0}^{t-1} \sum_R \mathcal{Y}_{C^l I}^{\{n,n\}} + \sum_{l=0}^{t-1} \sum_R \mathcal{Y}_{RC^l I}^{\{n,n\}} \\
&= \frac{t^2(t-1)}{2\mathcal{N}} + \frac{t^2}{\mathcal{N}} \sum_{i \neq 0} \frac{\lambda_i}{1-\lambda_i} \\
&- \frac{t^2}{\mathcal{N}} \sum_{i \neq 0} \frac{\lambda_i^t}{1-\lambda_i} + \frac{t^2}{2} \sum_{\substack{i \neq 0 \\ j \neq 0}} \frac{\lambda_i^t \lambda_j - \lambda_i \lambda_j^t}{\lambda_i - \lambda_j} Q_R^{ij} \\
&+ \frac{t^2}{2} \sum_{ij} \frac{\lambda_i^t \lambda_j - \lambda_i \lambda_j^t}{\lambda_i - \lambda_j} \tilde{Q}_R^{ij}. \tag{E14}
\end{aligned}$$

d. *Sub-sequence reversal with repetition*

Following the rules in Sec. V, we find the contribution from the sub-sequence reversal with a repetition diagrams as

$$\begin{aligned}
\bar{\mathcal{Y}}_{SR}^{\{n,n\}} &= \frac{t}{2} \sum_{\tau_1=1}^t \sum_{\tau_2=\tau_1+3}^{t+\tau_1-3} \sum_{ij} \lambda_i^{\tau_2-\tau_1-2} \lambda_j^{t-\tau_2+\tau_1} Q_{SR}^{ij} \\
&+ \frac{t}{2} \sum_{\tau_1=1}^t \sum_{\tau_2=\tau_1+3}^{t+\tau_1-3} \sum_{ij} \lambda_i^{\tau_2-\tau_1-2} \lambda_j^{t-\tau_2+\tau_1} \tilde{Q}_{SR}^{ij}
\end{aligned}$$

$$\begin{aligned}
&= \frac{t^2}{2} \sum_{ij} \frac{\lambda_i^{t-4} \lambda_j^3 - \lambda_i \lambda_j^{t-2}}{\lambda_i - \lambda_j} Q_{SR}^{ij} \\
&+ \frac{t^2}{2} \sum_{ij} \frac{\lambda_i^{t-4} \lambda_j^3 - \lambda_i \lambda_j^{t-2}}{\lambda_i - \lambda_j} \tilde{Q}_{SR}^{ij}, \quad (\text{E15})
\end{aligned}$$

where

$$\begin{aligned}
Q_{SR}^{ij} &= \tilde{\mathcal{M}}_{b,c}^{(i)} \mathcal{M}_{a,a}^{(j)} V_{a,b} V_{c,a} V_{a,c}^* V_{b,a}^* \\
&= \left( \tilde{\mathcal{M}} \tilde{\mathcal{M}}^{(i)} \tilde{\mathcal{M}} \right)_{a,a} \mathcal{M}_{a,a}^{(j)} = \chi_i^2 \tilde{\mathcal{M}}_{a,a}^{(i)} \mathcal{M}_{a,a}^{(j)}, \quad (\text{E16})
\end{aligned}$$

$$\tilde{Q}_{SR}^{ij} = \mathcal{M}_{b,c}^{(i)} \tilde{\mathcal{M}}_{a,a}^{(j)} V_{a,b} V_{c,a} V_{c,a}^* V_{a,b}^* = \lambda_i^2 \mathcal{M}_{a,a}^{(i)} \tilde{\mathcal{M}}_{a,a}^{(j)}. \quad (\text{E17})$$

Thus, we can find

$$Q_{SR}^{i0} = \frac{\chi_i^2}{\mathcal{N}} \text{tr} \tilde{\mathcal{M}}^{(i)} = \frac{\chi_i^2}{\mathcal{N}}, \quad (\text{E18})$$

$$\tilde{Q}_{SR}^{0i} = \frac{1}{\mathcal{N}} \text{tr} \tilde{\mathcal{M}}^{(i)} = \frac{1}{\mathcal{N}}. \quad (\text{E19})$$

We substitute Eqs. (E18) and (E19) in Eq. (E15) to find

$$\begin{aligned}
\bar{\mathcal{Y}}_{SR}^{\{n,n\}} &= \frac{t^2}{\mathcal{N}} \sum_i \frac{\chi_i^3}{1 - \chi_i} - \frac{t^2}{\mathcal{N}} \sum_i \frac{\chi_i^{t-2}}{1 - \chi_i} \\
&+ \frac{t^2}{2} \sum_i \sum_{j \neq 0} \frac{\lambda_i^{t-4} \lambda_j^3 - \lambda_i \lambda_j^{t-2}}{\lambda_i - \lambda_j} Q_{SR}^{ij} \\
&+ \frac{t^2}{2} \sum_{i \neq 0} \sum_j \frac{\lambda_i^{t-4} \lambda_j^3 - \lambda_i \lambda_j^{t-2}}{\lambda_i - \lambda_j} \tilde{Q}_{SR}^{ij}. \quad (\text{E20})
\end{aligned}$$

Therefore, we get the total second-order correction to the SFF for systems in the absence of  $\mathcal{T}$ -symmetry as

$$\begin{aligned}
K_0^{(2)}(t) &= \bar{\mathcal{Y}}_T + \bar{\mathcal{Y}}_S - \bar{\mathcal{Y}}_R^{\{n,n\}} - \bar{\mathcal{Y}}_{SR}^{\{n,n\}} \\
&= t^2 \sum_{i \neq 0} \left( -\frac{\lambda_i^{t-2}}{\mathcal{N}(1 - \lambda_i)} + \lambda_i^{t-3} Q_{T(1)}^i + \lambda_i^{t-4} Q_{T(2)}^i \right) + \frac{t^2}{2} \sum_{\substack{i \neq 0 \\ j \neq 0}} \frac{\lambda_i^{t-4} \lambda_j - \lambda_i \lambda_j^{t-4}}{\lambda_i - \lambda_j} Q_{T'}^{ij} \\
&+ t^2 \sum_{ij} \frac{\lambda_i^{t-4} \lambda_j - \lambda_i \lambda_j^{t-4}}{\lambda_i - \lambda_j} \tilde{Q}_{T'}^{ij} + t^2 \sum_i \lambda_i^{t-3} \tilde{Q}_{T(1)}^i + t^2 \sum_i \lambda_i^{t-4} \tilde{Q}_{T(2)}^i \\
&+ \frac{t^2}{2} \sum_i \sum_{j \neq 0} \frac{\lambda_i^{t-4} \lambda_j^3 - \lambda_i^3 \lambda_j^{t-4}}{\lambda_i - \lambda_j} Q_S^{ij} + \frac{t^2}{2} \sum_{ij} \frac{\lambda_i^{t-4} \lambda_j^3 - \lambda_i^3 \lambda_j^{t-4}}{\lambda_i - \lambda_j} \tilde{Q}_S^{ij} \\
&+ \frac{t^2}{\mathcal{N}} \sum_{i \neq 0} \frac{\lambda_i^t}{1 - \lambda_i} - \frac{t^2}{2} \sum_{\substack{i \neq 0 \\ j \neq 0}} \frac{\lambda_i^t \lambda_j - \lambda_i \lambda_j^t}{\lambda_i - \lambda_j} Q_R^{ij} - \frac{t^2}{2} \sum_{ij} \frac{\lambda_i^t \lambda_j - \lambda_i \lambda_j^t}{\lambda_i - \lambda_j} \tilde{Q}_R^{ij} \\
&+ \frac{t^2}{\mathcal{N}} \sum_i \frac{\chi_i^{t-2}}{1 - \chi_i} - \frac{t^2}{2} \sum_{ij} \frac{\lambda_i^{t-4} \lambda_j^3 - \lambda_i \lambda_j^{t-2}}{\lambda_i - \lambda_j} Q_{SR}^{ij} - \frac{t^2}{2} \sum_{ij} \frac{\lambda_i^{t-4} \lambda_j^3 - \lambda_i \lambda_j^{t-2}}{\lambda_i - \lambda_j} \tilde{Q}_{SR}^{ij} \\
&= \mathcal{O}(\lambda_1^t, \lambda_0^t). \quad (\text{E21})
\end{aligned}$$

Equation (E21) shows the absence of universal term at second order in time, which explains the emergence of

CUE SFF. Equation E21 includes the contribution of all Type III terms, which are ignored in our calculation with the reduced diagrams in Eq. 104.

- [1] O. Bohigas, M. J. Giannoni, and C. Schmit, Characterization of chaotic quantum spectra and universality of level fluctuation laws, *Phys. Rev. Lett.* **52**, 1 (1984).  
[2] S. W. McDonald and A. N. Kaufman, Spectrum and eigenfunctions for a Hamiltonian with stochastic trajectories, *Phys. Rev. Lett.* **42**, 1189 (1979).

- [3] G. Casati, F. Valz-Gris, and I. Guarneri, On the connection between quantization of nonintegrable systems and statistical theory of spectra, *Lett. Nuovo Cimento* **28**, 279 (1980).  
[4] M. V. Berry and M. Tabor, Level clustering in the regular spectrum, *Proc. R. Soc. Lond. A* **356**, 375 (1977).



- [5] M. V. Berry, Quantizing a classically ergodic system: Sinai's billiard and the KKR method, *Ann. Phys.* **131**, 163 (1981).
- [6] M. L. Mehta, *Random matrices, 2nd ed.* (Academic Press, San Diego, 1991).
- [7] E. P. Wigner, Characteristic vectors of bordered matrices with infinite dimensions, *Ann. Math.* **62**, 548 (1955).
- [8] E. P. Wigner, *Group Theory and its Application to the Quantum Mechanics of Atomic Spectra* (Academic Press Inc., New York, 1959).
- [9] F. J. Dyson, Statistical theory of the energy levels of complex systems. i, *J. Math. Phys.* **3**, 140 (1962).
- [10] F. J. Dyson, Correlations between eigenvalues of a random matrix, *Commun. Math. Phys.* **19**, 235 (1970).
- [11] M. V. Berry, theory of spectral rigidity, *Proc. R. Soc. Lond. A* **400**, 229 (1985).
- [12] M. Sieber and K. Richter, Correlations between periodic orbits and their role in spectral statistics, *Phys. Scr.* **T90**, 128 (2001).
- [13] M. Sieber, Leading off-diagonal approximation for the spectral form factor for uniformly hyperbolic systems, *J. Phys. A* **35**, L613 (2002).
- [14] S. Müller, S. Heusler, P. Braun, F. Haake, and A. Altland, Semiclassical foundation of universality in quantum chaos, *Phys. Rev. Lett.* **93**, 014103 (2004).
- [15] S. Müller, S. Heusler, P. Braun, F. Haake, and A. Altland, Periodic-orbit theory of universality in quantum chaos, *Phys. Rev. E* **72**, 046207 (2005).
- [16] Z. Pluhař and H. A. Weidenmüller, Universal quantum graphs, *Phys. Rev. Lett.* **112**, 144102 (2014).
- [17] Z. Pluhar and H. A. Weidenmüller, Quantum graphs and random-matrix theory, *J. Phys. A-Math.* **48**, 275102 (2015).
- [18] R. Dubertrand and S. Müller, Spectral statistics of chaotic many-body systems, *New J. Phys.* **18**, 033009 (2016).
- [19] P. Kos, M. Ljubotina, and T. Prosen, Many-body quantum chaos: Analytic connection to random matrix theory, *Phys. Rev. X* **8**, 021062 (2018).
- [20] A. Chan, A. De Luca, and J. T. Chalker, Solution of a minimal model for many-body quantum chaos, *Phys. Rev. X* **8**, 041019 (2018).
- [21] A. Chan, A. De Luca, and J. T. Chalker, Spectral statistics in spatially extended chaotic quantum many-body systems, *Phys. Rev. Lett.* **121**, 060601 (2018).
- [22] B. Bertini, P. Kos, and T. Prosen, Exact spectral form factor in a minimal model of many-body quantum chaos, *Phys. Rev. Lett.* **121**, 264101 (2018).
- [23] B. Bertini, P. Kos, and T. Prosen, Exact correlation functions for dual-unitary lattice models in 1 + 1 dimensions, *Phys. Rev. Lett.* **123**, 210601 (2019).
- [24] B. Bertini, P. Kos, and T. Prosen, Entanglement spreading in a minimal model of maximal many-body quantum chaos, *Phys. Rev. X* **9**, 021033 (2019).
- [25] A. J. Friedman, A. Chan, A. De Luca, and J. T. Chalker, Spectral statistics and many-body quantum chaos with conserved charge, *Phys. Rev. Lett.* **123**, 210603 (2019).
- [26] D. Roy and T. Prosen, Random matrix spectral form factor in kicked interacting fermionic chains, *Phys. Rev. E* **102**, 060202(R) (2020).
- [27] S. Moudgalaya, A. Prem, D. A. Huse, and A. Chan, Spectral statistics in constrained many-body quantum chaotic systems, *Phys. Rev. Research* **3**, 023176 (2021).
- [28] B. Bertini, P. Kos, and T. Prosen, Random matrix spectral form factor of dual-unitary quantum circuits, *Commun. Math. Phys.* **387**, 597 (2021).
- [29] S. J. Garratt and J. T. Chalker, Local pairing of Feynman histories in many-body Floquet models, *Phys. Rev. X* **11**, 021051 (2021).
- [30] D. Roy, D. Mishra, and T. Prosen, Spectral form factor in a minimal bosonic model of many-body quantum chaos, *Phys. Rev. E* **106**, 024208 (2022).
- [31] K. Richter, J. Diego Urbina, and S. Tomsovic, Semiclassical roots of universality in many-body quantum chaos, *J. Phys. A* **55**, 453001 (2022).
- [32] M. Winer and B. Swingle, Hydrodynamic theory of the connected spectral form factor, *Phys. Rev. X* **12**, 021009 (2022).
- [33] M. Winer and B. Swingle, The Loschmidt spectral form factor, *J. High Energ. Phys.* **2022**, 137 (2022).
- [34] Y. Liao and V. Galitski, Emergence of many-body quantum chaos via spontaneous breaking of unitarity, *Phys. Rev. B* **105**, L140202 (2022).
- [35] L. K. Joshi, A. Elben, A. Vikram, B. Vermersch, V. Galitski, and P. Zoller, Probing many-body quantum chaos with quantum simulators, *Phys. Rev. X* **12**, 011018 (2022).
- [36] C. Dag, S. Mistakidis, A. Chan, and H. R. Sadeghpour, Many-body quantum chaos in stroboscopically-driven cold atoms, *Commun. Phys.* **6**, 136 (2023).
- [37] V. Kumar and D. Roy, Many-body quantum chaos in mixtures of multiple species, *Phys. Rev. E* **109**, L032201 (2024).
- [38] A. Vikram and V. Galitski, Exact universal bounds on quantum dynamics and fast scrambling, *Phys. Rev. Lett.* **132**, 040402 (2024).
- [39] T. N. Ikeda, L. Vidmar, and M. O. Flynn, Exact spectral form factors of non-interacting fermions with dyson statistics, [arXiv:2410.08269](https://arxiv.org/abs/2410.08269) (2024).
- [40] F. Haake, *Quantum Signatures of Chaos, 2nd ed.* (Springer, New York, 2001).
- [41] H. Gharibyan, M. Hanada, S. H. Shenker, and M. Tezuka, Onset of random matrix behavior in scrambling systems, *J. High Energ. Phys.* **2018**, 124 (2018).
- [42] S. Heusler, The semiclassical origin of the logarithmic singularity in the symplectic form factor, *J. Phys. A* **34**, L483 (2001).
- [43] A. K. Das, C. Cianci, D. G. Cabral, D. A. Zarate-Herrada, P. Pinney, S. Pilatowsky-Cameo, A. S. Matsoukas-Roubeas, V. S. Batista, A. del Campo, E. J. Torres-Herrera, *et al.*, Proposal for many-body quantum chaos detection, [arXiv:2401.01401](https://arxiv.org/abs/2401.01401) (2024).
- [44] H. Dong, P. Zhang, C. B. Dağ, Y. Gao, N. Wang, J. Deng, X. Zhang, J. Chen, S. Xu, K. Wang, Y. Wu, C. Zhang, F. Jin, X. Zhu, A. Zhang, Y. Zou, Z. Tan, Z. Cui, Z. Zhu, F. Shen, T. Li, J. Zhong, Z. Bao, H. Li, Z. Wang, Q. Guo, C. Song, F. Liu, A. Chan, L. Ying, and H. Wang, Measuring the spectral form factor in many-body chaotic and localized phases of quantum processors, *Phys. Rev. Lett.* **134**, 010402 (2025).
- [45] L. E. Fischer, M. Leahy, A. Eddins, N. Keenan, D. Ferracin, M. A. Rossi, Y. Kim, A. He, F. Pietracaprina, B. Sokolov, *et al.*, Dynamical simulations of many-body quantum chaos on a quantum computer, [arXiv:2411.00765](https://arxiv.org/abs/2411.00765) (2024).
- [46] A. Altland and M. R. Zirnbauer, Nonstandard symmetry classes in mesoscopic normal-superconducting hybrid structures, *Phys. Rev. B* **55**, 1142 (1997).

- [47] S. A. Gershgorin, Über die abgrenzung der eigenwerte einer matrix, *Izv. Math.* , 749 (1931).
- [48] R. A. Horn and C. R. Johnson, *Matrix Analysis* (Cambridge University Press, 1985).